Therapeutic Approach of selected Nano Composites with Mechanism of action in Colon Cancer

Thesis submitted for the degree of
Doctor of Philosophy (Tech.) in Chemical Technology

by
Snehasis Mishra
Department of Chemical Technology
2021

To my Ma

Acknowledgement

Every thesis has a story to tell… what it doesn't tell is the story behind building the thesis. A story with different phases… the springs… the falls… the anxieties...the frustrations… the happiness… the highs…the lows… and in this journey of mixed feelings there are multiple characters that either lends a hand of support or pulls you down.

This thesis marks the end of my doctoral research work which I carried out at Department of Chemical Technology Division, University of Calcutta and CSIR-Indian Institute of Chemical Biology under the esteemed guidance of **Prof. Sriparna Dutta** and **Dr. Krishna Das Saha** respectively. Prof. Dutta has not only been my supervisor but also an excellent mentor and an immense source of knowledge and guidance… a knowledge gathered by the years of experience that guided me to sail through. Her aptitude for research, scientific foresightedness and grasp over the subject is impeccable. I will always be indebted to her for making me a part of his list of students. Her supervision and constant words of encouragement incepted the zeal to overcome even the most frustrating moments associated with this journey. Apart from being an excellent scientist and mentor Prof. Dutta is a lovely human being at heart and I will always be indebted to her for standing by me whenever I needed him.

Next, I would like to acknowledge my co-supervisor, **Dr. Krishna Das Saha, CSIR-IICB** for his constant support and encouragement. I will also be indebted to her for allowing me to carry out some of my experiments in her lab. Thank you, Madam for being such a great source of support and inspiration.

I want to thank **Prof. Achintya Saha**, faculty of the Department of Chemical Technology, University of Calcutta for giving freedom to utilise laboratory facilities to carry out my research work. I acknowledge the support of Applied Chemistry Library and its staff members.

I would also like to express my sincere gratitude towards our collaborator, **Prof. Asim Bhaumik** from Indian Association for the Cultivation of Science (Department of Material Science), **Prof. Samir Kumar Pal** from S N Bose national centre for Basic Sciences, and **Dr. Chandan Kumar Ghosh** from Jadavpur University for their scientific guidance.

I take this opportunity to thank other faculties of IICB, specially **Dr. H. K. Majumder, Dr. Sanjay Dutta, Dr. Nakul Chandra Maity, Dr. Nahid Ali, Dr. Sib Sankar Roy** and **Dr. Shyamal Roy** for making my journey a learning experience.

I am thankful to **Santanuda, Helendi, Eshika** and **Dipanjanda** from Prof. Sriparna Dutta's lab for all their help.

I am also thankful to **Niladrida, Tanushree, Saswati, Sayoni, Moumita, Saheli, Sanchaita** and **Sanjib** from Dr. Krishna Das Saha's lab for their kind help. In addition I want to

acknowledge **Krishnenduda** from Dr. Krishna Das Saha's lab for his co-operation and timely advices.

The guidance I received from cannot be limited to my lab members only and involves seniors from other labs at IICB as well. **Shameel Bhaia, Tridibda, Sarfaraz Bhaia, Sayanikadi, Mithunda, Abdusda, Monida, Banida, Archyoda, Somda, Chinmayda, Sandipda, Anirbanda** deserves a special mention in this regard.

My journey at IICB is incomplete without my pillars...my friends **Kamran, Ritesh, Debu, Subroto, Sambit, Peter, Saif, Anandda, Samrat, Achintada, Koushikda, Rajeevda, Dhiren Bhaia, Dipayan Da, Sumantada, Satadruda, Suvankarda, Chittranda, Suborno, Paros, Pulok, Sourav, Biswada, Narattom, Eshayan, Sumon,** and **Kajol** have always supported me and helped me find a way whenever I was lost.

I want to acknowledge **Mr. Jeet Chakraborty** for his unconditional help...

I take this opportunity to thank all of you and say that without you this journey wouldn't have been complete.

Next, I want to acknowledge the integral members of my life...**Debu (School friend), Saikat, Sudipto, Akshay, Narayan, Susovon, and Mantuda**. They have always been by me and helped me in shaping me into the person I am today. Thank you, guys, for holding me whenever I lost the strength to fight.

I owe this thesis to my **Mom, Dad, Sister** and **Wife**. I will always be indebted to their unconditional love, support and sacrifices.

Index

Introduction:

Cancer begins when cells in a part of the body start to grow out of control (1). There are many kinds of cancer, but they all start because of out-of-control growth of abnormal cells (2). Dawn of history people have written about cancer. Some of the earliest evidence of cancer is found among fossilized bone tumors, human mummies in ancient Egypt, and ancient manuscripts. Growths suggestive of the bone cancer called osteosarcoma have been seen in mummies. Bony skull destruction as seen in cancer of the head and neck has been found, too.Since the earliest medical records were kept, Cancer as a disease was first described in several It's called the Edwin Smith Papyrus and is a copy of part of an ancient Egyptian textbook on trauma surgery. It describes 8 cases of tumors or ulcers of the breast that were removed by cauterization with a tool called the fire drill. The writing says about the disease, "There is no treatment."Egyptian medical practice on Cancer was described in two papyri, known as the "Edwin Smith" and "George Ebers" papyri. In those books of cancer, which were written around 1600 B.C., and are believed to date from sources as early as 2500 B.C described not only basic characteristics of this malady but also a few ways of remedies and case studies. The Smith papyrus describes surgery, while the Ebers' papyrus outlines pharmacological, mechanical, and magical treatments. Based on the information recorded on papyri and hieroglyphic inscriptions, ancient Egyptians were able to distinguish benign tumors from malignant tumors. They were also able to use different treatments, including surgery, and other various modes of medicine (3).

Following the decline of Egypt, the next chapters of medical and scientific history were written in Greece and Rome. The great doctors Hippocrates and Galen dominated medical thought for 1500 years. They lifted medicine out of the realms of magic, superstition, and religion. Hippocrates and Galen defined disease as a natural process, and based treatment on observation and experience. Cancers were identified, with warnings against treatment of the more severe forms. Hippocrates is credited with naming "cancer" as "karkinoma" (carcinoma) because a tumor looked like a "crab" ("karkinoma" is Greek for "crab") in that there isa central body to a tumor and the tumor extension appeared as the legs of the "crab"(4).

After the fall of Rome, Constantinople became the intellectual storehouse of civilization. From there, in Arabic translations, classic Greek and Roman texts made their way back through Europe. The ancient teachings of Galen continued to inspire physicians in Constantinople, Cairo, Alexandria, Athens, and Antioch in a time when magic spells and

myths dominated the West. Cancer continued to be explained as the result of an excess of black bile, curable only in its earliest stages (5).

In the modern world, science and surgery advanced as physicians returned to direct observation of the human body. However, the theory that cancer was caused by an excess of black bile continued to prevail in the 16th century. Cancer was considered incurable, although a wide variety of pastes containing arsenic were formulated to treat its manifestations (6).

In the 17th century, the old theory of disease based on bodily humors was discarded when GaspareAselli discovered the vessels of the lymphatic system and suggested abnormalities of lymph as the primary cause of cancer (7).Rejecting the 17th-century theory about the cause of cancer was the French physician Claude Gendron. He concluded that cancer arises locally as a hard, growing mass, untreatable with drugs, and must be removed with all its "filaments"(8).

Two 18th-century French scientists, physician Jean Astruc and chemist Bernard Peyrilhe, conducted experiments to confirm or disprove hypotheses related to cancer(9). Their efforts, however absurd they seem in retrospect, established experimental oncology, the science of seeking better diagnosis(10)treatments and understanding of the causes of cancer. During this period, environmental cancers were reported, and hospitals specializing in cancer care were opened(11).

In the late 19th century, the development of better microscopes not only helped document and define disease-causing organisms, but also made possible the examination of cells and cellular activity(12). Study of cancer tissues and tumors revealed that cancercells were markedly different in appearance than normal cells of surrounding tissue or the cells from which they originated(13). Researchers began to focus on questions such as the origin of cells and the relationship of disease to the behavior of a cell. It was the invention of the microscope that revealed the cancer cell itself.

The early 20th century saw great strides made in understanding the structures, functions and chemistry of living organisms. Cancer research in cell culture, chemical carcinogens, diagnostic techniques and chemotherapy firmly established oncology as science. Researchers pursued different theories of the origin of cancer, subjecting their hypotheses to systematic experimentation. A viral cause of cancer in chickens was documented in 1911 (14), and both

chemical and physical carcinogens were conclusively identified. Chromosomal abnormalities were also investigated as possible causes of cancer (15).

In 1913, a need to combat rising public fear and ignorance concerning cancer led to two significant events: the publication of the first known article on cancer's warning signs in a popular woman's magazine (16), and formation of a nationwide organization dedicated to public education on cancer (17). Cancer, as a disease, was brought into the light of day.

In 1937, the U.S. Congress made the conquest of cancer a national goal with a unanimous vote to pass the National Cancer Institute Act. This Act created the National Cancer Institute, which was expected to break new theoretical ground by conducting its own research, promoting research in other institutions and coordinating cancer-related projects and activities. In 1971, President Richard M. Nixon signed the National Cancer Act, launching a National Cancer Program administered by the National Cancer Institute (18).

Since its establishment, fundamental biomedical research supported by the National Cancer Institute has advanced the understanding of cancer. Using tools of molecular biology and molecular genetics, scientists are making great leaps in the discovery and mapping of links between chromosomes, the genes within, and cancer. In addition to traditional cancer therapies, potential solutions to the prevention and cure of cancer seem limited only by the imagination.

Colorectal cancer /bowel cancer/ rectal cancer or colon cancer is may be described as development of abnormal neoplastic growth which can capable of mature enough to metastasize locally as well as distant organs. Dr. Aldred Warthin first investigate and described this type of cancer in gastric and colon in 1913. Now a days, colon cancer referred as second most common cause of cancer related death in USA. In 2020, 147,950 peoples will be tested positive for this fetal disease and among the 53,200 patients were not survived (19). According to American cancer society this type of cancer comes with some physical symptoms like (20) –

- Weakness and fatigue
- Sudden and unintended weight loss
- Rectal bleeding with bright red blood

- Dark brown blood in stool
- Black stool
- Sudden change in bowel habits, specifically constipation, narrowing of the stool even diarrhea. Symptoms are last for a few days and frequently repeat.
- Irregular Felling of bowel movement but not release.

Presently, colorectal cancer is predominantly reported in Australia, New Zealand, Europe and North America and lower rate in Africa and Asia. One geographical variation of colorectal cancer is noted, reports surprisingly suggested more than half of the cases are reported from the developed countries. Mortality rate is rather higher in less developed countries with limited medical resources and related infrastructures.By analyzing epidemiological and demographic reports, experts are hypothesized that difference in dietary and environmental cues played a silent but crucial role in development of this fatal disease. According to IARC, 2011inflammatory bowel disease, life style, genetic background, presence of polyp and lastly age are major factors. Whereas, research established factors such as obesity, physical inactivity, poor diet, smoking and heavy alcohol consumption is causing more than 80% of all colorectal cancer cases (21). Two hereditary disease, namely, Familial adenomatous polyposis and Lynch Syndrome is responsible for 10% of all colorectal cancer cases.

In Indian scenario, 7.2 per 100,000 males and 5.1 per 100,000 female are carrying colorectal cancer. However, this scenario is looks very minute in number, but reality is just massive. In a country with over a billion population, statistically actual number of suffering patient is just devastatingly colossal. Survival rate is leadingly lowest in the world. Only 40% patients can manage to survive for five years after diagnosis of the disease. CONCORDE-2 study revealed five year survival rate is actually falling in some territories. Hence in developed countries 80% of patients now survived the first year after diagnosis and approximately 62% survive after 5 years or more (22). That pin pointed to inadequate diagnostics as well as therapeutics.

Morphological and anatomical characteristics of Colon:

Colon is a part of large intestine, which is the end section of the alimentary canal and positioned in between terminal ileum and anal canal. In case of normal adult individual, colon is approx.1.5 meter long, tubular structure, made up with cecum or the ascending colon, hepatic flexure, transverse colon, splenic flexure, descending colon and the sigmoid colon. Rectum is 12 cm long starts at peritoneal reflexion and runs through the curve of the sacrum and ends at anal canal. It operates as a primary reservoir of fecal matters (23).

Histopathological observation of colon illustrated four layers, *i.e*. the mucosa, the sub mucosa, the muscularis externa/propria (containing circular and smooth muscle layers) and lastly serosa. Mutation and other genetic alterations are usually noticed in mucosa cells. Because they are highly dividing in nature to continue replenish cells in the bowel wall. Rectal mucosa is quite similar in structure but they have numerous goblet cells. Sub mucosa layer is an important layer encompasses blood vessels, lymphatic and terminal nerve fibers. At the point of tumor maturation, it invaded into this region of bowel wall and communicates with blood as well as lymphatic system lastly metastasize (24).

Colorectal Cancer:

Colorectal cancer or colon cancer is a single disease, termed for generation and maturation of malignant growth at large bowel and occasionally, confined locally for a comparatively long period before metastasis from the bowel wall via angiogenic and lymphogenic process to other parts of the body (25).

Evaluation of epidemiological aspects of Colorectal Cancer:

According to reports of GLOBOCAN 2018, colon cancer is the fourth most common cancer in the world, and cancer in the rectum is in the eight places. In together, colorectal cancer is placed at the third leading cancer in the world comprising 11% of total cancer diagnosis (26).

In 2020, 1931590 new patients were diagnosed colorectal cancer among them 1065960 were male and 865630 were female. Among them 1148515 individuals were suffered colon cancer and rests were rectal (27).

Comprising with other continent, Africa, Asia and Latin America have lowest incidence of colorectal cancer. Australia and New Zealand has noted as highest rates of (44.8 and 32.2 per 100,000 in men and women respectively) colon cancer patients. Colon cancer is fifth most

deadly cancer worldwide in 2020. In that year GLOBOCAN reported 576858 patients died in this disease. That comprising 5.8% of all cancer deaths. Highest rate of mortality is observed in Hungary (31.2 in male and 14.8 in female) (28).

Causative factors for generation of colon cancer:

Formation and development of colon cancer is a very complex process.It forms by involving factors from surrounding environment and hereditary cues. Colon cancer found in two types: sporadic and inherited. 70 to 75% reported colon cancer are sporadic (people without any family history), whereas only 20 to 25% had cases in their pedigree. The *de novo* genetic changes, mainly caused by etiologic factors like age, life style, environmental exposure of toxicants as well as carcinogens; are prime causative factors for this sporadic cases (29).

Age:

Although, risk of developing colon cancer increases with age and affect all ages butreports suggests, commonly of colon cancer is diagnosed after age of fifty years and rate is highest in 60 to 79 years aged population. Recent reports suggested colon cancer is 10^{th} most common cancer for younger population in between 20-49 years in USA (30).

Life style cues for colon cancer:

Ingredients of our consumed foods and beverages are directly interacts with colon. Therefore effect of culinary culture on colon cancer has been thoroughly studied with very much importance. Terry et al. 2001 first time coined consume low fruit and vegetables increase risk of colorectal cancer (31). Several researchers not only hypothesized but also evidenced consuming anti-oxidant, leafy vegetables, hi-fiber diet, folic acid, flavone containing vegetables mitigate chance of colon cancer. Variation in culinary culture, type consumed food as well as gut microbiota, shows a great impact on epidemiological analysis of colon cancer. Dietary fiber increase faecal bulk and decrease colonic handling time, which lesser external exposure time. Life style practitioner and researcher observe an tight relationship between dietary fiber consumption and deduction of colon cancer risks (32).

Studies also suggested regular diet containing high amount of animal fat and cholesterol precisely red meat increase chance of colon cancer development. That may be major factor for colon cancer predominance in western world. High meat diet develop a unique gut

microbiota which colony can degrade bile salts and generate highly carcinogenic N-nitroso compounds (33). Grilled or barbecued meat preparation generate heterocyclic amines and aromatic hydrocarbons *i.e.* highly carcinogenic in nature.

Meta-analysis study revealed regular exercise reduces obesity and prostaglandin level that decrease gut transit time that can boost chances of colon cancer. Studies proven exercise in daily habit can reduce chance of colon cancer by almost 25% in both sexes. Meta-analysist also estimated that individual with a body mass index $\geq 30 kg/m^2$ had a 20% more prone to develop colon cancer as comprising with normal weighted control (34).

Increased blood glucose level, hyper insulinemia, diabetes mellitus with insulin resistance are now very common metabolic disorder and presently proved as associated inducer of colon cancer. Meta-analysis report evidenced type-2 diabetes mellitus solely increase 30% risk of colon cancer (35). Molecular and protein-protein interaction that modulate colon cancer development, has been shown their close moiety with altered metabolism and insulin resistance syndrome. Hypertension, can also a cues to increase risk factor by altering hyperplasia metabolism through modulating blood sugar level (36).

Tobacco derived carcinogens like heterocyclic amine, nitrosamines and poly cyclic hydrocarbons are evidently store and inoculated at colon and rectal regions. That are highly carcinogenic compounds and research well evidently demonstrated cigarette smoking is important cues for not only the formation of colon cancer but also maturation and uncontrolled growth rate of adenomatous polyps *i.e.* precursor for colon cancer (37)

One surprising meta-analysis study reported risk of colorectal cancer is significantly lower after women postmenopausal stage, who received Hormonal replacement therapy compared with untreated population. That indicated a role of alteration in physiologicallevelsex hormones in formation and maturation of tumor. It was recently reported that estrogen, restrict IGF-1 in serum and also attenuate production of bile acids. In this way, estrogen not only inhibits colon cancer generation, but also restricting tumor progression by attenuating mitogen guided cell proliferation and subsequent transformation of carcinoma. Similar effect was also noticed in NSAIDs treated patients, this group of drugs interact in similar molecular pathway and reduce chance of colon cancer progression. These experimental analysis also supported by epidemiologists and meta-analysist (38).

Non-Sporadic Colon Cancer:

Only 5-10% of total colon cancer patients has suffered in this fetal disease because of hereditary factors. Studies reveled that it is inherited from first degree relatives of biological parents with diagnosed adenoma or metastatic colon cancer. Besides family culinary traditions, mutation in several responsible genes at germ cells is predominant cues for generation of colon cancer (39). Familial adenomatous polyposis, hereditary non polyposis colorectal cancer, Lynch syndrome in family pedigree can be noted as forecaster for colon cancer. Patients with inflammatory Bowl syndrome, Crohn's disease, Uncreative colitis, Cowden disease, Peutz-jeghers disease, Turcot's syndrome, and Gardener's syndromes are noted as inducer and early notifier of this disease (40). Ulcerative colitis patients have reported as more prone to develop colon cancer, several studies demonstrated 2% of ulcerative colitis patients develop colon cancer after 10 years, 8% after 20 years and 18% after 30 years (41).

Chromosome instability played an important factor to develop aneuploid tumor cells. This is responsible for several genetic mutation of several genes like APC, KRAS, TGF-β, PIK3CA, EGFR, BRAF, TP53 are prime. Alteration of chromosomal microsatellites is responsible for 15% of non-sporadic colon cancer. Microsatellites are small repetitive DNA sequences within 1-6 bp long play a important role not only in hyperplasia and tumor progression. Mutation in set of tumor suppressor genes like p53, BAX, BCL2, NF-κβ, BAD, BIM play important roles (42). Genetics are reported that DNA mismatch repair is responsible for 90% of colon cancer related disease. DNA methylation specially in CpG island play some role in development in colon cancer (43).

Therapeutic Approaches:

The basic four approaches are currently used for the treatment of CRC: surgery, chemotherapy, radiotherapy and targeted therapies. The mainstay of CRC treatment is surgery. In early stage disease (stage 0 or I), surgical excision can be used without need for further treatment options, as the recurrence rate for node-negative T1 CRC is not good enough (44). Many studies have now shown that adjuvant therapy has a survival benefit for patients with stage III disease, and therefore, this is the standard of care. The situation is still not very clear for stage II CRC patients, however, in which there is somewhat conflicting, evidence regarding the benefit of adjuvant therapy. It is agreed that "high-risk" stage II

patients should be offered adjuvant therapy, as they are the most likely to derive a benefit, although there is currently some debate regarding the exact definition of “high-risk” stage II CRC. Patients with stage IV disease require chemotherapy or targeted therapies combined with surgery.There are some formulation based approaches for CRC like different metal nanoparticles, Polymer based and some inorganic nanohybrid based drug delivery. Several receptor based drug delivery also has been studied. Briefly Discussed hare with (45):

Nanocarriers for drug delivery:

Nanomedicine is a rapidly developing area that is revolutionizing cancer diagnosis and therapy. Nanoparticles have unique biological properties given their small size (diameter within 1–100 nm) and large surface area to volume ratio, which allows them to bind, absorb and carry anticancer agents, such as drugs, DNA, RNA, and proteins,along with imaging agents with high efficiency (46). Nanocarriers used in chemotherapy can be classified into two major types designed for targeted or non-targeted drug delivery: vehicles that use organic molecules as a major building block material and those that use inorganic elements (usually metals) as a core. Organic nanocarriers are comprised of liposomes, lipids, Dendrimer, carbon nanotubes, emulsions, and synthetic polymers (47). Inorganic nanocarrier platforms have been intensively investigated for therapeutic and imaging treatments in recent years due to their great advantages, such as large surface area, better drug loading capacity, better bioavailability, lower toxic side effects and controlled drug release, and their tolerance towards most organic solvents, unlike polymer-based nanoparticles. Now a days several groups are working on Quantum dots, Covalent organic frameworks (COFs), Organic Polymers, mesoporous silica and magnetic nanoparticles mediated cancer treatment in various ways (48).

Mesoporous silica nano (MSNs) with tunable pore sizes offer great potential for controlling drug loading percentages and release kinetics and can deliver antitumor drugs in a targeted fashion, releasing them on demand to increase their cellular uptake without any premature release prior to reaching the target site (49). Another advantage of MSNs is their ability to deliver membrane impermeable hydrophobic drugs, thereby serving as a universal transmembrane carrier for intracellular drug delivery and imaging applications. They also have emerged as promising candidates for both passive and active targeted delivery systems and can accumulate in tumor tissues via the enhanced permeation and retention (EPR) effect. Furthermore, specific drug delivery can be achieved via active targeting by the

functionalizing of MSNs with targeting ligands, such as folate (FA) or EGF. Antibodies, peptides, and magnetic nanoparticles can also be decorated onto MSNs, thereby acting as a homing device (50). In the targeting process, particle size and surface modification of MSNs critically influence particle cellular uptake, pharmacokinetics, and Biodistribution profiles. Calcium phosphate-based organic–inorganic nanocarriers are known for switching on photodynamic therapy in response to acidic environments. Mn2+ within calcium phosphate nanoparticles of poly(ethylene glycol) shells has been found to act as an efficient magnetic resonance imaging (MRI) contrast agent that rapidly amplifies magnetic resonance signals in response to pH. Superparamagnetic iron oxide nanoparticles (SPIONs) are receiving increased attention for chemotherapy, hypothermia, magnetic resonance imaging (MRI), tissue engineering, cell and tissue targeting and transfection due to their intrinsic properties, such as inherent magnetism, visualization by magnetic resonance (MR) imaging, biocompatibility, guidance to target sites by means of an external magnetic field, heating to provide hyperthermia for cancer therapy and degradation into nontoxic iron ions in vivo. SPIONs are composed of an inner magnetic particle core (usually magnetite, Fe_3O_4, or maghemite, γ-Fe_2O_3) and a hydrophilic coating of polymers, such as polysaccharide, poly(ethylene glycol) (PEG), and poly(vinyl alcohol). Direct use of SPIONs without any polymer coating as an in vivo MRI contrast agent results in biofouling of the particles in blood plasma and particle agglomerations that are quickly sequestered by cells of the reticular endothelial system (RES), such as macrophages. The coating helps to shield the magnetic particle from the surrounding environment and can also be functionalized by targeting ligands. These magnetic drug-bearing nanocarriers rely on external magnetic field guidance to reach their target tissue (51). Magnetic albumin microspheres (MM-ADR) in animal tumor models exhibit better responses than Adriamycin alone both in terms of tumor size reduction and animal survival. The enhanced efficacy of magnetic albumin microspheres in the targeted delivery of an anticancer agent compared to the pure drug in rat model is predominantly due to magnetic effects and is not due to the particle's size or nonmagnetic holding. SPION based MRI is a very powerful non-invasive tool in biomedical imaging, clinical diagnosis, and therapy (52).

The Current study deals with new theranostics which having Photothermal activity along with the newly synthesized Covalent Organic Framework (COF) which having anticancer property against Human Colorectal Carcinoma (HCT 116) *in vitro*. The another part of the present

study is Theranostic application of novel Folate functionalize Quercetin loaded Fe_3O_4 fabricated Mesoporous SBA-15 *in vitro* and *in vivo.*

References:

1. Cooper GM, The Cell: A Molecular Approach, 2000.

2.A.Fadaka,B.Ajiboye,O.Ojo,O.Adewale,I.Olayide,R.Emuowhochere,*Journal of Oncological Sciences*,2017,3,2,45-51.

3. F.Inchingolo, L.Santacroce, A.Ballini, S.Topi, G.Dipalma, K.Haxhirexha, L.Bottalico, I. A.Charitos, *International journal of environmental research and public health*, 2020,17(9).

4. A. Boardman, G. Bavikatte,*BJMP*,2020,13(1):a007

5. G. B. Faguet,*International journal of cancer*,2015,136,9,2022-2023.

6. P.Baláž, J.Sedlák ,*Toxins*, 2010,2(6), 1568–1581.

7. S. H. Yan, *Chinese journal of cancer*, 2013, 32(9), 475–477.

8. R. Sullivan, O. I. Alatise, B. O. Anderson, R. Audisio, P. Autier, A. Aggarwal, C. Balch, M. F. Brennan, A. Dare and A. D'Cruz, Lancet Oncol., 2015, 16, 1193–1224.

9. A. victor,*Cancer research*,1965,2,25

10. J. M. L. Stephens,*University of British Columbia*,2018.

11.R. D. Smith , M. K. Mallath , *Journal of Global Oncology* ,2019,5,1-15.

12. F.Balloux, L.van Dorp,*BMC biology*,2017, 15(1), 91.

13. A. Abercrombieande. J. Ambros,*American Association for Cancer Research*,22.

14. P.Kumar,F. A.Murphy,Emerging infectious diseases, 2013,19(4), 661–663.

15. N.Parsa ,*Iranian journal of public health*, 2012,41(11), 1–9.

16. C.Vrinten, L. M.McGregor,M.Heinrich, C.von Wagner, J.Waller, J.Wardle, & G. B.Black,*Psycho-oncology*,2017 26(8),1070–1079.

17.C.Morgan,M.Cira,A.Karagu,F.C.Asirwa,N.R.Brand,N.BuchananLunsford,S.M.Dawsey,A. Galassi,A.Korir,L.Kupfer,P.J.Loehrer,D.Makumi,L.Muchiri,S.Sayed,H.Topazian,J.Welch,M. J.Williams,K.Duncan, *Journal of Cancer Policy* ,2018,17,38-44.

18.V.T. DV. Jr., E Chu,*cancerresearch*,2008,68, 21.

19. RL.Siegel, KD.Miller, A.Goding Sauer, SA.Fedewa, LF.Butterly, JC.Anderson, A.Cercek, RA. Smith, A.Jemal,*CA Cancer J Clin.*,2020,70(3):145-164.

20. L.Stark, C.Tofthagen, C.Visovsky, S. C.McMillan, *Journal of hospice and palliative nursing*, 2012,14(1), 61–70.

21. F. A.Haggar,R. P.Boushey, *Clinics in colon and rectal surgery*, 2009,22(4), 191–197.

22.V. Arndt , H. Merx , C.Stegmaier , H. Ziegler , H. Brenner ,*Journal of Clinical Oncology* ,2004,22,2,4829-4836.

23. J.Kenig, P.Richter,*Videosurgery and other miniinvasive techniques*, 2013,8(3), 183–186.

24. R.Paduch,*Cellular oncology (Dordrecht)* ,2016,39(5), 397–410.

25. M.Riihimäki, A.Hemminki, J.Sundquist,K.Hemminki,*Scientific reports*,2016, 6, 29765.

26. P.Rawla, T.Sunkara,A.Barsouk,*Przegladgastroenterologiczny*, 2019,14(2), 89–103.

27. P. S.Patil, A.Saklani, P.Gambhire, S.Mehta, R.Engineer, A.De'Souza, S.De'Souza, M.Bal, *Indian journal of surgical oncology*, 2017,8(4), 484–490.

28. K.Bogos, Z.Kiss, G.Gálffy, L.Tamási, G.Ostoros, V.Müller, L.Urbán, N.Bittner, V.Sárosi, A.Vastag, Z.Polányi, Z.Nagy-Erdei, Z.Vokó, B.Nagy, K.Horváth, G.Rokszin, Z.Abonyi-Tóth, J.Moldvay, Frontiers in oncology,2019, 9, 1051.

29. DK. Kinney, DH.Barch, B.Chayka, S.Napoleon, KM.Munir,*Med Hypotheses*, 2010,74(1):102-6.

30. H. A.Loomans-Kropp, A.Umar, *Journal of cancer epidemiology*, 2019, 9841295.

31.M.Ryan-Harshman,W.Aldoori,*Canadian family physician Medecin de famillecanadien*, 2007,53(11), 1913–1920.

32. A. T.Kunzmann, H. G.Coleman, W. Y.Huang, C. M.Kitahara, M. M.Cantwell, S. I.Berndt,*The American journal of clinical nutrition*, 2015,102(4), 881–890.

33. J. M.Ridlon, D. J.Kang, P. B.Hylemon, J. S.Bajaj,*Current opinion in gastroenterology*,2014, 30(3), 332–338.

34. A.A.Moghaddam, M.Woodward, R.Huxley,*Cancer Epidemiol Biomarkers Prev.*,2007,16(12):2533-47.

35. S. Y. Guraya, *World journal of gastroenterology*, 2015,21(19), 6026–6031.

36. B. M.Cheung, C.Li,Current atherosclerosis reports, 2012,14(2), 160–166.

37. T.Tanaka,*Journal of carcinogenesis*, 2009,8, 5.

38. R.Wong, *Advances in pharmacological sciences*, 2019, 3418975.

39. K. W.Jasperson, T. M.Tuohy, D. W.Neklason, R. W.Burt,*Gastroenterology*,2010, 138(6), 2044–2058.

40. J.Wehkamp, M.Götz, K.Herrlinger, W.Steurer, E. F.Stange,*Deutsches Arzteblatt international*, 2016,113(5),72–82.

41. C. J.Karvellas, R. N.Fedorak, J.Hanson, C. K. Wong, (2007). *Canadian journal of gastroenterology* , 21(7), 443–446.

42. T. T.Vo, A.Letai, *Advances in experimental medicine and biology*, 2010,687, 49–63.

43. H.Ashktorab, H.Brim, *Current colorectal cancer reports*, 2014,10(4), 425–430.

44. National Health Commission Of The People's Republic Of China, *Chinese journal of cancer research*,2020, 32(4), 415–445.

45.. J. K.Patra, G.Das, L. F.Fraceto, E.Campos, M.Rodriguez-Torres, L. S.Acosta-Torres, L. A.Diaz-Torres, R.Grillo, M. K.Swamy, S.Sharma, S.Habtemariam, H. S. Shin, *Journal of nanobiotechnology*,2018, 16(1), 71.

46. S.Rizvi, A. M.Saleh,Saudi pharmaceutical journal,2018,26(1), 64–70.

47. N.Mody, R. K.Tekade, N. K.Mehra, P.Chopdey, N. K.Jain, *AAPS PharmSciTech*, (2014). 15(2), 388–399.

48. F. Zhao, H. Liu,S. D. R. Mathe ,A. Dong,J Zhang,*Nanomaterials* ,2018, *8*(1), 15.

49.S. Senapati, A. K. Mahanta,S. Kumar,P.Maiti ,*Signal Transduction and Targeted Therapy*,2018,3,7.

50. F.ud.Din,W. Aman, I.Ullah, O.S.Qureshi, O. Mustapha,S.Shafique, A Zeb,*Int J Nanomedicine*,2017, 12, 7291–7309.

51. F. U.Din, W.Aman, I.Ullah, O. S.Qureshi, O.Mustapha, S.Shafique, A.Zeb,,*International journal of nanomedicine*,2017, 12, 7291–7309.

52. R.Sensenig, Y.Sapir, C.MacDonald, S.Cohen,B.Polyak, *Nanomedicine* ,2012,7(9),1425–1442.

53.C. Zhang, Y. Yan,Q.Zou, J. Chen , C LI, *Asia-Pac J ClinOncol*,2016, 12,13–21

Biological Material & Methods...

a. Cell Lines and Chemicals:

Human colorectal carcinoma (HCT 116),Human hepatocellular carcinoma(Hep G2), Human small lung carcinoma (A549), Human pancreatic carcinoma (MIAPaCa-2), Murine colorectal carcinoma (CT-26), and human embryonic kidney (HEK-293) cell lines were procured from National Centre for CellSciences (NCCS),Pune, India. Components of cell culture media viz.fetal bovine serum (FBS),Dulbecco's Modified Eagle Medium (DMEM), trypsin,Penicillin-Streptomycin-neomycin (PSN) antibiotic cocktail, and ethylenediaminetetraacetic acid (EDTA) were obtainedfrom Gibco (Grand Island, NY, USA). Other raw and fine chemicalswere purchased from Sigma-Aldrich, St. Louis, MO, USA, and Sisco Research Laboratories (SRL), Mumbai,India. Primary Antibodieswere bought from Santa Cruz Biotechnology, Dallas, Texas, USA andeBioscience, San Diego, USA. Fluorescence tagged secondary antibodies were procured from Abcam, Cambridge, United Kingdom. Dyes were obtained from Thermo Fisher Scientific, United States. Other antibodies were purchased from Cell Signaling Technology, United States.

b. Cell Culture:

HCT 116, Hep G2, HCT 116, A549, MIAPaCa-2 and HEK-293 cells were cultured in DMEM carrying 10% FBS with1% antibiotic cocktail in a humidified condition under constant 5% CO2 at 37 °C. After reaching 70−75% confluence, cell seeding was completed with EDTA (0.52 mM) and trypsin (0.25%) in phosphate-buffered saline (PBS) and plated at a required density to permit them to re-equilibrate before the experiment(1). All of the thesis work has followed the above cell culture protocol.

c. Determination of Cell Viability:

Determination of cell viability was done by MTT [(4,5- dimethyl-thiazol-2-yl)-2,5-diphenyl-tetrazolium bromide] assay. Cells were seeded at a required density (4×10^3 cells/well) in a 96-well plate. After 18−24 h of seeding, cells were treated with respective material for the particular duration. After the treatment, plates were placed in an incubator at 37 °C in a humidified CO_2-rich condition (5%). After incubation for proper time duration cells were rinsed from each well of 96 well plate by PBS and then the MTT solution was added to each

well and reserved in an incubator for 4 h to appear formazan salt. The formazan salt was then solubilized using DMSO and the absorbance was taken at 595 nm using an ELISA reader (Emax, Molecular device, USA) (2).Cell propagation was evaluated from the absorption intensity. Cell viability wasdetermined as follows:

$$\text{Cell viability} = \frac{\text{OD of Control} - \text{OD of treated}}{\text{OD of Control}} \times 100$$

In every case, the samples were sonicated before treating in a cell line to obtain homogenized mixtures. The final reported biological data were represented after repeating the experiments in triplicate.

d. Detection of Apoptosis/Necrosis:

Necrotic and Apoptotic cell death was determined using the Annexin-V FITC/DAPI apoptosis detection kit (Calbiochem, CA, USA). Briefly, the cells cells were plated in six well plates then treated with certain dose of materials (obtained from MTT assay). After proper time of incubation, the cells were washed and stained with DAPI/PI and Annexin-V-FITC in accordance with the manufacturer's directions (3). The percentages of apoptotic (early and late), live, and necrotic cells were analyzed using a flow cytometer (BD LSRFortessa TM San Jose, CA, USA). The acquired data were analyzed using Flow Jo (Version 10.0) software.

e. Assessment of Intracellular ROS:

This has been previously reported that mitochondrial ROS is one of the key signaling molecules for apoptosis. So, we have calculated the ROS level. To decide the intercellular ROS, we incubated the treated cells with 2′,7′-dichlorofluoresceinDiacetate (DCF-DA) of 10 μM at 37 °C for 25 min before the analysis by the flow cytometer (BD LSRFortessaTM, San Jose, CA, USA)equipped with FlowJo software (4). The increase of DCF fluorescence is the symbol of generated ROS inside cells, which was signified as mean fluorescence intensity of DCF.

f. Quantification of intracellular hydroxyl radical (°OH) accumulation using flow cytometry:

Earlier reports have revealed that amongst the several free radicals, the hydroxyl radical is frequently found cellular free radical that is produced through oxidative stress, and causes cell death (5).Intracellular hydroxyl radical (°OH) accumulation was calculated by hydroxyphenyl fluorescein (HPF), a specific indicator which reacts particularly with hydroxyl radicals (6). HPF exhibits bright green fluorescence (excitation/emission maxima 490/515 nm) upon oxidation. The treated cells (2×10^6 cells) were incubated with HPF for 30 min in the dark followed by acquisition using a flow cytometer (BD LSRFortessaTM San Jose, CA, USA) (7). The acquired data were analyzed using Flow Jo (Version 10.0) software.

g. Detection of nuclear fragmentation and condensation by fluorescence microscopy:

To observe nuclear fragmentation or chromatin condensation, control ells with or without the treatment of respective material were stained with Acridine orange (50 mg/ml) and ethidium bromide (50 mg/ml) for 10min (8). The images were taken with an inverted phase contrast microscope (OLYMPUS IX 70, Olympus Optical Co. Ltd, Sibuya-ku, Tokyo, Japan). Then the images were analyzed using ImageJ software. The emission was collected at 525 nm and 605 nm upon excitation at 488 nm.

h. Measurement of nuclear DNA in various phases of the cell cycle:

Quantification of nuclear DNA in various phases of the cell cycle was measured by flow cytometry. After the treatment with respective material, the harvested cells werefixed overnight at 4 °C in 70% cold ethanol. Then centrifugation was completed. After that the cells were resuspended in PBS containing25 mg/ml RNase. Then the tubes were left for incubation at 37 °C for 1 h. Cells were then stained with Propidium iodide (PI) (50 mg/ml) at 4 °C for 15min(3).The stained nuclear DNA was analyzed using a flow cytometer(BD LSRFortessaTM, San Jose, CA, USA).

i. Assessment of Protein Expression by Flow Cytometry:

Treated and untreated Cells were fixed in paraformaldehyde (4%) in PBS (pH 7.4) for 20min at room temperature followed by permeabilization (0.1% TritonX-100 in PBS) with 0.1% FBS for 5 min. The permeabilized cells werethen washed twice using PBS with 3% FBS and

incubated with respective rabbit/mouse/goat/donkey raised primary antibody for overnight. Further,the primary antibody labelled cells were incubated with fluorophore conjugated anti-rabbit/anti-mouse/anti-goat/anti-donkey IgG as a secondary antibody on ice for 2h and the stained cells were subjected to flow cytometricanalysis using a BD LSRFortessaTM flow cytometer (Becton Dickinson,Franklin Lakes, NJ, USA) equipped with FlowJo software(9).

j. Alteration in Mitochondrial Membrane Potential by Flow Cytometry:

Treated and Untreated cells were incubated with thecationic carbocyanine dye, JC-1 (5,5′,6,6′-tetrachloro-1, 1′, 3, 3′-tetraethylbenzimidazolylcarbocyanine iodide) after two time wash by PBS. Then the tubes were subjected to flow cytometricanalysis according to the manufacturer protocol. JC-1 displaypotential dependent accumulation in mitochondria and show afluorescence emission shift from green (525 nm) to red (590 nm)(10).The fluorescence change, therefore, allows determining the percentageof hyperpolarized and depolarized mitochondria on the basis of theresultant fluorescence of JC-1 aggregate and monomer.

k. Western Blot Analysis:

Immunoblotting is a extensively used method used to recognize specific proteins(11). Briefly, the celllysate was separated by SDS-PAGE (10−15%) followed by anoptimized transfer to PVDF membranes (Millipore, Bedford, MA)(12).The membranes were then blocked using 5% bovine serum album(BSA) for 2 h and incubated overnight with respective rabbit/mouse raised primary antibodies at 4°C and β-Actin was used as a loading control(13). Further, the membrane waswashed before the incubation with alkaline phosphatise conjugatedsecondary antibodies for 2 h at room temperature. At last, theresultant protein appearance was visualized by chromogenicsubstrates, NBT-BCIP(12). The intensities of every immunoblot werecalculated using ImageJ software and represented as mean relativeintensities of each protein.

l. DNA Fragmentation Assay:

Cells were treated with the respective material at different concentrations for several duration and the resultant fragmented DNA was calculated using commercially obtainable kits according to the manufacturer procedure(14).

m. Comet assay:

The oxidative DNA damage was inspected by executing the Comet assay(15). The treated cells were mixed with 100 ml of 0.5%low melting agar (LMA) at 39 ℃ and then spread on a fully frosted microscopic slide pre-coated with 1% LMA. After agarose solidification, the slide was covered with 75 ml of0.5% LMA and immersed in lysis solution (10 mM Tris, 2.5 M NaCl, 100 mM Na-EDTA, 10% DMSO and 1% TrionX-100, pH 10) at 4 ℃ for 1 h. The slides were positioned in a gel-electrophoresis apparatus containing for 40 min at 300 mM NaOH (pH 13) and 10 mM Na-EDTA to permit DNA unwinding and the expression of alkali labile damage. An electrical field was applied (25 V,300 mA) at 4 ℃ for 20 min to draw negatively charged DNA towards an anode. After electrophoresis, the slides were washed three times at 4 ℃ for 5 min in a neutralizing buffer (0.4 M Tris pH 7.5) and then stained with 75 ml EtBr solution (20 mg/ml). The slides were photographed using a fluorescence microscope and the images were analyzed by Comet Score software (v1.5) (4).

n. Caspase-3 and Caspase-9 Activity Assays:

Treated cells were allowed to caspase-3 and caspase-9 colorimetric assay using commercially available kits according to the manufacturer instruction(BioVision Research Products, Mountain View, CA) respectively(16).

o. In vitro MRI:

For checking the Therapeutic nature of Magnetic Nano-composite, Magnetic Resonance Imaging (MRI) experimentation was planned. In vitro cellular MR imaging experimentation was completed with HCT 116, A549 and HEK 293 cell line. HCT 116, A549 and HEK 293 cells (6×10^3) were incubated in a 96-well plate. After proper adherent, cells were treated with the magnetic composite at various concentrations and kept for 3 h. Then, the cells were washed three times by PBS and fixation was completed by using paraformaldehyde. For avoiding air exposure, low melting agarose (2%) was added to each well. Then, the plate was incubated at 4 ℃ to freeze the cell suspensions. The MRI was completed under a 3T clinical

MRI scanner(Siemens MAGNETOM Verio) using a pre-fabricated sample holder. MR phantom images were acquired by applying a spin-echo multi-section pulse sequence. The MRI signal intensity (SI) and visualization of the phantom images were examined by using the standard software provided by the manufacturer (17).

p. Quantification of protein expression/localization using Immunofluorescence:

Briefly, the treated/control cells were washed twice for 10 min each in PBS, and incubated in blocking solution containing 2% normal bovine serum for 1 h and 0.3% Triton X-100 in PBS. After the blocking, the cells were left for incubation overnight at 4 ºC with the respective primary antibody, followed by washing and incubation with their respective fluorophore-conjugated secondary antibodies for 2 h. The slides were then counterstained with DAPI for 10 min, and mounted with the Prolong Anti-fade Reagent (Molecular Probe, Eugene, OR, USA). Stained cells were examined using a Confocal laser-scanning microscope (FV 10i, Olympus, Japan)(18).

q. Animals:

Adult male BALB/c mice ranging from 8 to 10 weeks old with initial body weights of 20–22 g were obtained from our institutional facility. The animals were reserved under standard laboratory conditions of 21 ºC, relative humidity of 55%and 12 h : 12 h light : dark cycle maintained during the experiment. Standard rat pellets and tap water adlibitum were given to the animals. All investigational protocols were performed by the guideline of the Institutional Animal Ethics Committee, CSIR Indian Institute of Chemical Biology and accepted by the Committee for the Purpose of Control and Supervision of Experiments on Animals (CPCSEA), Ministry of Environment, Forests and Climate Change, Government of India.

r. In vivo experimentation:

On the 1st day, the animals were shaved on the back flank. Each mouse was injected subcutaneously in the shaved right flank with CT-26 (2×10^6) in PBS. Eight days after tumor implantation, the animals were randomly divided into four groups as follows (5 mice in each group) (Fig. 1):

Group I: served as control and mice in this group were kept at a standard ambient temperature of 24 ± 2 ºC and 60–70%relative humidity.

Group II: CT-26 tumor-bearing mice treated with normal saline.

Group III: CT-26 tumor-bearing mice treated with QN (15 mg/kg) intraperitoneally for six alternate days.

Group IV: in this group, mice were injected with FA-IO-SBA-15-QN (15 mg /kg) intraperitoneally for six alternate days.

The resultant tumor length, as well as the weight, was measured after the completion of the experimentation. In addition, the animal survival rate was evaluated for up to 30 days.

s. Tumor morphological analysis using histology:

The harvested tumor tissue was dipped in 10% formalin andprocessed routinely in paraffin. Then, the 5 mM thick slices wereprepared and stained with H&E for histological analysisaccording to the standard protocol(19).

t. Determination of protein expression using Immunofluorescence:

The unstained tumor slice of 6 mm of thickness of all experimentalgroups was analyzed through indirect Immunofluorescence(20).Briefly, the sections were deparaffinised and hydratedin graded ethanol, followed by blocking (0.3% hydrogenperoxide) for 20 min to mask the endogenous peroxidise activity. A microwave oven was used to retrieve the antigen using citrate buffer (10 mM, pH 6.0) at temperatures ranging between 95 ºC and 98 ºC for 15 min, and then the section was further blocked with BSA (5%) at 37 ºC for 30 min. The sectionswere incubated with the respective primary antibody (Dilution: 1: 250) at 4 ºC for overnight. After washing the samples with PBS, the sections were incubated with anti-rabbit/mice-AF546, and AF647 secondary antibody for 1 h each at 37 ºC, followed by nuclear staining with DAPI for 10 min. The images were taken using an Olympus FV1000 MPE SIM Laser (21).

u. In vivo MRI:

Tumor-bearing mice were injected with the proper composite (at proper dose) via a tail vein. Adding up, magnetic targeting was used to half of these mice. MRI was performed using a 3T MRIscanner (Sigma; GE Medical Systems, Milwaukee, WI, USA). The MR images were calculated by a T2-weighted spin-echo sequence (TR/TE=4000/108 ms; slice thickness, 2 mm; slice spacing, 1mm; matrix, FOV, 256×256; 8 cm×8 cm). Signal variation was observed following the injection of nanocarriers for 1 h (22).

v. Analysing of Tumor morphology by using histology:

The harvested tumor tissue was dipped in 10% formalin and processed regularly in paraffin. After that, the 5 mM thick slices were prepared and stained with H&E for histological examination according to the standard protocol l(23).

w. References:

1. G. Kulsi, A. Sannigrahi, S. Mishra, K. D.Saha, S.Datta, P.Chattopadhyay,K.Chattopadhyay,*ACS Omega* **2020** *5* (27), 16395-16405

2. M. Price, J. J. Reiners, A. M. Santiago,D. Kessel, *Photochem. Photobiol.*, 2009, 85, 1177–1181.

3. A. Nandy, S. K. Dey, S. Das, R. N. Munda, J. Dinda,K. D. Saha, *Mol.Cancer*, 2014, 13, 1.

4. I. Vermes, C.Haanen, H. Steffens-Nakken ,C. Reutellingsperger, *J. Immunol. Methods*, 1995, 184, 39–51.

5. Pham-Huy, L. A., He, H., Pham-Huy *International journal of biomedical science :IJBS*, 2008,*4*(2), 89–96.

6. M. Price,J. JReiners,A M Santiago,D.Kessel, *Photochemistry and Photobiology*,2009,85(5):1177-81

7. D. J. Dwyer, M. A. Kohanski, B. Hayete , J. J. Collins, *Mol.Syst. Biol.*, 2007, 3, 91.

8. J. C. Kern and J. P. Kehrer, *Chem.-Biol. Interact.*, 2002, 139,79–95.

9. K. Manna, U. Das, D. Das, S. Kesh, A. Khan, A. Chakraborty, S. Dey, *Free Radical Res.*, 2015, 49, 422–439.

10. J. Gu, H. Xu, Y. Han, W. Dai, W. Hao, C. Wang, N. Gu, H. Xu, J. Cao, *Sci. China Life Sci.*, 2011, 54, 793–805.

11. Y. Zhang, B. C. Y. Cheng, R. Xie, B. Xu, X. Y. Gao, G. Luo,*RSC Adv.*, 2019, 9, 8912–8925.

12.K. Manna, A. Khan, D. K. Das, S. Bandhu Kesh, U. Das,S. Ghosh, R. Sharma Dey, K. Das Saha, A. Chakraborty,S. Chattopadhyay, S. Dey and D. Chattopadhyay, *J.Ethnopharmacol*., 2014, 155, 132–146.

13. T. Mahmood, P. C. Yang,*North American journal of medical sciences,* 4(9), 429–434.

14. P.Majtnerová , T.Roušar ,*Molecular Biology Reports* ,2018,45,1469–1478

15. A. Azqueta, J. Slyskova, S. A. Langie, I. O'Neill Gaivão,A.Collins,*Frontiers in genetics*,2014 5, 288.

16. K. Manna, A. Khan, S. Biswas, U. Das, A. Sengupta,D. Mukherjee, A.Chakraborty ,S. Dey, *RSC Adv.*, 2016,6, 23058–23073

17. R. Nandi, S. Mishra, T. K. Maji, K. Manna, P. Kar, S. Banerjee,S. Dutta, S. K. Sharma, P. Lemmens, K. D. Saha ,S. K. Pal, *J. Mater. Chem. B*, 2017, 5, 3927–3939.

18. S. K. Das, S. Mishra, K. Manna, U. Kayal, S. Mahapatra,K. Das Saha, S. Dalapati, G. P. Das, A. A. Mostafa,A.Bhaumik, *Chem. Commun.*, 2018, 54, 11475–11478.

19. V. Picco , G. Pag`es, *Genes Cancer*, 2013, 4, 360–368.

20. Y. Zhang, B. C. Y. Cheng, R. Xie, B. Xu, X. Y. Gao, G. Luo, *RSC Adv.*, 2019, 9, 8912–8925.

21. S. B. Kesh, K. Sikder, K. Manna, D. K. Das, A. Khan, N. Das, S. Dey, *Life Sci.*, 2013, 92, 938–949.

22. E. Li, Y. Yang, G. Hao, X. Yi, S. Zhang, Y. Pan, B. Xing, M. Gao, *Nanotheranostics*, 2018, 2, 233–242.

23. V. Picco and G. Pages, *Genes Cancer*, 2013, 4, 360–368.

Chapter-1

Quercetin loaded Folic acid-conjugated magnetic mesoporous silica nanoparticles: a Theranostic application for Colon cancer

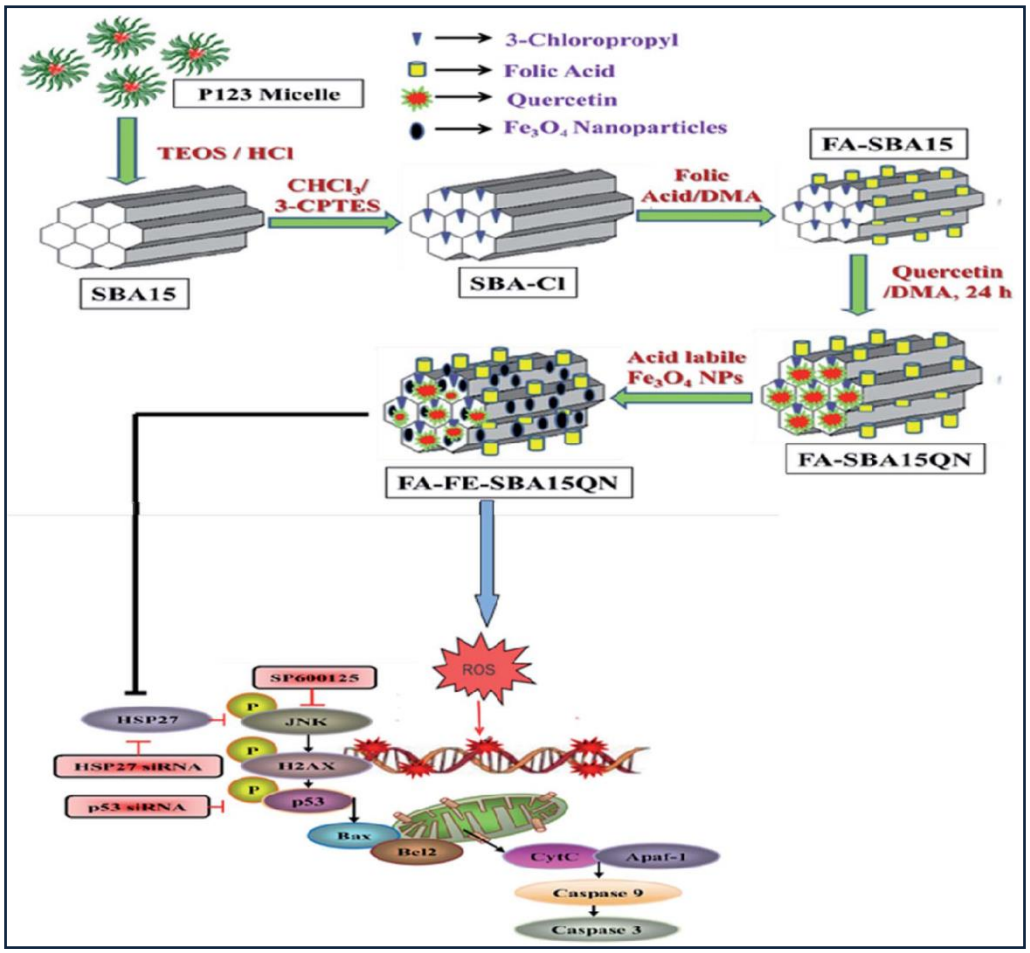

1.1. Introduction

Cancer is accumulation of more than hundred diseases, that mature with time and blast out with uncontrolled alter cell division (1). All starts when a cell breaks free from normal cell cycle demarcations and follows its self-proliferation strategy. Every cancer has own unique features but fundamental features are quite similar and it is a major threat for both developing and developed countries. According to GLOBOCAN 2018, cancer ceased 9.6 million life in 2018. According to present GLOBCAN report Colorectum cancer is the third most noted

cancer after lung and breast and depicted high mortality rate (2). Surgical removal of tumor is not sufficient to overcome this disease. After surgery, chemotherapy, radiotherapy, immunotherapy, hormonal therapy is widely popular now (3). But patient survival rate is not promising and cost with a high degree of side effects. Chemotherapy is the most popular one, beside of its high side effects due to its systematic toxicity which causes a plethora of damage to healthy tissues, after surgery therapeutics. Radiation therapy has many drawbacks due to its non-specificity and non-selectivity nature (4). Combinational chemotherapy by using plant-based components may be a novel strategy to reduce disease sevearityand limits an associated complication (5).

Now a days natural occurring phytochemicals and secondary metabolites are widely used in therapeutics, due to their tissue specificity and tissue protective nature. Quercetin (3, 3′, 4′, 5, 7-pentahydroxy-2-phenylchromen-4-one), a naturally occurring aglycone flavonoid, contains a group of polyphenols with a flavonol core, extracted from several plant sources, viz fruits, leaves, roots, and barks. As its unique biological properties, Quercetin can improve disease resistance and overall health, including antioxidant, anti-inflammatory, anti-carcinogenic, antiviral, and antibacterial activities (6). Quercetin (QN) also can restrict lipid peroxidation, platelet aggregation. An ample range different cellular effects and associated with multiple signaling pathways which are essential in the regulation of physiological processes are turnd on with Quercetin inoculation. QN can inhibit tyrosine kinase (PTK) signaling pathways that reflect as suppression of tumor. PTK is augmented in the primary cellular response at the period of cancer cell maturity (7). Besides the anti-cancer property, the anti-inflammatory effect of QN is consigned in inhibiting inducible nitric oxide synthase (iNOS), followed by cytokine production, prostaglandin synthesis. QN can attenuate several pro-inflammatory cytokine secretions by directly communicating with the components of mitogen-activated protein kinase (MAPK), and nuclear factor kappa-light-chain-enhancer of

activated B cells (NF-κB),important inducers of inflammatory gene expression. Surprizingly it is reported that, QN indirectly prevent inflammation by increasing peroxisome proliferator-activated receptor gamma (PPARγ) activity (8). It is well defined that QN is proficient at inducing apoptotic cell death in various carcinoma including cervical, squamous, colon, pancreatic, leukemia, breast, lung, and hepatocellular cells. QN-guided apoptosis is primarily demonstrated through the mitochondrial pathway which includes an imbalance of pro/anti-apoptotic protein and the activation of selective cysteine-aspartic proteases (caspases-3, -9) (9). In contempt of an extensive range of biological effects, the physicochemical properties of QN represent a limit for its application. The low water solubility, followed by low bioavailability as well as low oxidative stability and intensive biotransformation confines its applicability. Therefore, different approaches have been taken,andenormous research is going on to improve its delivery and efficiency (10).

Currently, mesoporous silica nanoparticles (SBA-15) is widely used for improved and targeted drug delivery which open up new possibilities in nanomedical research (11). The diffusion process generally directs the liberation of the drug from SBA-15. Thus, the release profile may be coustomised by altering pore diameter. Interaction of the encapsulated drug with the pore wall of SBA-15 may beexecute an essential role in drug release which is dependent on the relative amount and obeys the rule of displacement desorption.Folate receptor (FR), is predominant in colon carcinoma, is a potential target for drug delivery and imaging purpose. That increase tumor specific drug release very effectictively and reduce sideeffects. Previous reports have been we documented that FA can be readily attached through amide reactions with the outer surface of SBA-15 (12).

Magnetic resonance imaging (MRI) is a prevailing technique for diagnostic and analyzing tomographic images of tumor, as it offers an amalgamation of three-dimensional tumor coverage and deep tissue penetration. Presentlyvarious research has been carried out

to develop novel MRI contrast agents but the single mode contrast agents are still unmade. Current contrasting agents displayed fundamental limitations in terms of imaging artifacts, imaging uncertainties, and health risks. Researchers are vigorously studies to develop functionalized contrasting agent that can be useful for cancer management (13).

The present study was aimed to explore a novel Theranostic platform which includes three major components to enable a “dual sword”: (i) targeted and enhanced QN loading and regulates its release using external and internal triggers (pH), (ii) provide imaging capability with a suitable contrasting agent (Fe_3O_4) (14). The current study was also designed to explore the prolonged efficacy of QN with the evaluation of possible molecular mechanism.

1.2. Reagents and Methods: Synthesis

1.2.1. Chemicals:

P123 (Poly(ethylene glycol)-block-poly(propylene glycol)-block-poly(ethylene glycol), TEOS (tetraethyl orthosilicate) and 3-chlorooopropyltriethoxysilane (3-CPTES) were purchased from Sigma Aldrich, India. Folic acid (M = 441.4 g/mol), and quercetin (M = 302.236 g/mol) were procured from Sigma Aldrich, India. All other organic solvents were used as received without further purification.

1.2.2. Synthesis of mesoporous 3-chloropropyl-functionalized SBA-15 (SBA-Cl):

Pure SBA-15 material was synthesized using P123 as a structure directing agent in the presence of HCl and tetraethyl orthosilicate as a silica source (15). The as-synthesized material was calcined at 623 K to remove the template P123 molecules. Then calcined SBA-15 (1.0 g) was dispersed in a round bottom flask (100 mL) containing $CHCl_3$ (50 mL). 3-chloropropyltriethoxysilane (3-CPTES) (1.2 g) was then added into the dispersed solution. The resulting solution mixture was allowed to stir continuously at room temperature for about 36 h under nitrogen atmosphere. After completion of the reaction, the solid product was filtered through simple filtration technique and washed with excess chloroform and finally dried in air to obtain SBA-Cl (16).

1.2.3. Synthesis of folic acid-functionalized SBA-15 (FA-SBA-15):

Briefly, solid white SBA-Cl (1.5 g) was further dispersed in dimethylacetamide (DMA) (25 ml) and of folic acid (250 mg) was added to this reaction mixture. Then it was allowed for reflux at 160°C for 36 h. Finally, the pale yellow colored solid product was filtered and washed with copious amount of distilled water to relieve of unreacted folic acid from the functionalized material. The resulting solid was dried in the oven at a 75ºC temperature and subjected for characterization (**17**).

1.2.4. Quercetin Loading:

FA functionalized SBA-15 particles were added into Quercetin (QN) solution and incubated in a shaker at room temperature overnight. QN molecules could diffuse in solution into the pore channels. The QN-loaded SBA-15 was taken out by centrifugation and rinsed with water to get rid of the redundant QN. Finally, the resulting particles were washed with water and dried in vacuo at 60°C to yield QN-loaded folate (FA) functionalized SBA-15. The amount of

QN-loaded into FA-functionalized SBA-15 was estimated by UV-VIS spectroscopy at 369 nm (λ_{max}=369 nm).

$$Loading\ Content = \frac{Initial\ weight\ of\ QN - Supernatant\ weight\ of\ QN}{Weight\ of\ particles} \times 100\%$$

1.2.5. Synthesis of Fe_3O_4 (IO) :

Iron (II) chloride tetrahydrate and iron (III) chloride hexahydrate was measured 2.50×10^{-3} and 2.99×10^{-3} mol respectively and added into a vigorously stirred deoxygenated aqueous solution (600.0 mL, pH~1.5). Then ammonium hydroxide (1.50M) was added dropwise to the aqueous solution of iron (II) and iron (III) solution. Addition of ammonium hydroxide was continued till the pH reached 11.0 from 1.5. As the pH will increase (from 1.5 to 11.0), a black precipitate of magnetite (Fe_3O_4) formed simultaneously. The black precipitate was separated by magnetic decantation then five times washing was completed by water. Ethanol was used for collecting the dried Fe_3O_4 power before evaporating. Then the powder Fe_3O_4 was collected (18).

1.2.6. Embedding of IO into QN-loaded FA-functionalized SBA-15 composite (FA-IO-SBA-QN):

To transfer Fe_3O_4 nanoparticles into an aqueous phase, dispersion of nanoparticles (1.2 mL in chloroform) was mixed with the CTAB solution (0.8 g in 20 ml water) and then stirred at 60°C for 2 h. Then, the mixture was filtered through a 0.44 μm syringe filter to remove large aggregates. The filtered solution and NaOH (2 M, 175 μl) solution was diluted with deionized water (22 mL), followed by heating to 70°C. After stirring for 10 min at 70°C monodispersed Fe_3O_4 was added to FA-IO-SBA-15-QN and kept it for overnight under magnetic stirring for overnight. Then, it was centrifuged (13,000 rpm, 10 min) to remove the unbounded Fe_3O_4 and dried to evaporate the solvent. The dried FA-IO-SBA-15-QN was characterized.

1.2.7. Characterization:

Nitrogen adsorption/desorption analysis was carried out by using a Quantachrome Autosorb 1-C surface area analyzer at 77 K. Prior to gas adsorption; a sample was degassed for 8 h at 403 K under high vacuum. NLDFT pore size distribution method was employed to determine the average pore size of the samples from their respective N_2 sorption isotherm using the silica/cylindrical pore model as a reference. The powder X-ray diffraction patterns were recorded on a Bruker D8 Advance SWAX diffractometer, which was operated at 40 kV voltages and 40 mA current. The instrument has been calibrated with a standard silicon sample, using Ni-filtered Cu Kα (λ=0.15406 nm) radiation. For TEM analysis, 10 mg of material was dispersed into absolute ethanol for 5 min. under sonication. Then one drop of the dispersed solution was dropped onto the carbon-coated copper grid and dried before analysis in the air. FT-IR spectra of the samples were recorded by using KBr pellets in a Perkin Elmer IR 783 spectrophotometer. Thermogravimetric analysis (TGA) and differential thermal analysis (DTA) of the sample were performed in a thermal analyzer TA-SDT Q-600 of TA Instruments under an air flow at a temperature ramp of 10 ºC/min. The carbon, hydrogen, and nitrogen (CHN) contents of different functionalized materials were determined in a Vario EL III elemental analyzer. ^{13}C CP MAS NMR study was carried out on a JEOL-ECA400NB 400 MHz spectrometer at resonance frequencies of 100.6 MHz

1.2.8. *In vitro* QN release assay:

The release of QN from the FA-IO-SBA-15-QN was studied using the dialysis bag diffusion method. 2 mL of sample were placed in the dialysis bag, sealed, and suspended in a beaker containing 40 mL of PBS, pH 3.5/5.5/7.4 in different time point (1-8 hr). The entire system was kept at 37°C with vigorous stirring on a mechanical shaking bath. Samples were withdrawn from the receptor media at predetermined time intervals and replaced with fresh buffer. The relative amount of QN in the samples was determined using UV-Vis spectrophotometer (Biorad, Hercules, California, USA) (19).

1.3. Results and discussion…

1.3.1. Characterization analysis of FA-IO-SBA-15-QN:

FTIR spectra of pure SBA-15, FA-SBA-15, and FA-IO-SBA-15-QN are potreyed in **Fig. 1A**. As depicted in the spectra, the additional transmittance peaks were noted in FA-IO-SBA-15-QN due to the presence of Fe_3O_4 at the surface of functionalized SBA-15. The small angle powder XRD patterns of four materials, *i.e.*,calcined SBA-15, SBA-Cl, FA-SBA-15, and FA-IO-SBA-15-QN are shown in **Fig. 1B**. As observed in **Fig. 1B**, pure SBA-15 material displayed three characteristic diffraction peaks at 2θ region (0.91, 1.58, and 1.82) for three distinctive planes (100) strong, (110) weak and (200) weak, respectively which suggested the presence of the ordered 2D-hexagonal mesoporous structure.In the 3-chloropropyl

functionalized material SBA-Cl also displayed similar diffraction pattern as portrayed in **Fig. 1B**. Hence, FA-SBA-15 depicted similar diffraction pattern with a 2θ value of 0.92, 1.56 and 1.83º degrees (**Fig. 1B**), corresponding to the above mentioned three characteristic planes, suggesting the retention of ordered 2D-hexagonal mesophase in the material.Minute increase in 2θ values indicated a minor decrease in d-spacing values, which confirmed the surface functionalization of SBA-15 base material. Contrastingly, in FA-IO-SBA-15-QN, the broad peak appears at a 2θ value of 20-23º due to amorphous nature of SBA-15 material and another broad and a sharp diffraction peaks were noted at a 2θ value of 9.27-15.53 and 18.19º, corresponding to the folic acid moiety bound at the mesopore surface. As elucidated **Fig. 1C**, the N_2 adsorption/desorption isotherms of FA-IO-SBA-15-QN at 77 K was observed. This isotherm could be classified to type IV isotherm with two steep rises in N_2 uptakes.This capillary condensation is more pronounced in the desorption isotherm, which showed large hysteresis. BET surface area and pore volume of this FA-IO-SBA-15-QN material were 402 m^2g^{-1} and 0.0737 ccg, sequentially. Pore size distribution plot was estimated from this sorption isotherm using the NLDFT model (**Fig. 1D**), and it displayed trimodal peak pores of 3.2, 5.0 and 7.6 nm. Three peak pores could be attributed to the stepwise functionalization of the 2D-hexagonal mesopores of SBA-15. Further, the ^{13}C CP-MAS (cross-polarization magic angle spinning) NMR of FA-SBA-15-QN was taken systematically. Chemical shifts of different carbon atoms corresponding to the folic acid and quercetin molecules are marked in **Fig. 1E**.

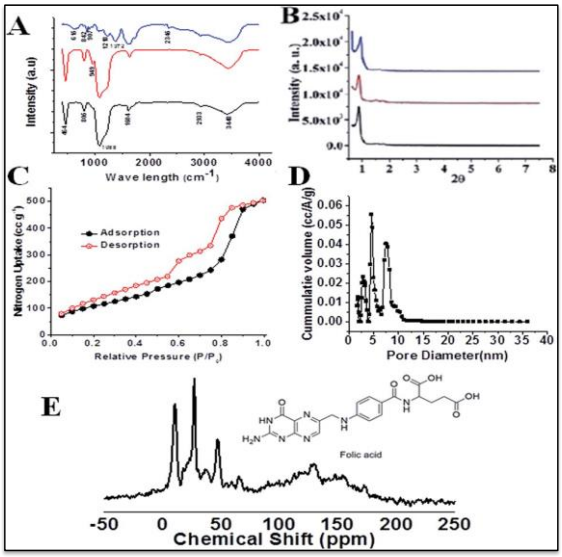

Fig. 1. Line graph representing (A) FTIR spectra, (B) XRD pattern, (C) N_2 adsorption and desorption isotherms, and (D) relative pore diameter of SBA-15, FA-SBA-15QN, and FA-IO-SBA-15-QN.

Thus, this solid-state^{13}C NMR data suggested successful functionalization of the surface of SBA-15 with FA and QN moieties. HRTEM images and SAED pattern of pristine SBA-15 and Fe_3O_4 NPs are shown in **Fig. 2**. SAED pattern of **Fig. 2B** suggested hexagonally order pore channels in SBA-15 material. In **Fig. 2E and 2F** HRTEM images of drug loaded FA-conjugated magnetic mesoporous silica material FA-IO-SBA-15-QN are shown. As seen in **Fig. 2A** and **2E** periodicity of hexagonal mesopores were retained in the QN-loaded functionalized SBA-15 material (20-22).

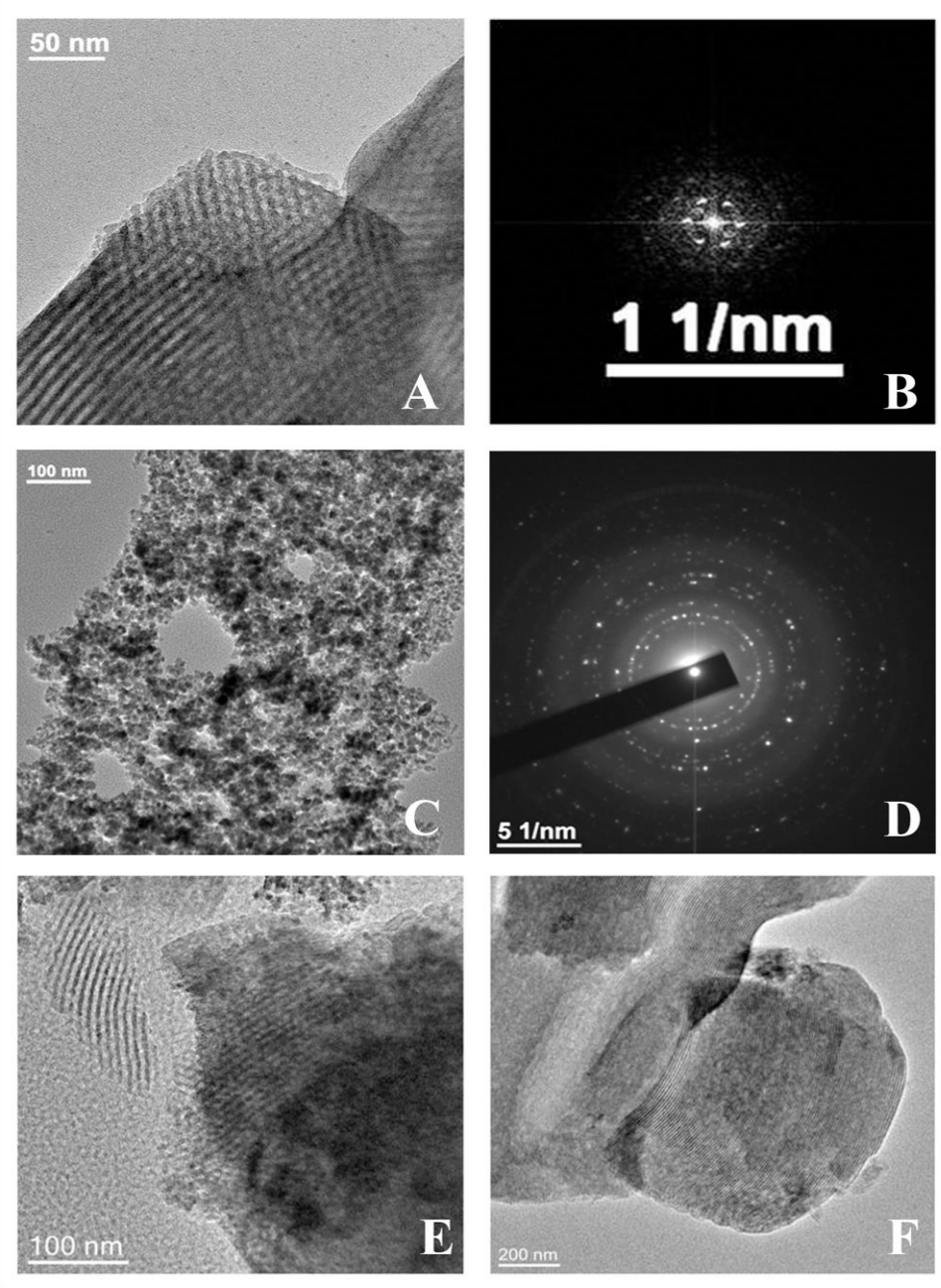

Fig. 2. Representative TEM image and SAED pattern of (A and B) SBA-15, (C and D) Fe_3O_4, and (E and F) FA-IO-SBA-15-QN. Scale bar: 50, 100, and 200 nm.

1.3.2. Analysis of pH-dependent release of QN from FA-IO-SBA-15-QNin a cell-free system:

The *in vitro* release behavior of conjugated QN from FA-IO-SBA-15-QN in response to physiological, tumor endosomal/lysosomal change was studied using a cell-free system, and the release pattern was estimated through fluorescence assessment. As shown in **Fig. 3B**, a gradual increase in QN release from FA-IO-SBA-15-QN was evident at pH 7.4, where 30.03% of QN was discharged from the SBA-15 core at 8 hr incubation. However, a slight decline in pH from 7.4 to 5.5 increased the QN liberation. 74.81% of QN was releasedafter 4 hr incubation, and the maximum peak (93.39%) was reached at 8 hr. In order to determine the effect of stomach pH ranging from 1.5 to 3.5 on QN release from SBA-15 nanopore, the release assay was also assessed using HPLC. In pH 3.5, the release of QN was not evident under the limit detection of HPLC due to the circumventing interaction with the acidic medium. Thus, most of the QN was retained in the SBA-15 pore at pH 3.5 as evident from the HPLC chromatogram (data was not displayed). Contrarily, at pH 7.4, most of the QN was slowly released from the SBA-15 core. On the other hand, due to the enhanced electrostatic repulsion between the positively charged nanopore decorated in SBA-15 at pH 5.5, the maximum QN moiety was released in the medium, showing useful cytotoxic activity in cancer cells which was consistent with the earlier scientific reports. As QN displayed a dominant emission maximum at ~540 nm and two different excitation maxima, at ~380 nm, and ~440 nm, the enhanced green emission was observed under pH 5.5 with respect to the pH 7.4, confirming the maximum liberation in the medium (**Fig. 3A**) (21).

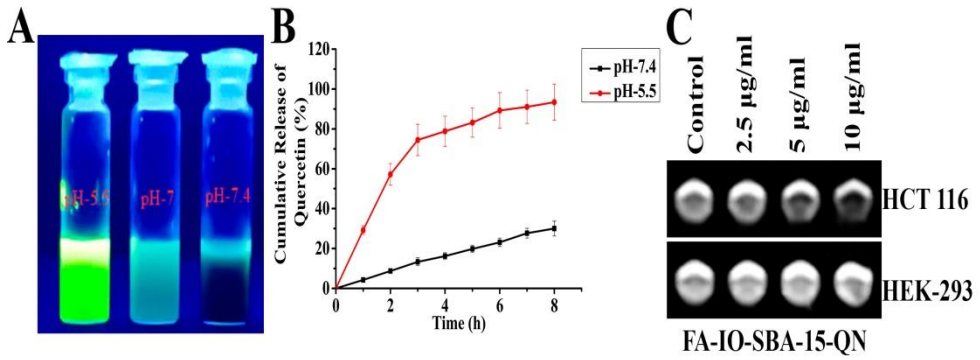

Fig 3: FL emission released by QN after the dispersion of FA-FE-SBA15QN in PBS at different pH values (5.5, 7 and 7.4). (B) Line diagram representing the release kinetics of QN from FA-FE-SBA15QN in different pH values (7.4 and 5.5). (C) In vitro T2 weight MRI images of HCT 116 and HEK-293 cells after the treatment of FA-FE-SBA15QN at different concentrations (2.5, 5, and 10 mg/ml). Values are represented as the mean SEM (n=5)

1.3.3. Illumination of *In vitro* contrasting property of FA-IO-SBA-15-QN:

The contrast effect of the FA-IO-SBA-15-QN was evaluated by measuring transverse (T_2) relaxation times of dispersed nanostructures under the MRI equipment (3.0 T). As evident in **Fig. 3C**, The T_2-weight MR signals were significantly augmented with the dose-dependent increase of FA-IO-SBA-15-QN in HCT 116 cells. Contrastingly, no MR signal was seenin HEK-293 cells when they were treated with FA-IO-SBA-15-QN. That suggested the pH-sensitivecontrasting property of nanomaterial. The specific Relaxivity value (r2) also measured in HCT 116 cells which weresignificantly enough (145.2 mM^{-1} s^{-1}) to serve as a unique and sensitive contrast agent for diagnostic purposes (22).

1.3.4. Comparative analysis between QN and FA-IO-SBA-15-QN induced cytotoxicity in HCT 116 cells:

To determine the cytotoxic activity of native QN as well as to compare it with the growth inhibitory potential of different components of orchestratedFA-IO-SBA-15-QN,

including Folic Acid (FA), Iron Oxide (Fe_3O_4), mesoporous silica nanoparticle (SBA-15), various concentration were assessed (3-30 µg/ml for QN, 10-100 µg/ml for Fe_3O_4, 5-30 µg/ml for SBA-15, 5-30 µg/ml for FA-SBA-15, and 5-30 for FA-IO-SBA-15-QN) in colorectal carcinoma cells (HCT 116), where 50% (IC_{50}), 70% (IC_{70}) growth inhibition were also evaluatedand displayed on the basis of cytotoxicity.

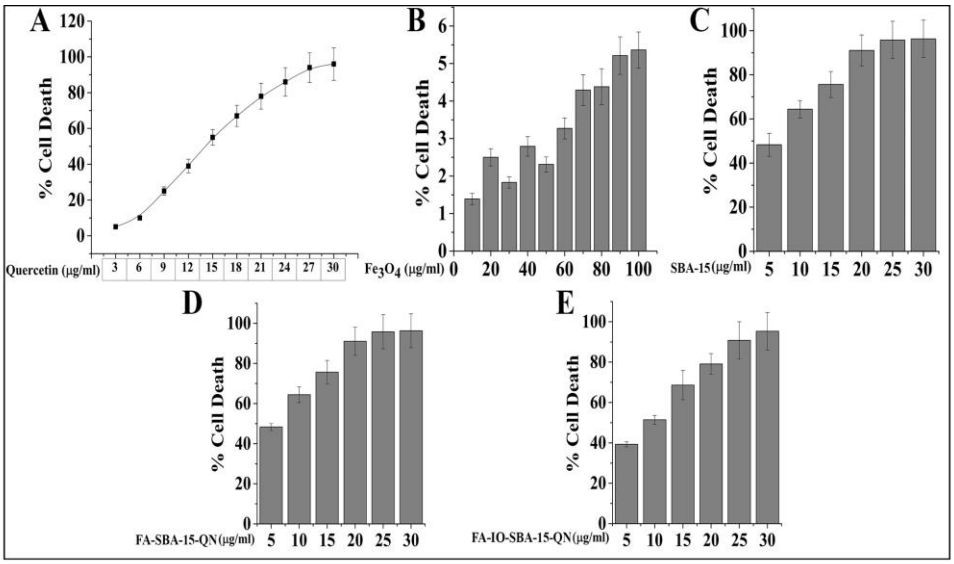

Fig. 4. Assessment of cell viability upon the treatment of different concentration of QN, Fe_3O_4, SBA-15, FA-SBA-15QN, and FA-IO-SBA-15-QN. Values are represented as mean ± SEM (n=5).

As depicted in **Fig. 4A**, a gradual increase in cytotoxicity was found upon the treatment of native QN at which IC_{50} was 15 µg/ml. The potential activity of QN to perturb the cell viability of different cancer cell has been previously well described. Therefore, presently this study was to design a nanomaterial that could extremize the QN activity along with its bioavailability at the target site. Earlier scientific studied well evidenced that loading of various chemotherapeutic drugs in nanomaterial has been conserved and sometimes potentiated the activity. On the other hand, Fe_3O_4 treatment alone did not show any promising cytotoxicity in higher concentration, indicating a little effect on cell viability (**Fig. 4B**). But contrastingly, SBA-15, FA-conjugated SBA-15, and fully orchestrated SBA-15 treatment showed a variable reduction in cell viability (**Fig. 4C, 4D and 4E**). More than 50% cell death depicted at ~ 14 µg/ml of SBA-15, and FA-SBA-15 application, whereas, IC_{50} was lowered (10 µg/ml) when cells were treated with FA-IO-SBA-15-QN, suggesting the

enhancement of cytotoxic activity which was accordance with the previous studies. Based on the initial experimentation, the effective concentration of 15 µg/ml of QN and 10 µg/ml of FA-IO-SBA-15-QN were chosen for the entire study for the exploration of the molecular mechanism of action (23-24).

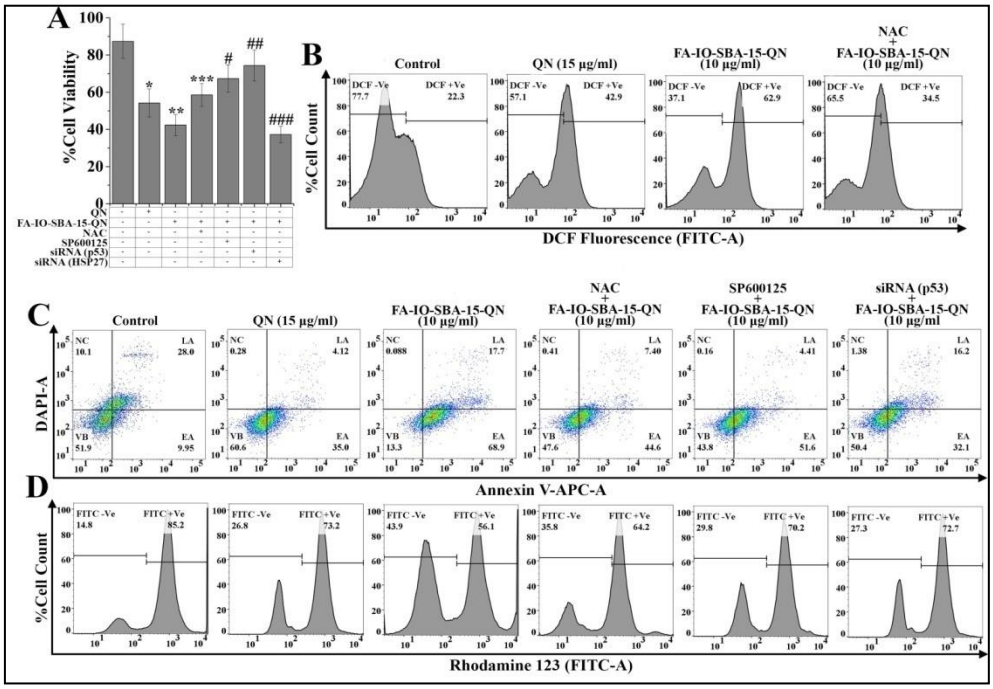

Fig. 5. Determination of cell viability, iROS, apoptosis/necrosis, and mitochondrial membrane potential upon the treatment of QN (15 µg/ml) and FA-IO-SBA-15-QN (10 µg/ml) along with/without of NAC, SP600125, p53 siRNA, and HSP27 siRNA application in HCT 116 cells. (A) Bar graph showing cell viability, Representative flow cytometric dot plot and gating hierarchy used to define (B) DCF +Ve cells and DCF -Ve cells, (B) viable cells (VB), early apoptotic cells (EA), late apoptotic cells (LA), and necrotic cells (NC), (C) High ΔΨ and Low ΔΨ, (D) FITC +Ve cells and FITC –Ve cells. Values are represented as mean ± SEM (n=5). p<0.05 was considered as significant. Statistical comparison: *Control vs. QN (15 µg/ml); **Control vs. FA-IO-SBA-15-QN (10 µg/ml); ***FA-IO-SBA-15-QN (10 µg/ml) vs. FA-IO-SBA-15-QN (10 µg/ml) + NAC; #FA-IO-SBA-15-QN (10 µg/ml) vs. FA-IO-SBA-15-QN (10 µg/ml) + SP600125; ##FA-IO-SBA-15-QN (10 µg/ml) vs. FA-IO-SBA-15-QN (10 µg/ml) + siRNA (p53); ###FA-IO-SBA-15-QN (10 µg/ml) vs. FA-IO-SBA-15-QN (10 µg/ml) + siRNA (HSP27).

1.3.5. Analysis of alteration in intercellular reactive oxygen species in HCT116 cells after FA-IO-SBA-15-QN treatment:

A growing body of evidencesuggested QN triggers cytotoxicity in various cancer cells through the generation of iROS. To evaluate the role of FA-IO-SBA-15-QN in triggering iROS, flow cytometric evaluation was carried out using ROS-sensitive dye, H_2DCFDA.

Upon the action of iROS, the acetate group of H_2DCFDA is removed through the activity of intercellular esterase, following the conversion of non-fluorescent H_2DCFDA to highly fluorescent 2',7'-dichlorofluorescein (DCF). Hence, an significanthike in DCF fluorescence shows the relative amount of ROS generated within the cells. Result pointed out an enhanced DCF fluorescence (62.9%) upon the treatment of FA-IO-SBA-15-QN (10 μg/ml) which was much higher than the resultant DCF fluorescence of control (22.3%) and QN-treated state (42.9%) (**Fig. 5B**), suggesting a possibility of higher release of native QN in HCT-116 cells which mediated cytotoxicity. Contrastingly, a specific ROS scavenger, N-acetyl cysteine (NAC) significantly suppressed the ROS (34.5%) when treated along with FA-IO-SBA-15-QN, indicating the direct correlation of ROS-mediated cytotoxicity in HCT-116 cells. The following result corroborated with the earlier demonstrated literature (25).

1.3.6. Analysis of FA-IO-SBA-15-QN-mediated apoptosis and necrosis in HCT-116 cells:

To examine the apoptosis and necrosis upon the FA-IO-SBA-15-QN treatment, a detailed flow cytometric evaluation was performed by using Annexin V/DAPI. Annexin V is a commonly used marker to detect apoptotic cells by its ability to bind phosphatidylserine of the outer leaflet of the cellular membrane. **Fig. 5C** demonstrated that the percent cell population of early (EA) and late (LA) apoptosis was markedly enhanced with the treatment of FA-IO-SBA-15-QN (68.9% of EA and 17.7% of LA) which was much higher than native QN treatment (35.0% of EA and 4.12% of LA) with respect to the control cells (9.95% of EA and 28.0% of LA). Comprising, treatment of NAC along with FA-IO-SBA-15-QN, the augmented level of EA (44.6%) and LA (7.40%) population was reduced. Whereas, silencing of p53 (p53 siRNA) markedly reduced EA (32.1%) and LA (16.2%) in FA-IO-SBA-15-QN-treated condition which was much higher than with the co-application of JNK inhibitor (SP600125) (51.6% of EA and 4.41% of LA) and FA-IO-SBA-15-QN (10 μg/ml). The above

result indicated the involvement of JNK and p53-regulated apoptosis in FA-IO-SBA-15-QN-mediated cytotoxicity which was in accordance with the earlier reports (26).

1.3.7. Estimation of mitochondrial membrane potential change (ΔΨm) in HCT-116 cells after FA-IO-SBA-15-QN treatment:

Various previous reports well documented that mitochondrial dysfunction has been associated with the apoptosis phenomenon and also involved in the regulation of crucial signaling mediators in triggering apoptosis. To establish underlying fact the involvement of ΔΨm in FA-IO-SBA-15-QN-mediated apoptosis, a tracer dye Rhodamine 123 (RH-123) was used through flow cytometry application. The rate of mitochondrial energization mediates the quenching of RH-123 which reflects a progressive reduction with the change in ΔΨm. Thus, the resultant fluorescence decay of RH-123 is corelated to the mitochondrial membrane potential. As illustrated in **Fig. 5D**, the relative RH-123 +Ve cells (FITC +Ve) were decreased (73.2% and 56.1%) after treatment of QN (15 µg/ml) and FA-IO-SBA-15-QN (10 µg/ml). Surprisingly, co-treatment of NAC, SP600125, and siRNA specific for p53 with FA-IO-SBA-15-QN, the percent RH-123 +Ve cells were gradually increased (64.2%, 70.2%, and 72.7%) with respect to the FA-IO-SBA-15-QN-treated alone group, representing the possible correlation between mitochondrial-dependent apoptosis and JNK/ p53-mediated downstream signaling system (27).

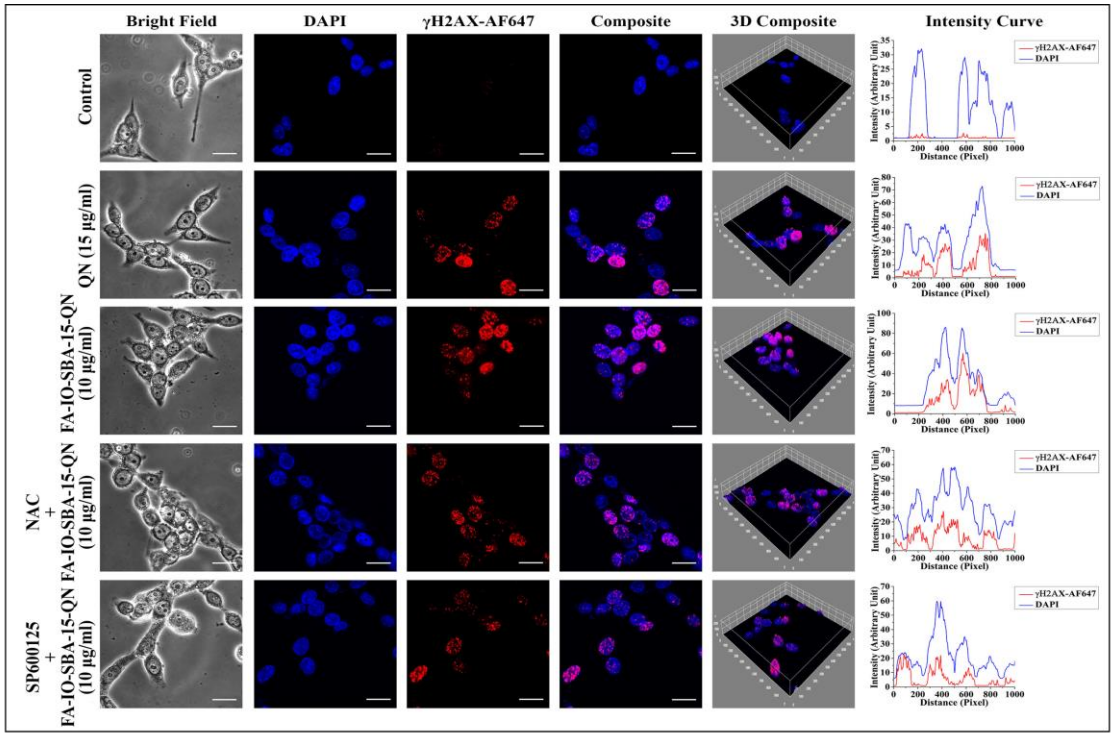

Fig. 6. QN and FA-IO-SBA-15-QN-induced DSBs were marked by γH2AX foci. Immunofluorescence images showing the expression of γH2AX. DAPI was used for nuclear staining. Slides were viewed using a Confocal microscope (Magnification 20×). Respective fluorescence intensities (γH2AX-AF647 and DAPI) were analyzed using ImageJ software through RGB calculator.

1.3.8. FA-IO-SBA-15-QN induced phosphorylation H2AX in HCT-116 cells:

A direct co relation between DNA damage and apoptosis exists as supported by a large body of literature. DNA damage, a common event of life, is responsible for triggering apoptosis by controlling numerous signaling systems. H2AX, a prime member of H2A protein family, is a component of histone octamer of nucleosomes. Upon DNA damage (DSB) by exogenous and endogenous sources, the H2AX is phosphorylated at Ser139 to form gamma-H2AX (γ-H2AX), which recruits repair proteins at the damaged site of DNA. Previous reports also well evidently established that γ-H2AX formation is an indicative step for DNA damage that provokes the activation of downstream machinery-associated with apoptosis. To elucidate the role of FA-IO-SBA-15-QN in triggering DNA breakdown resulting the apoptosis machinery, H2AX phosphorylation was studied through

immunofluorescence. As portrayed in **Fig. 6**, the number of γH2AX foci formation was increased with the treatment of native QN. On the contrary, the foci formation in HCT 116 was markedly increased when treated with FA-IO-SBA-15-QN, indicating the enhancement of DNA damage. However, NAC co-treatment with FA-IO-SBA-15-QN, the enhancement of DNA damage was slower, representing a putative effect of ROS on the γH2AX formation. Whereas, SP600125, a known JNK inhibitor, also suppressed H2AX formation over FA-IO-SBA-15-QN treatment, suggesting that JNK inhibition may attenuate H2AX phosphorylation, which was corroborated with the previous report (28-29).

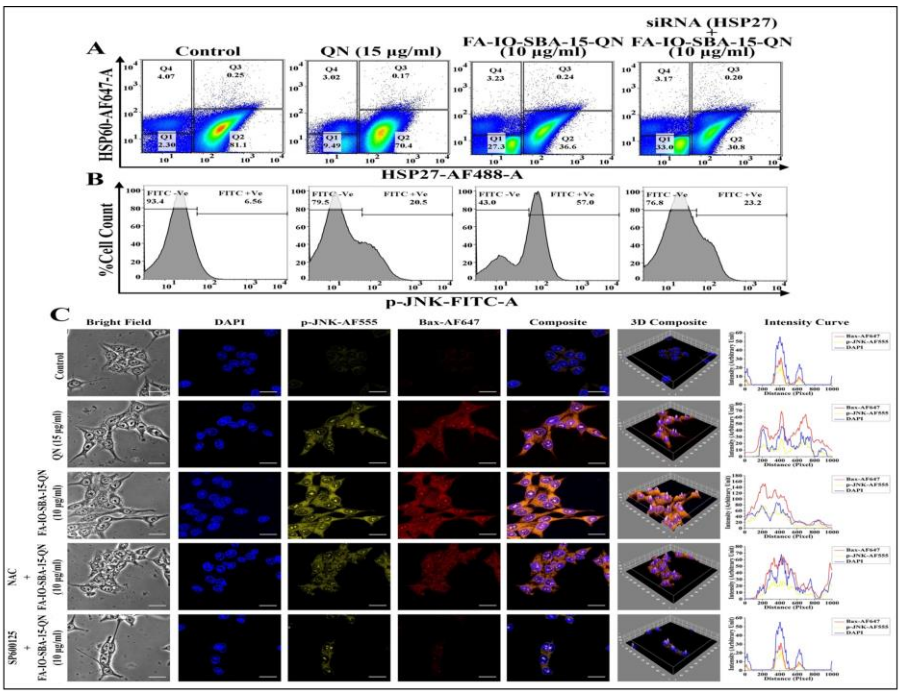

Fig. 7. QN and FA-IO-SBA-15-QN-induced modulation of HSP60, HSP27, p-JNK, and Bax expression in HCT 116 cells with/without application of NAC, SP600125, and siRNA (HSP27). Representative flow cytometric dot plot and gating hierarchy used to define (A) Q1: HSP60-AF647 -Ve/HSP27-AF488 -Ve cells; Q2: HSP60-AF647 -Ve/HSP27-AF488 +Ve cells; Q3: HSP60-AF647 +Ve/HSP27-AF488 +Ve cells; Q4: HSP60-AF647 +Ve/HSP27-AF488 -Ve cells, (B) p-JNK-FITC -Ve and p-JNK-FITC +Ve cells. (C) Immunofluorescence images showing the expression of p-JNK and Bax. DAPI was used for nuclear staining. Slides were viewed using a Confocal microscope (Magnification 20×). Respective fluorescence intensities (p-JNK-AF555, Bax-AF647, and DAPI) were analyzed using ImageJ software through RGB calculator.

1.3.9. Modulation of HSPs in HCT-116 cells after FA-IO-SBA-15-QN induction:

Heat shock protein (HSP), a conserved superfamily of protein, functions as a molecular chaperone to guard protein against illicit or promiscuous interaction between other proteins. Activation of HSPs has been shown to increase resistance against programmed cell death induced by multifaceted factors. Various studies manifested that HSP27, a subfamily of HSPs, is associated with the regulation of apoptosis through the inhibition of multiple signaling systems. Bicolor flow cytometric analysis exhibited that FA-IO-SBA-15-QN markedly reduced (36.6%) HSP27 expression (HSP-AF488 +Ve cells) as compared to the QN-treated cells (70.4%). On the other hand siRNA specific for HSP27 treatment along with FA-IO-SBA-15-QN, a further decrease in HSP27 expression (30.8%) was observed (**Fig. 7A**). The expression of another HSP, precisely HSP60 (HSP60-AF647 +Ve cells), was unchanged throughout the following treatment of QN and FA-IO-SBA-15-QN, suggesting that only HSP27 was attenuated with the application of QN and FA-IO-SBA-15-QN. Diminished cell viability (37.28%) was also detected on the use of HSP27 siRNA with FA-IO-SBA-15-QN treatment which was much nominal as compared to the FA-IO-SBA-15-QN treatment (42.38%) (**Fig. 7A**), supporting the fact that HSP27 inhibition was directly correlated with the cytotoxicity (30).

1.3.10. Analysis of phosphorylation of JNK in HCT-116 cells after FA-IO-SBA-15-QN treatment:

One of the most emminantmitogen-activated protein kinase family of proteins, Jun N-terminal kinase (JNK) play a pivotal role in mitochondrial-assisted apoptotic pathways. Studies have also evidenced that JNK isan indispensable playerin both mechanism cell proliferation and apoptosis. A corelating mechanism exists between JNK and HSP27. Mechanical attenuation of HSP27 stifles JNK activation which also modulated apoptosis-associated protein expression. As observed in our immunofluorescence analysis, JNK was

significantly phosphorylated when treated with FA-IO-SBA-15-QN. The augmented expression was markedly decreased after SP600125 treatment which was much lower than NAC treatment (**Fig. 7C**). Concomitant treatment with SP600125 and FA-IO-SBA-15-QN also elevated the cell viability (67.34%) when compared with the FA-IO-SBA-15-QN (42.38%), indicating that the loss of JNK function could inhibit the apoptosis (**Fig. 7A**). Contrarily, treatment with siRNA specific for HSP27 also reduced JNK phosphorylation (JNK-FITC +Ve of 23.2%) in FA-IO-SBA-15-QN-treated condition which supports the fact that HSP27 may modulate the JNK expression (**Fig. 7B**) (31).

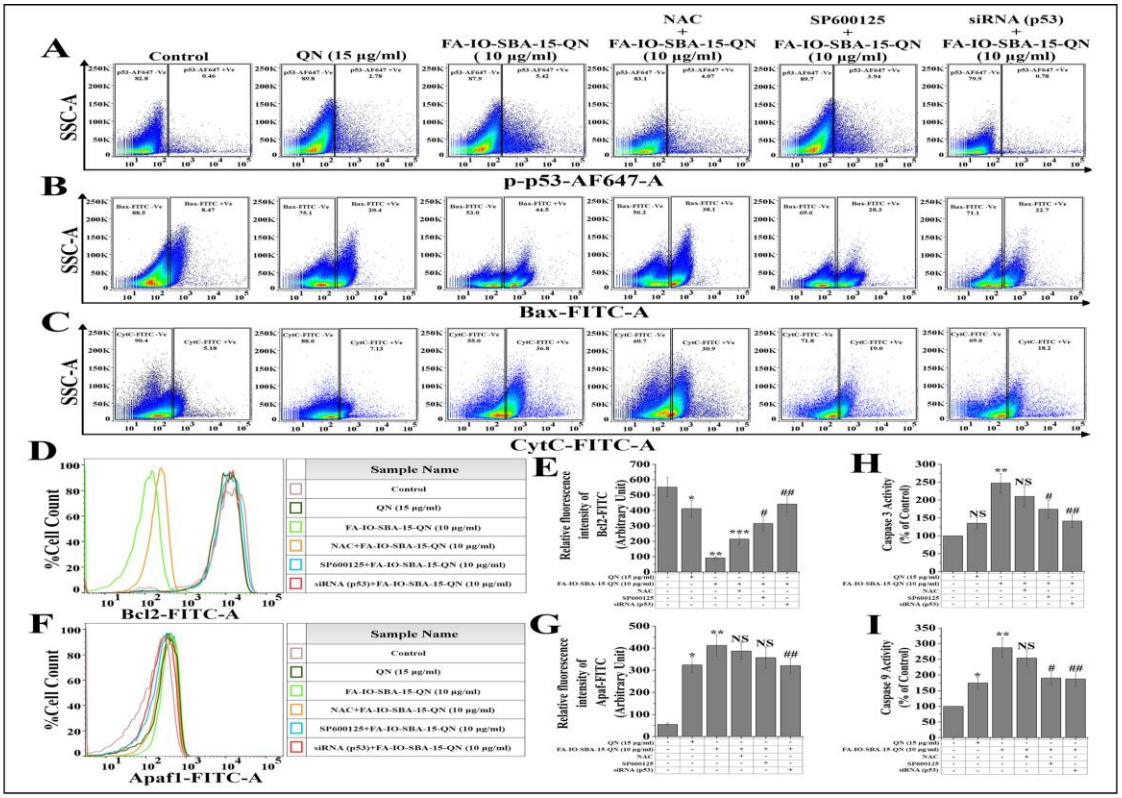

Fig.8.Assessment of mitochondrial-dependant apoptosis upon QN and FA-IO-SBA-15-QN treatment along with/without application of NAC, SP600125, and siRNA (p53). Representative flow cytometric dot plot and gating hierarchy used to define (A) p53-AF647 +Ve and p53-AF647 -Ve cells, (B) Bax-FITC +Ve and Bax-FITC –Ve cells, (C) CytC-FITC +Ve and CytC-FITC –Ve cells. Representative flow cytometric histogram showing (D) Bcl2 and (F) Apaf1. Bar graph showing relative fluorescence intensities of (E) Bcl2-FITC and (G) Apaf1-FITC. Bar graph showing (H) Caspase 3 and (I) 9 activity in the different experimental condition in HCT-116 cells Values are represented as mean ± SEM (n=6). p<0.05 was considered as significant. Statistical comparison: *Control vs. QN (15 µg/ml); **Control vs. FA-IO-SBA-15-QN (10 µg/ml); ***FA-IO-SBA-15-QN (10 µg/ml) vs. FA-IO-SBA-15-QN (10 µg/ml) + NAC; #FA-IO-SBA-15-QN (10 µg/ml) vs. FA-IO-SBA-15-QN (10 µg/ml) + SP600125; ##FA-IO-SBA-15-QN (10 µg/ml) vs. FA-IO-SBA-15-QN (10 µg/ml) + siRNA (p53); NS=Non significant.

1.3.11. FA-IO-SBA-15-QN trigger of p53-guided mitochondrial apoptosis:

A master redox-assisted transcription factor, p53 (tumor suppressor protein) is turned on in the regulation of mitochondrial-dependent apoptosis by responding DNA damage.

Enhanced phosphorylation of p53 targets the proapoptotic members of Bcl2 family proteins including, Bax, PUMA, and NOXA by its ability to control transcription. Besides, p53 can also transactivate several components of apoptotic effector machinery. One of these components, Apaf1 plays as a coactivator of caspase 9, which helps to initiate caspase cascade. FA-IO-SBA-15-QN treatment markedly enhanced the p53 phosphorylation (5.42%) over the control group (**Fig. 8A**) (0.46%) which also increased the expression of proapoptotic protein Bax (44.5%) (**Fig. 8B**). On the other hand, an anti-apoptotic protein, Bcl2 (0.17-fold) was also decreased upon the FA-IO-SBA-15-QN treatment (**Fig. 8D and 8E**). The expression of Cytochrome c (36.8%) and Apaf-1 (7.47-fold) was augmented (**Fig. 8C, 8F and 8G**) with the FA-IO-SBA-15-QN treatment which further supported the final fate of apoptosis as observed in the activation of caspase cascade (2.87-fold for caspase 9 and 2.47-fold for caspase 3) (**Fig. 8H and 8I**). Selective inhibition of p53 using specific siRNA remarkably diminished the p53 phosphorylation (0.78%), following the enhancement of Bcl2 (0.80-fold) as well as suppression of Bax (22.7%), CytC (18.2%), and Apaf1 (5.82-fold) that was more pronounced than NAC (4.07% for p-p53, 38.1% for Bax, 30.9% for CytC, 7.01-fold for Apaf-1, 0.39-fold for Bcl2, 2.54-fold for caspase 9, and 2.10-fold for caspase 3)/SP600125 (3.94% for p-p53, 28.3% for Bax, 19.0% for CytC, 6.47-fold for Apaf-1, 0.57-fold for Bcl2, 1.90-fold for caspase 9, and 1.74-fold for caspase 3) treatment. Surprisingly, p53 inhibition using siRNA also decreased the caspase activation (1.87-fold for caspase 9 and 1.41-fold for caspase 3) which increased cell viability (74.35%) (**Fig. 8A**), indicating the presence of possible crosstalk mechanism between p53 phosphorylation and mitochondrial apoptosis in FA-IO-SBA-15-QN treated state (32).

1.3.12. FA-IO-SBA-15-QN trigger mitochondrial guided apoptosis through activating JNK/p53 axis:

For further confirmation of the JNK-induced activation of apoptosis in FA-IO-SBA-15-QN-treated condition, immunofluorescence assay was carried out. FA-IO-SBA-15-QN-treatment augmented Bax expression which was greater than naive QN treatment. On the contrary, selective inhibition of JNK pathway using SP600125 further diminished the Bax expression. Surprisingly NAC treatment along with FA-IO-SBA-15-QN did not affect significantly on JNK and Bax expression. These data depicted that the JNK pathway might regulate p53-guided Bax expression (**Fig. 8C**).

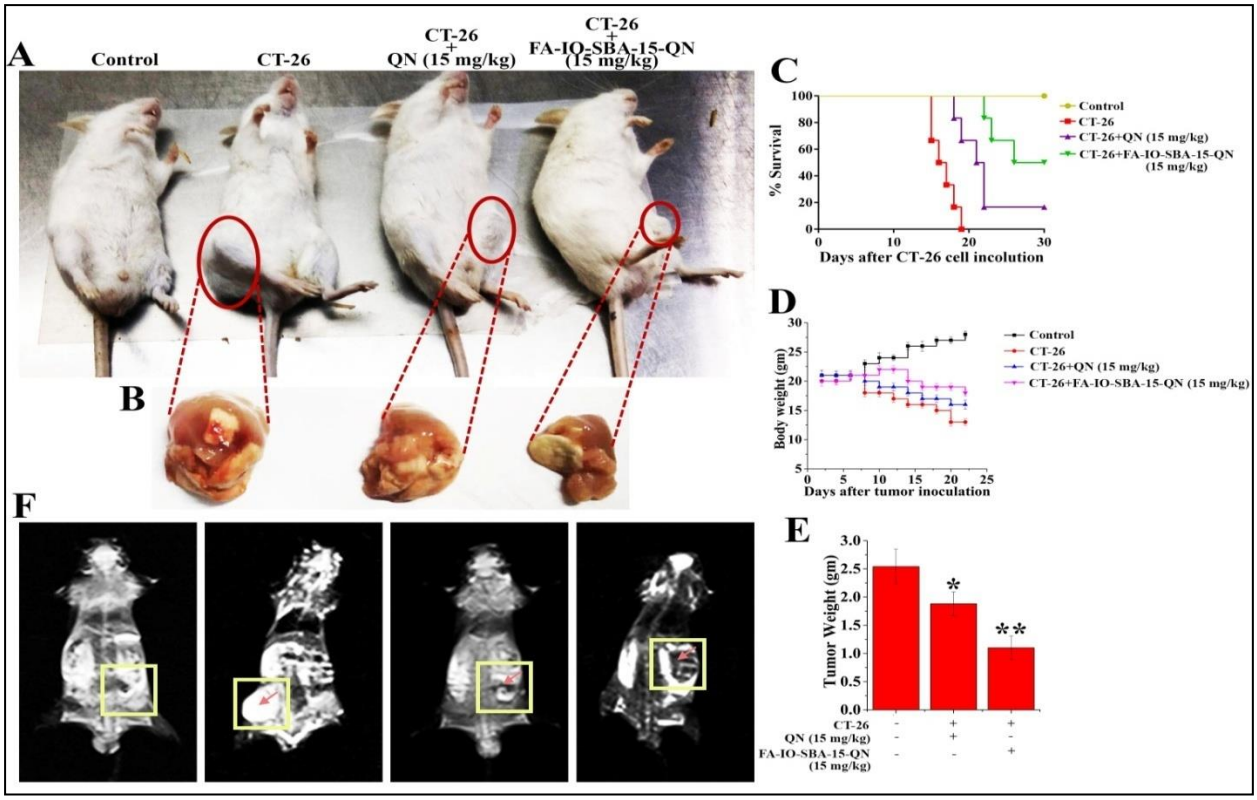

Fig. 9: In vivo assessment of chemotheranostic potential of QN and FA-IO-SBA-15-QN. (A) Experimental animals showing tumor growth inhibitory activity of QN and FA-IO-SBA-15-QN, (B) Representative images of tumor harvested after the completion of experimentation. (C) Kaplan-Meier analysis of 30 days survival of CT-26 tumor-bearing mice post-administrated with QN and FA-IO-SBA-15-QN (15 mg/kg). (D) Representative line diagram showing body weight change throughout the experimental period, (E) Bar graph showing tumor weight. (F) In vivo T_2 weight MRI images of CT-26 tumor-bearing mice. Rectangular zone indicating the tumor area. Values are represented as mean ± SEM (n=5). p<0.05 was considered as significant. Statistical comparison: *CT-26 vs. CT-26+QN (15 mg/kg); **CT-26 vs. CT-26+FA-IO-SBA-15-QN (15 mg/kg).

1.3.13. Experimentally analysis of restoration in survivability rate of tumor-induced mice after FA-IO-SBA-15-QN administration:

To evaluate whether FA-IO-SBA-15-QN had substantial antiproliferative activity over native QN, a suitable tumor-bearing murine model was developed through subcutaneous injection of CT-26 cells (**Fig. 9A**). The optimum effectivity of FA-IO-SBA-15-QN and QNwas also determined on the basis of survivability. Data corresponding to the optimum effective dosage of FA-IO-SBA-15-QNand QNon the survival rate of mice estimated after the CT-26 challenge is illustrated in **Fig. 9C**. FA-IO-SBA-15-QNapplication alone for six alternate days did not induce any death within the 30-day observational period. The first death of CT-26 tumor-bearing mice was observed after the 15^{th} day of CT-26 challenge due to the significant symptoms including reduction of food/water intake, irritability, enhanced tumor burden, weight loss, lethargy, and roughing of hair. Results also demonstrated that 50% of animals died within the 16 days of CT-26 challenge and 100% mortality was reachedat 19^{th} day. Administration of FA-IO-SBA-15-QN(15 mg/kg) on CT-26 tumor-bearing condition enhanced the survival proportion with respect to the CT-26 challenge alone. The maximum survival (50%) was evident with the treatment of 15 mg/kg of body weight of FA-IO-SBA-15-QN,while 16.67% of animals died within the 30-day observational period upon the treatment of native QN (15 mg/kg), validating the effectivity of FA-IO-SBA-15-QN over native QN (33).

1.3.14. Estimation of weight loss in tumor induced mice after FA-IO-SBA-15-QN treatment:

A remarkable loss of body weight has been profoundly associated with the development of tumor mass due to the failure of homeostatic balance. To examine whether FA-IO-SBA-15-QNtreatment was effective in reducing the cancer-induced complications, a regular assessment of body weight was monitoreduntil the end of experimentation. A marked

reduction of body weight was evident after the introduction of CT-26 cells. The average body weight was reduced to 24% on the 15th day of experimentation. Interestingly, FA-IO-SBA-15-QN treatment (15 mg/kg) markedly restored the tumor-induced body weight reduction (5%) over QN (15%), indicating that FA-IO-SBA-15-QN administration was helped to maintain the body weight in tumor-bearing mice **(Fig. 9D)** (34).

1.3.15. Evaluation of reduction in tumor weight after FA-IO-SBA-15-QN treatment:

A remarkabledecrease in tumor weight was measured after 15mg/kg FA-IO-SBA-15-QNadministration as compared with native QN (15 mg/kg). The depletionof tumor weight was significantly reduced to 1.11 and 1.88 gm as compared to the untreated tumor mass (2.54 gm) **(Fig. 9B and 9E)**.

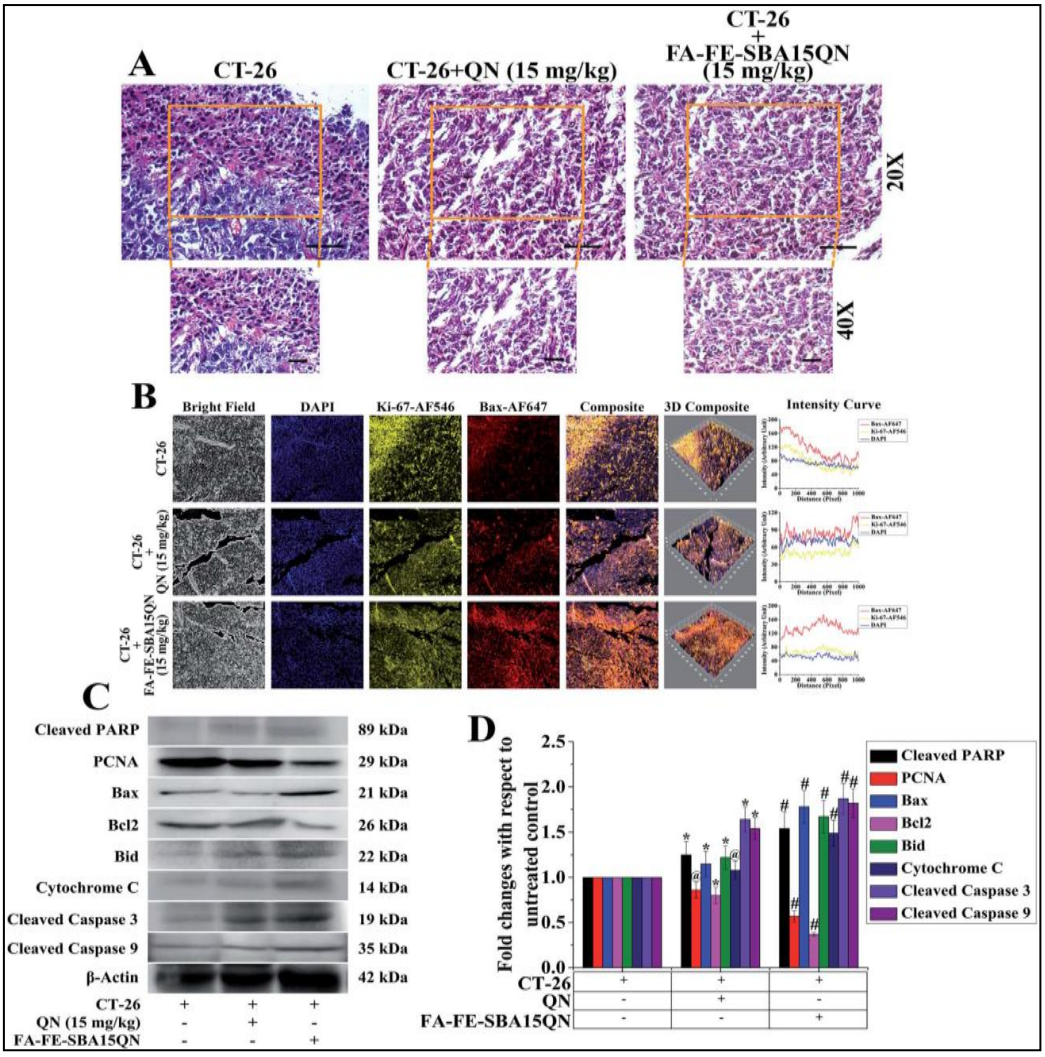

Fig. 10. (A) Histopathological assessment of tumor microenvironment. The tumor tissue architectural assessment was done using hematoxylin & eosin staining (H&E) (Magnification: 20× and 40×). (B) Immunofluorescence images showing the expression of Ki-67 and Bax. DAPI was used for nuclear staining. Slides were viewed using a confocal microscope (Magnification 20×). Respective fluorescence intensities (Ki-67-AF546, Bax-AF647, and DAPI) were analyzed using ImageJ software through RGB calculator. (C) Representative immunoblots of cleaved PARP, PCNA, BAX, Bcl2, Bid, Cytochrome C, cleaved Caspase 3 and cleaved Caspase 9. (D) Densitometric analysis of relative protein expression of cleaved PARP, PCNA, BAX, Bcl2, Bid, Cytochrome C, cleaved Caspase 3 and cleaved Caspase 9. β-Actin was served as internal control. Values are presented as mean ± SEM (n=6). $p<0.05$ was considered as significant. Statistical comparison: *CT-26 vs. CT-26+QN (15 mg/kg); #CT-26 vs. CT-26+FA-IO-SBA-15-QN (15 mg/kg); @=Non significant.

1.3.16. Estimation of rate of CT-26 tumor cell proliferation after FA-IO-SBA-15-QN administration:

Ki-67, a cellular metastatic tumor marker protein associated with the cell proliferation. Ki-67 protein expression was determined in an experimental condition in order todetermine the ameliorative role of FA-IO-SBA-15-QNon the CT-26 tumor. Decreased Immunofluorescence level after15mg/kg FA-IO-SBA-15-QNrevealed that markedly reduced Ki-67 expression as well as increased Bax expression in the CT-26 tumor, suggesting a possible inhibition on tumor cell proliferation **(Fig. 10B)**. On the other hand, histopathological analysis of tumor mass also confirmed a similar result **(Fig. 10A)**. Tumor of untreated groups shows 70-90% viable polymorphic cells with dense and round nuclei. The tumor also showed an excessive microvascular compartment in an naive condition. Surprisingly, upon the treatment of FA-IO-SBA-15-QN(15 mg/kg), a marked reduction of microvascular compartment along with the viable tumor cells was observed which substantiated the previous reports. The data were also indicated that the efficacy of FA-IO-SBA-15-QN was more effective than native QN (15 mg/kg) treatment in reducing tumor cell proliferation as observed in the Ki-67 and Bax expression.

To further confirm the antiproliferative property of FA-IO-SBA-15-QN, plethora of protein expression-related to cellular proliferation and apoptosis were determined using immunoblot. As displayed in the **Fig. 10C and D**, the cellular proliferation marker, PCNA was significantly decreased with the treatment of FA-IO-SBA-15-QN which was more effective than native QN treatment (15 mg/kg). On the other hand, proapoptotic protein, Bax, Bid, cytochrome C, cleaved PARP was markedly augmented as well as a diminished expression of antiapoptotic protein, Bcl2 was evident upon the treatment of FA-IO-SBA-15-QN, suggesting the potent reductive ability of QN. The final fate of tumor reduction was observed when cleaved caspase 3 and 9 expression increased in the FA-IO-SBA-15-QN-treated condition, indicating the antiproliferative efficacy of FA-IO-SBA-15-QN over the QN-treated state.

1.3.17. Visualization of magnetic resonance imaging (MRI) of CT-26 adenocarcinoma by using novel contrast FA-IO-SBA-15-QN:

MRI, a widely used tool for diagnosis, is capable of providing detailed information on the structure-composition relationship of tumors, with spatial resolution. The use of exogenously administered contrasting agents allows compartment-specific enhancement of tumors, enabling image specific functional and interstitial volumes.One of the major goal of this study was to develop a particular molecular MR contrast agent which could probe and interact with ligand receptor-specific (FA) target molecule *and* also create a changes in local tissue proton relaxation times (longitudinal relaxation time, $T_{1;}$ and transverse relaxation time, T_2) to sense the tumour site.Folic acid receptor (FaR) is highly expressed in CT-26-induced adenocarcinoma. Hence, the approach was to target the folic acid receptor by folic acid-functionalized SBA-15. The unique capping material Fe_2O_3, having superparamagnetic property, used as a contrasting agent and the loaded QN was directed for its therapeutic efficacy. Thus, the contrasting feature of FA-IO-SBA-15-QN was determined to evaluate the targeted delivery of QN in the tumor site as well as to define its Theranostic approach. As evident in the *in vivo* MRI images, CT-26 bearing adenocarcinoma had no clear zone in terms of contrast area (T_2 relaxation time) at the tumor site. However, an enhanced T_2-MR signal (contrast area) was found at the tumor site when mice treated with FA-IO-SBA-15-QN, establishing its notable contrasting character which might be the promising approach for Theranostic drug development (**Fig. 9F**) (35-36).

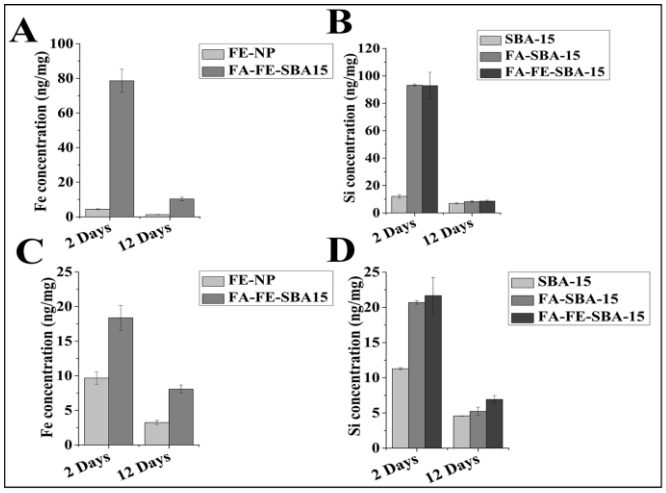

Fig. 11. The concentration of iron and silica content of IO-NP, SBA-15, FA-SBA-15, FA-IO-SBA-15 in (A and B) tumor tissue, (C and D) Hepatic tissue after the single application of respective nanoparticles in 2nd day and 12th day. Values are represented as mean ± SEM (n=6).

1.3.18. Evaluation of biodistribution of Fe and Si of SBA-15, FA-IO-SBA-15 in tumor and hepatic tissue:

Biodistribution of Si and Fe was found in hepatic and tumor tissue by ICP-MS. As depicted in the **Fig. 11**, a sprinkled quantity of naked IO-NP was found after the 1st treatment in liver and tumor which was almost negligible after 6th consecutive treatment. The rapid clearance of IO-NP was evident in all the tissues due to its Ultrasmall size. In case of FA-SBA-15, a maximum concentration of Si in liver and tumor tissue was found with respect to the SBA-15-treated group, which was also cleared after 6th consecutive treatment. Comparing with the all hepatic tissue, tumor had the maximum agglomeration of Si and Fe, justifying the targeted delivery of FA-IO-SBA-15.

1.4. Conclusion:

The formulation and characterization of Fe_3O_4-functionalized mesoporous silica SBA-15 loaded with QN (FA-IO-SBA-15-QN) is represented in this study. *In vitro* investigations on human colorectal carcinoma cells (HCT 116) evidenced a dose-dependent decrease of cell viability which was also in a direct relationship with the QN content in SBA-15. Surface

modification by Fe_3O_4 helped to act as a better contrasting agent which was useful for cancer/tumor detection under MRI. FA conjugation increased the QN delivery with more targeted and sophisticated waywhich would provide better clinical outcomes with less toxicity and offer a superior treatment modality in future chemotherapeutic approach. Further, FA-IO-SBA-15-QN triggered caspase-dependent apoptosis integrated with overexpression of p53, Bax, and CytC as well as down-regulation of Bcl-2. Additionally, FA-IO-SBA-15-QN inhibited HSP27 expression which could enhance the JNK expression, followed by the indirect phosphorylation of H2AX/DSBs. All of this demonstrated positive effects of SBA-15 as a drug carrier system with pronounced cytotoxic activity. SBA-15 amplified the activity of QN *in vitro* system and protected the active compound from impulsive, light-directed inactivation or degradation guided by extremely acidic conditions corresponding to gastric pH. Thus, FA-IO-SBA-15-QN can be successfully used in cancer therapy, with the vital ability to the delivery of chemotherapeutic drugs intracellularly.

1.5. References:

1.N. G. Zaorsky, T. M. Churilla, B. L. Egleston, S. G. Fisher,J. A. Ridge, E. M. Horwitz, J. E. Meyer, *Ann. Oncol.*,2017, 28, 400–407.

2. F. Bray, J. Ferlay, I. Soerjomataram, R. L. Siegel, L. A. Torre, A. Jemal, *Ca-Cancer J. Clin.*, 2018, 68, 394–424.

3 A. Urruticoechea, R. Alemany, J. Balart, A. Villanueva,F. Vinals, G. Capella, *Curr. Pharm. Des.*, 2010, 16, 3–10.

4 H. Zaid, M. Silbermann, A. Amash, D. Gincel, E. Abdel-Sattar,N. B. Sarikahya, *Evidence-Based Complementary and Alternative Medicine*, 2017, 7952417.

5 N. Bertranda, J. Wub, X. Y. Xua, N. Kamaly, O. C. Farokhzadb, *Adv. Drug Delivery Rev.*, 2014, 66, 2–25.

6.A. Sarkar, S. Ghosh, S. Chowdhury, B. Pandey, P. C. Sil, *Biochim. Biophys. Acta, Gen. Subj.*, 2016, 1860, 2065–2075.

7. M. L. Mansuri, P. Parihar, I. Solanki, M. S. Parihar, *GenesNutr.*, 2014, 9, 400.

8.Y. Li, J. Yao, C. Han, J. Yang, M. T. Chaudhry, S. Wang, H. Liu, Y. Yin, *Nutrients*, 2016, 8, 167.

9. A. Rauf, M. Imran, I. A. Khan, M. Ur-Rehman, S. A. Gilani,Z. Mehmood, M. S. Mubarak, *Phytother. Res*., 2018, 32,2109–2130.

10. T. Ramasamy, H. B. Ruttala, N. Chitrapriya, B. K. Poudal, J. Y. Choi, S. T. Kim, Y. S. Youn, S. K. Ku, H. G. Choi,C. S. Yong , J. O. Kim, *Acta Biomater*., 2017, 48, 131–143.

11. B. Liu, T. Jiang, H. Q. Zheng, S. Dissanayke, W. Q. Song,A. Federico, S. L. Suib , J. He, *Nanoscale*, 2017, 9, 6380–6390.

12. L. B. D. Freitas, I. J. G. Bravo, W. A. D. Macedo, E. M. B. de Sousa, J. Sol-Gel, *Sci. Technol.*, 2016, 77, 186–204.

13. K. Sarkar, K. Dhara, M. Nandi, P. Roy, A. Bhaumik , P. Banerjee, *Adv. Funct. Mater.*, 2009, 19, 223–234.

14. Q. Gao, W. S. Xie, Y. Wang, D. Wang, Z. H. Guo, F. Gao,L. Y. Zhao, Q. Cai, *RSC Adv.*, 2018, 8, 4321–4328.

15. B. Dragoi, I. Mazilu, A. Chirieac, C. Ciotonea, A. Ungureanu, E. Marceau, E. Dumitriu , S. Royer, *Catal. Sci. Technol.*,2017, 7, 5376–5385.

16.P. Bhanja, A. Modak, S. Chatterjee, A. Bhaumik, *ACS Sustainable Chem. Eng.*, 2017, 5, 2763–2773.

17. J. Pang, L. Zhao, L. Zhang, Z. Li , Y. Luan, *J. Colloid Interface Sci.*, 2013, 395, 31–39.

18. E. Li, Y. Yang, G. Hao, X. Yi, S. Zhang, Y. Pan, B. Xing ,M. Gao, *Nanotheranostics*, 2018, 2, 233–242.

19.P. Bhanja, S. Mishra, K. Manna, A. Mallick, K. Das Saha , A. Bhaumik, *ACS Appl. Mater. Interfaces*, 2017, 9, 31411–31423

20.W. Chen, C. A. Cheng, B. Y. Lee, D. L. Clemens, W. Y. Huang, M. A. Horwitz ,J. I. Zink, *ACS Appl. Mater. Interfaces*, 2018,10, 31870–31881.

21. M. S. Moorthy, J. H. Park, J. H. Bae, S. H. Kim,C. S. Ha, *J.Mater. Chem. B*, 2014, 2, 6487–6499.

22.H. Kalita, S. Rajput, B. N. P. Kumar, M. Mandal,A. Pathak, *RSC Adv.*, 2016, 6, 21285–21292.

23.M. X. Ren, X. H. Deng, F. Ai, G. Y. Yuan,H. Y. Song, *Exp.Ther. Med.*, 2015, 10, 579–583.

24. S. Y. Kim, H. C. Jeong, S. K. Hong, M. O. Lee, S. J. Cho,H. J. Cha, *Oncotarget*, 2017, 8, 64964–64973.

25. R. P. Rastogi, S. P. Singh, D. P. Haeder, R. P. Sinha, *Biochem. Biophys. Res. Commun.*, 2010, 397, 603–607.

26.S. R. Kumar, S. Priyatharshni, V. N. Babu, D. Mangalaraj,C. Viswanathan, S. Kannan, N. Ponpandian, *J. Colloid Interface Sci.*, 2014, 436, 234–242.

27. J. D. Ly, D. R. Grubb, A. J. A. Lawen, *Apoptosis*, 2003, 8,115–128.

28. J. Y. J. Wang, *Cell Death Differ.*, 2001, 8, 1047–1048.

29. A. Sharma, K. Singh and A. Almasan, *Methods Cell Biol.*,2012, 920, 613–626.

30. D. Lanneau, M. Brunet, E. Frisan, E. Solary, M. Fontenay,C. Garrido, *J. Cell. Mol. Med.*, 2008, 12, 743–761.

31. J. Ruan, Z. Qi, L. Shen, Y. Jiang, Y. Xu, L. Lan, L. Luo,Z. Yin, *Biochem. Biophys. Res. Commun.*, 2015, 456, 122–128.

32.J. S. Fridman ,S. W. Lowe, *Oncogene*, 2003, 22, 9030–9040.

33.A. Kim, M. Im, M. J. Gu , J. Y. Ma, Sci. Rep., 2016, 6, 24214.

34. A. Bonetto, J. E. Rupert, R. Barreto,T. A. Zimmers, *J.Visualized Exp.*, 2017, 117, 54893.

35.O. Fluge, K. Gravdal, E. Carlsen, B. Vonen, K. Kjellevold, S. Refsum, R. Lilleng, T. J. Eide, T. B. Halvorsen,K. M. Tveit, A. P. Otte, L. A. Akslen, O. Dahl,*G. Norwegian, Br. J. Cancer*, 2009, 101, 1282–1289.

36. D. A. Orringer, D. R. Vago , A. J. Golby, *Semin. Neurol.*,2012, 32, 466–475.

Chapter-2

A novel nanohybrid for cancer theranostics: folate sensitized Fe_2O_3 nanoparticles for colorectal cancer diagnosis and photodynamic therapy

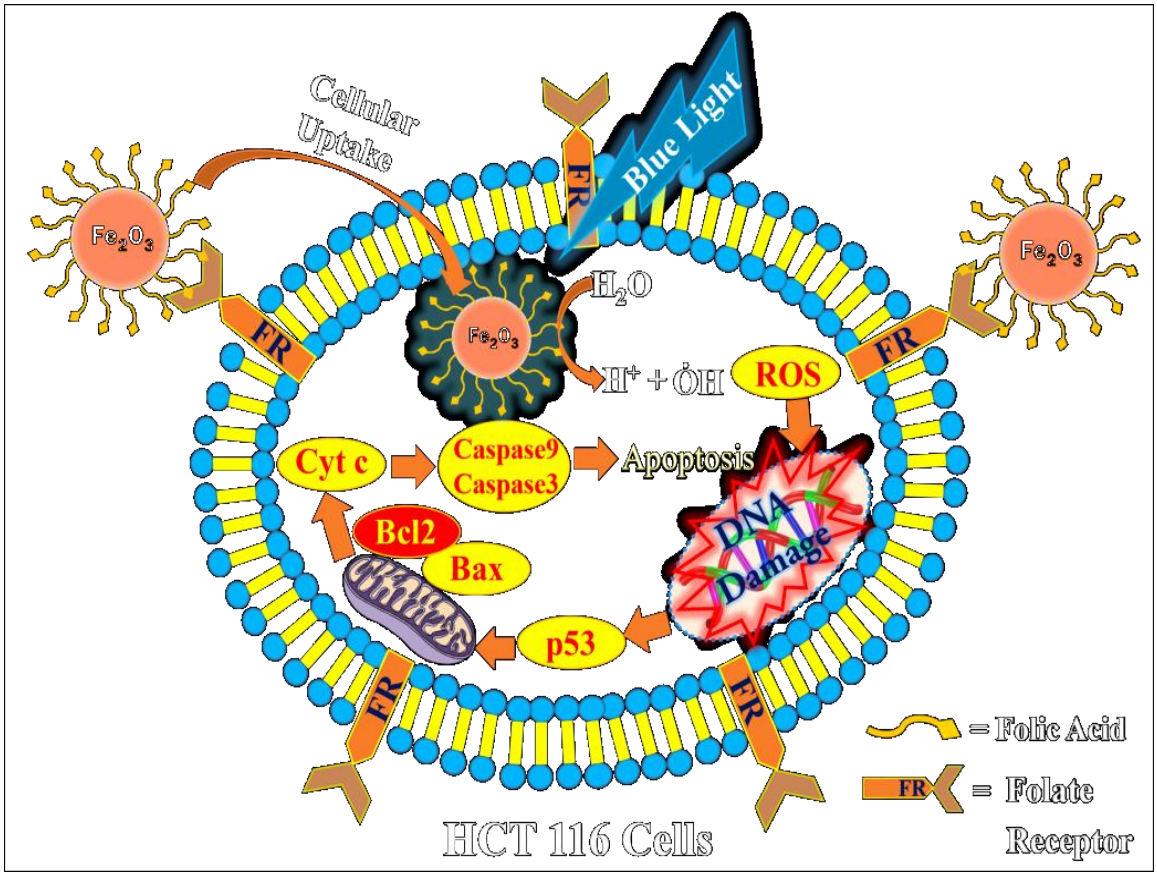

2.1. Introduction...

A great threat for every 21st century citizen is cancer. Everybody has a grave possibility to suffer in this malign malady (1). Due to its highly asymptomatic initial stages, prognosis is poor. That causes high rate of patient morbidity. When a mature stage valetudinarian is evincing his diagnosable symptoms, there is very least chance for physician or clinician to give him a bonafide remedy (2). That attract researcher to develop a sophisticated therapeutics, which not only effective as elegant medicine but also as a diagnostic tool. Effective surgical tumour removal and followed by chemo or radiation therapy is the orthodox medicament.But success rate is not at all satisfactorily after expensing high financial cost and physical malaise (2). Sometime associated disease due to cumulative medicinal side-effects were life threatening. In the year 1975, Dougherty was contraption/ designed a convincing solution for cancer with photodynamic theory (PDT) by using hematoporphyrin (3). As like every potential candidate, PDT have some challenges, but it successively overcome those limitations and validated as an elegant emerging therapy for cancer (4-7). Drug exposure followed by photo- irradiation withappropriate wavelength on the affected tissue, orchestrated drug excitation that provoke cell death by generating reactive oxygen species (ROS) and it is acomplete noninvasive process withevidently targeted tissue specific selectivity (8). This advance characteristic of specific delivery of a drug with PDT increases its therapeutic efficacy and reduced collateral effects significantly.

Folic acid (FA) is a highly specific, stable ligand express abundantly in malignant tumor (9). Its main binding specific target is folate receptor (FR), which is dominantly expressed in cancer cell and locatedat surface of cell membrane. Designing therapeutics strategies by targeting FR is very remedially effective because it is widely expressed in variety of cancer cells like, breast, kidney, colon, ovaries, cervix and renal cell carcinoma (10-12). FA conjugated like Au nanoparticles (NPs), quantum dot and doped semiconductor portrayed best affinity to FR expressing cells *i.e.* cancer cells. By using this phenomenon various nanoparticles were used not only to visualize cancer cells for diagnosis but also in treatments (13-15). Functionalized magnetic NPs are novel material for their high colloidal stability, target specificity. Thus NPs bound with FA is suitable for exclusive biomedical implementations such as magnetic resonance imaging (MRI) and magnetic hyperthermia. MRI contrast (accepted in FDA list) agents are gadolinium (Gd) based complexes, which is

causative toxicant for nephrogenic systemic fibrosis (NSF), a systematic disorder (16-18). There for, it is also a novel challenge to fabricate a nontoxic MRI contrast agent for the inventors. It is a good therapeutic prognosis to use a single nanoparticle with cumulative impact on diagnosis and remedy. Presently, these theranostics medicines were given highest attention not only by pharmacologists and medicine researcher but also by pharma industries for cost effective novel remedies with least side-effects.Nanomedicine with anticancer activity, that targeting specifically to cancer cells and magnetic property which can be used as diagnosis tool can be used as better therapeutics against cancer (19-20). Several approaches have been employed to synthesis folic acid functionalized iron oxide NPs for biomedical application using different organic linkers such as N-Hydroxysuccinimide (NHS), 1-Ethyl-3-(3-dimethylaminopropyl)-carbodiimide(EDC), 2,3-dibromopropionyl chloride (DBPC), polylactic-coglycolic acid and polyethylene glycol based attachment via multi-step complicated method of synthesis, which is a big issue to scale up the synthesis (21-22). To prepare a simple one step synthesis of FA templated iron oxide nano-medicine, may be a solution for theranostics application.

This ongoing study is about to designing a simple one-step hydrothermal synthesis of folic acid templated water soluble magnetic iron oxide NPs (FA-Fe_2O_3). FESEM, TEM and XRD imaging was carried out to visualize and characterize structural and morphological phenomenon. Minutely elaborate spectroscopic examination was performed with the help of FTIR, UV-Vis, fluorescence, Raman and time resolved fluorescence spectroscopy (TCSPC). Picosecond resolved Förster resonance energy transfer (FRET) was used to conformational evaluation on attachment of FA to Fe_2O_3 at molecular level. Photo induced enhanced ROS generation of FA-Fe_2O_3 with respect to Fe_2O_3 was monitored by dichlorofluorescin (DCFH) oxidation. Magnetic property was estimated by using VSM study. Anti-cancer activity and cellular uptake study have been performed on human colorectal carcinoma (HCT 116) cell line. We have carried out relaxometry study and MRI study of synthesized FA-Fe_2O_3 to consider its potential use as a MRI contrast agent for diagnosis. Upon relying on above mentioned assessments, ours NP may be a potential remedy for cancer patients.

2.2. Reagents and Methods: Synthesis…

2.2.1. Reagents:

Folic acid, Anhydrous $FeCl_3$, sodium hydroxide (NaOH), dichlorofluorescindiacetate (DCFH-DA), and Sodium dihydrogen phosphate (NaH_2PO_4)) were purchased from Sigma Aldrich. ethylene glycol and Ethanol were acquired from Merck. All utilized chemicals in this present research were of analytical grade and used as received without any further purification. HCT-116 (Human colorectal carcinoma) and HEK 293 (Human embryonic kidney) cell lines were obtained from NCCS, Pune, India. Chemicals requisite for cell culture like Dulbecco's Modified Eagle Medium (DMEM), Penicillin/streptomycin/neomycin (PSN) antibiotic, fetal bovine serum (FBS), trypsin and ethylenediaminetetraacetic acid (EDTA) etc.were obtained from Gibco-Life Technologies (Grand Island, NY, USA). Plastic wares (Tissue culture grade) were purchased from NUNC (Roskidle, Denmark) from Fermentas, EU. 3-(4,5- dimethylthiazol-2-yl)-2,5-diphenyltetrazolium bromide (MTT), DAPI (4',6-diamidino-2-phenylindole dihydrochloride), Acridine orange and Ethidium bromide were procured from SRL, (India), Invitrogen (California), Sigma-Aldrich (U.S), respectively. All antibodies were simultaneously bought from Santa Cruz Biotechnology, Inc. USA and eBioscience, Inc. San Diego, USA. Milli-Q water by Millipore was used as an aqueous solvent. Unless and until mentioned, all other used chemicals were purchased from Sigma-Aldrich Co. (St. Louis, MO, USA).

2.2.2. Fe_2O_3 synthesis:

Following protocol was generated and standardize in our laboratory for synthesis procedure. Anhydrous $FeCl_3$ (203 mg) was liquefied with 5 ml ethylene glycol and the solution was stirred for 30 min. After that, drop wise15 ml NaOH (0.25 M) solution was added with the help of constant stirring procedure. A brown color precipitate was obtained the resultant mixture then transferred into a Teflon-lined stainless-steel autoclave. The sealed autoclave was then placed at 150˚C for 18 hr without stirring. The system was allowed to cool down, after respective reaction was completed, to ambient temperature naturally. The product was isolated via centrifugation, then washed three times with Milli Q water and ethanol, respectively. Finaly product was dried on a water bath and rest for annealing at 550˚C for 1 hr.

2.2.3. Amalgamation of folic acid templated Fe_2O_3 (FA-Fe_2O_3):

Anhydrous $FeCl_3$ (203 mg) was dissolved in 5 ml ethylene glycol with continuous stirring for 30 min then 5 ml of NaOH (0.25 M) was added drop by drop. Resultant solution was stirred constantly for 30 min (marked as solution A). In the mean time, FA (27.6 mg) was solubilized in 5 ml of Milli Q water and pH was adjusted to ~7.4 by NaOH (0.1 M) treatment (denoted as solution B). Sequentially, drop wisesolution B was added to solution A with continual stirring. The produced mixture was stirred for 30 min and pH was adjusted to ~7.4 using NaOH (0.25 M). Generated solution was transferred into a Teflon-lined stainless-steel sealed autoclave and kept for 18 hr at 150˚C in tranquil heating condition. After reaction tenure, sealed system was naturally cool to ambient temperature. Obtained product was separated through centrifugation, three times washed with Milli Q water and ethanol. End product was dehydrated on a water bath.

2.2.4. Assessment tools and techniques for characterization:

In order to investigate the surface morphology of the samples, Field Emission Scanning Electron Microscopical (FESEM, QUANTA FEG 250) investigations were performed with a diluted drop of NPs on a silicon wafer. Transmission electron microscopy (TEM) grids were prepared with a drop of dilute sample solution to carbon-coated copper grids. The particle sizes were estimated from micrographs at 10^5**X** magnification by using an FEI (Technai S-Twin, operating at 200 kV) instrument. X-ray diffraction (XRD) patterns of the samples were evaluated by using a PANalytical XPERTPRO diffractometer equipped with Cu Kα radiation (at 40 mA and 40 kV) in a scanning rate of 0.02° S^{-1} in the 2θ range within 20° to 80°.Lake Shore vibrating sample magnetometer (VSM) was used to measure Magnetic properties within a field range of 0 to 1.6 T. For the Fourier transform infrared spectroscopy (FTIR), powdered samples were grinded with KBr powder and pelletized. Spectrum was measured on a JASCO FTIR-6300 spectrometer. The background errors were corrected by using a reference of KBr pellets. For optical experiments, the steady-state absorption and emission were carried out with a Shimadzu UV-2600 spectrophotometer and a Jobin Yvon Fluorolog fluorimeter, respectively. A micro-Raman (Horiba LabRAM) setup with an excitation line 532 nm was used in this study to evaluate the Raman scattering spectra of all samples at room temperature. For picosecond-resolved spectroscopic studies, we have perused with methodologies as described in our earlier work (23-24). Dynamic Light scattering (DLS) measurements were performed using a NanoS Malvern instrument equipped with a 4 mW He:Ne laser (λ= 632.8 nm) and a thermostated sample chamber. All the scattered photons are

collected at a 173° scattering angle. The scattering intensity data are processed using the software provided by the manufacturer to obtain the hydrodynamic diameter (d_H) and the size distribution of the scatterer in each sample. The instrument measures the time-dependent fluctuation in the intensity of light scattered from the particles in solution at a fixed scattering angle. d_H is defined as:

$$d_H = \frac{k_B T}{3\pi\eta D} \qquad (1)$$

Where k_B is the Boltzmann constant, T is the temperature, η is the viscosity, and D is the translational diffusion coefficient. In a typical size distribution graph from the DLS measurement, the X-axis shows a distribution of size classes in nanometers, while the Y-axis shows the relative intensity of the scattered light. In all the ROS related extracellular and intracellular experiments homemade LED light has been used.

2.2.5. Evaluating Förster resonance energy transfer (FRET):

To measure attachment of FA (donor) with Fe_2O_3 (acceptor), we applied below-mentioned formulations (25).

The Förster distance (R_0) is given by,

$$R_0 = 0.211 \times [\kappa^2 n^{-4} Q_D J(\lambda)]^{\frac{1}{6}} \quad (\text{In Å})$$

Where, k^2 is a factor describing the relative orientation in space of the transition dipoles of the donor and acceptor. For donor and acceptors that randomize by rotational diffusion prior to energy transfer, the magnitude of $\square^2$ is assumed to be 2/3. The refractive index (n) of the medium is assumed to be 1.496. Q_D, the integrated quantum yield of the donor in the absence of acceptor is ~ 0.005. Molar extinction coefficients (ε_M) for FA of 6197 (363 nm) and 25820 (280 nm).Once the value of R_0 is known, the donor-acceptor distance (r_{DA}) can be easily calculated using the formula,

$$r_{DA}^6 = \frac{R_0^6(1-E)}{E}$$

Where E is the efficiency of energy transfer has been calculated following the procedure of our earlier work (24).

2.3. Results and discussion…

2.3.1. Analysis of Fe_2O_3 and FA-Fe_2O_3 nanohybrid:

FESEM image portrayed in Fig1a and 1b reveled, it was preparedfrom Fe_2O_3 and FA-Fe_2O_3 respectively. Fe_2O_3 has a branched network like morphology having segment length of 300-500 nm and width 50-70 nm. Nano-egg like morphology of length 150-200 nm and width 60-110 nm was elucidated in FA-Fe_2O_3. Corresponding HRTEM images of Fe_2O_3 and FA-$Fe_2O_3$was represented in Figure 1c and 1d and insets show corresponding

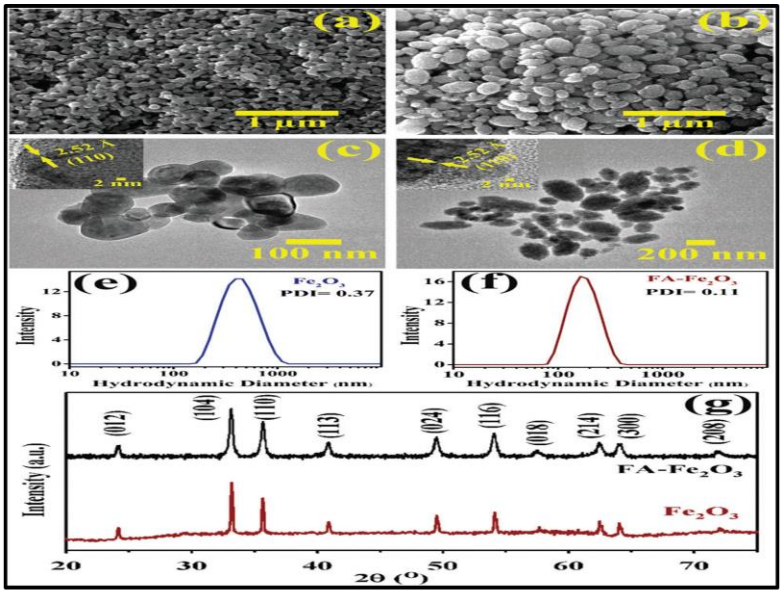

Fig.1.1 FESEM image of (a) Fe_2O_3 and (b) FA–Fe_2O_3 NPs. HRTEM image of (c) Fe_2O_3 and (d) FA–Fe_2O_3 NPs. Inset of (c) and (d) shows the corresponding HRTEM images at higher magnification. Dynamic light scattering data of (e) Fe_2O_3 and (f) FA–Fe_2O_3 NPs dispersed in water. (g) XRD pattern of Fe_2O_3 and FA–Fe_2O_3 NPs.

HRTEM image at higher magnification Fringe distance of both sampleswas measured as 2.52 Å which corresponds to the spacing between (110) planes of α-Fe_2O_3 (26). The dynamic light scattering spectra of Fe_2O_3 and FA-Fe_2O_3 dispersed in water has been shown in Figure 1e and 1f. Hydrodynamic diameter for Fe_2O_3 and FA-Fe_2O_3 NPs was found to be 418 and 180 nm, respectively. The polydispersity index was found to be 0.37 and 0.11 for Fe_2O_3 and FA-Fe_2O_3 NPs respectively. Exclusive alteration in size and morphology of FA-$Fe_2O_3$was due to presence of FA. Here FA is controlling the morphology of FA-Fe_2O_3 NPs. Powder X-ray diffraction pattern of FA-Fe_2O_3 and Fe_2O_3 had been presented in Figure 1g. The diffraction pattern matches with International Centre for Diffraction Data (ICDD) card no 33-0664, which corresponds to α-Fe_2O_3. XRD pattern and fringe distance from HRTEM image imply crystal structure of α-Fe_2O_3 remains intact after FA templated synthesis.

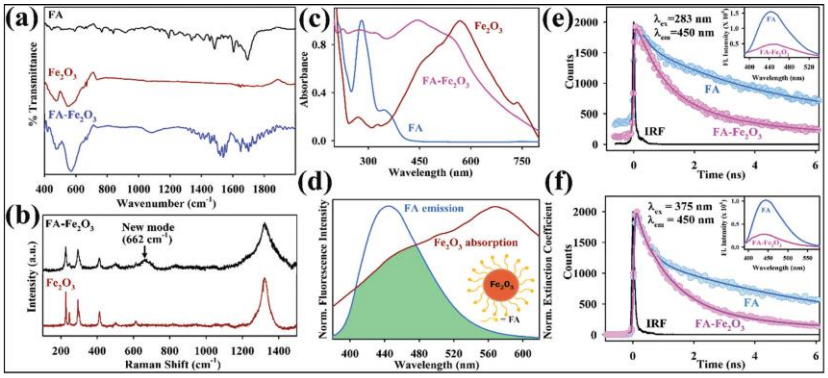

Fig. 2 (a) FTIR spectra of FA, Fe2O3 and FA–Fe2O3. (b) Raman spectra of FA–Fe2O3 and Fe2O3. (c) Absorption spectra of FA, Fe2O3 and FA–Fe2O3. (d) Spectral overlap between emission of FA and absorption of Fe2O3. (e) and (f) are the picosecond-resolved fluorescence transient spectra of FA in the absence and presence of Fe2O3, recorded at 450 nm upon excitation at 283 nm and 375 nm, respectively. Insets show the corresponding steady state emission spectra.

Figure 2a depicted FTIR spectra of FA, Fe_2O_3 and FA-Fe_2O_3. Two sharp peaks at 472 cm^{-1} and 550 cm^{-1}were pinpointed the characteristics of Fe-O stretching in Fe_2O_3 spectrum. The lower frequency absorption was remains unchanged but the higher one get shifted to increased frequency 570 cm^{-1} in FA-Fe_2O_3, which indicated an alteration in size during FA templated synthesis of Fe_2O_3. The sharp peak at 1699 cm^{-1} corresponds to the C=O stretching of carboxylic acid group of FA. In FA-Fe_2O_3, the C=O stretching perturbed into two peaks, one remains at 1699 cm^{-1} and another at 1684 cm^{-1}. This perturbation might be due to one of the free carboxylic acids of FA in FA-Fe_2O_3 and another one gets covalently attached with Fe_2O_3. Peaks in between 1485-1519 cm^{-1} corresponding to phenyl and pterin ring of FA. Raman spectra of Fe_2O_3 and FA-Fe_2O_3 were represented in Figure 2b. Fe_2O_3 had a sharp peaks at 228 cm^{-1} and 500 cm^{-1} corresponding to A_{1g} phonon modes and four E_g phonon modes at 248, 296, 413 and 612 cm^{-1}. Another 2 logitudional optical (2LO) phonon mode at 1324 cm^{-1}. The logitudional optical (LO) phonon mode which is Raman forbidden was not observed in case of Fe_2O_3. But the LO phonon modes was noticed in case of FA-Fe_2O_3 at 662 cm^{-1}, the similar mode was also coined by Onari *et al* (27). This variation is may be due to calcination at higher temperature leading to better crystallinity of Fe_2O_3 than that of un-calcined FA-Fe_2O_3.

Table 1: Lifetimes of picosecond-resolved fluorescent transient of FA and FA-Fe_2O_3

Picosecond resolved fluorescence transient lifetimes	**System**	**λ_{ex} (nm)**	**λ_{em} (nm)**	**τ_1(ns)**	**τ_2(ns)**	**τ_3 (ns)**	**τ_{avg}(ns)**
	FA	283	450	0.25 (35%)	4.50 (65%)	-	3.0
		375	450	0.28 (51%)	6.35 (49%)	-	3.3
	FA-Fe_2O_3	283	450	0.12 (14%)	0.78 (49%)	2.78 (37%)	1.4
		375	450	0.25 (33%)	1.30 (54%)	6.23 (13%)	1.6
FRET parameters of FA-Fe_2O_3		**λ_{ex} (nm)**	**λ_{em} (nm)**	**J (λ)**	**E**	**r_{DA} (nm)**	
		283	450	3.75 X 10^{13}	54.0	1.11	
		375	450	3.75 X 10^{13}	52.0	1.13	

The differences in UV-Vis absorption spectra of Fe_2O_3 and FA-Fe_2O_3 had been clearly depicted in Figure 2c. FA has two well-known absorption bands at 360 and 280 nm. Three possible electronic transitions werenoticed in case of Fe_2O_3 absorption spectra, absorption arising in the range of 200-400 nm mainly due to ligand to metal charge transfer transition (LMCT) from oxygen to iron, absorption band at 445 nm was attributed mainly to pair excitation from $^6A_1 \rightarrow {}^4E$, $^4A_1$ of magnetically coupled Fe^{3+}-Fe^{3+} system and sharp band at 568 nm, which was due to electronic transition from $^6A_1$ to $^4T_2(^4G)$ along with pair excitation of $^6A_1+{}^6A_1 \rightarrow {}^4T_2(^4G)+{}^4T_2(^4G)$. In case FA-$Fe_2O_3$ LMCT band in the wavelength range 200-400 nm and the absorption band at 445 nm gets triggered, surprisingly other one at 568 nm become sedate due to FA functionalization of Fe_2O_3. The significant spectral overlap of emission of FA with absorption of Fe_2O_3 had been shown in Figure 2d. Steady state fluorescence quenching of FA was measured in presence of Fe_2O_3 upon excitation at 283 nm and 375 nm shown in the insets of Figure 2e and 2f, respectively. Steady state emission spectra of FA-Fe_2O_3 indicate the structural integrity of FA remain undisturbed afterhydrothermal synthesis at 150˚C.It waspreviously reported that below 200˚C FA exhibit water loss and degradation occurs after 200˚C. Picosecond resolved fluorescent transients was recorded for both FA and FA-Fe_2O_3 at 450 nm upon excitation at 283 nm and 375 nm as displayed in Figure 2e and 2f,respectively and the corresponding time scales are tabulated in

Table 1.We employed well-known Förster resonance energy transfer (FRET) strategy to validate molecular level attachment of FA with Fe_2O_3.The fluorescence life time of FA is found to be quenched in presence of Fe_2O_3 NPs, which suggest a non-radiative energy transfer process from donor (FA) to acceptor (Fe_2O_3).The donor-acceptor distances (r_{DA}) had been calculated to be 1.11 nm and 1.13 nm for the excitation at 283 nm and 375 nm, respectively and all the other calculated FRET parameters are shown in Table 1.This molecular cross talking between FA and Fe_2O_3 suggests an trend of alteration in activities. Colloidal stability of Fe_2O_3 and FA-Fe_2O_3 NPs dispersed in water were evaluated (Figure 3a). Colloidal stability of FA-Fe_2O_3 was found to be ~40 times higher than Fe_2O_3. Stability of FA-Fe_2O_3 in PBS solution was found to be more than 96 hour.

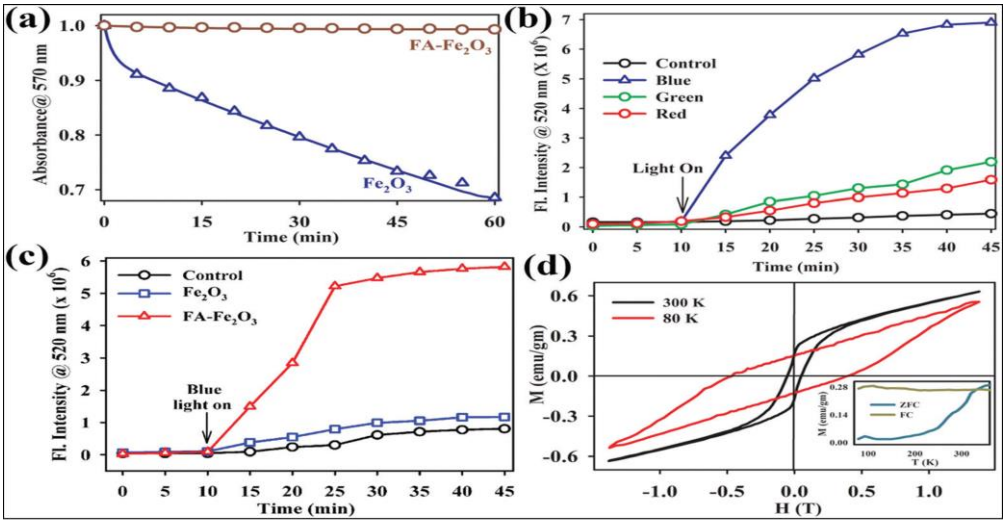

Fig. 3 (a) Colloidal stability of Fe_2O_3 and FA–FA-Fe_2O_3 nanoparticles dispersed in water. (b) DCFH oxidation with respect to time in addition of FA-Fe_2O_3 and control in the dark and with subsequent light (red, green and blue) irradiation. (c) DCFH oxidation with respect to time in addition of Fe_2O_3, FA-Fe_2O_3, and control under dark with subsequent blue light irradiation. (d) Field dependent magnetization (M vs. H) of FA-Fe_2O_3 at 300 K and at 80 K. Bottom right inset shows temperature dependence of MZFC and MFC curves measured at H = 1.6 T

2.3.2. The study of magnetic properties:

Magnetic properties of FA-$Fe_2O_3$was measured by using vibrating sample magnetometer (VSM), which shown magnetic field dependent magnetization (M vs H) at 80 K and 300 K.That pointed hysteresis feature with coercivity 0.43 T and 0.053 T, respectively (Figure 3d). Insets of Figure 3a depict M_{ZFC} curve decreases and M_{FC} rises slowly as a function of

decreasing temperature reveals strong ferromagnetic property and blocking temperature was 332 K.

2.3.3. Extracellular ROS activity:

In vitro ROS generation was evaluated using well known DCFH assay, in which, DCFH is oxidized to fluorescent DCF by reacting with ROS and thus ROS generation monitored using fluorescence of DCF at 520 nm.FA-Fe_2O_3 was assessed for its capability to generate ROS in presence of a range of visible light excitation (blue: 460 ± 15, green: 540 ± 15 and red: 640 ± 15 nm).The maximum ROS generation was observed in presence of blue light (Figure 3b). Blue light induced ROS genertion attributed mainly due to the absorption band of Fe_2O_3at 445 nm, which gets triggered after folic acid fictionalization in FA-Fe_2O_3. This band is mainly responsible for enhanced ROS production through photo inducedelectron-hole pair separation in FA-Fe_2O_3.We further evaluated ROS generation in presence Fe_2O_3 with control under blue light irradiation, which clearly reveals enhanced ROS generation in case of FA-Fe_2O_3 (Figure 3c). The swift nature of ROS generation gets saturated within 15 min, indicating a good signature for PDT application.

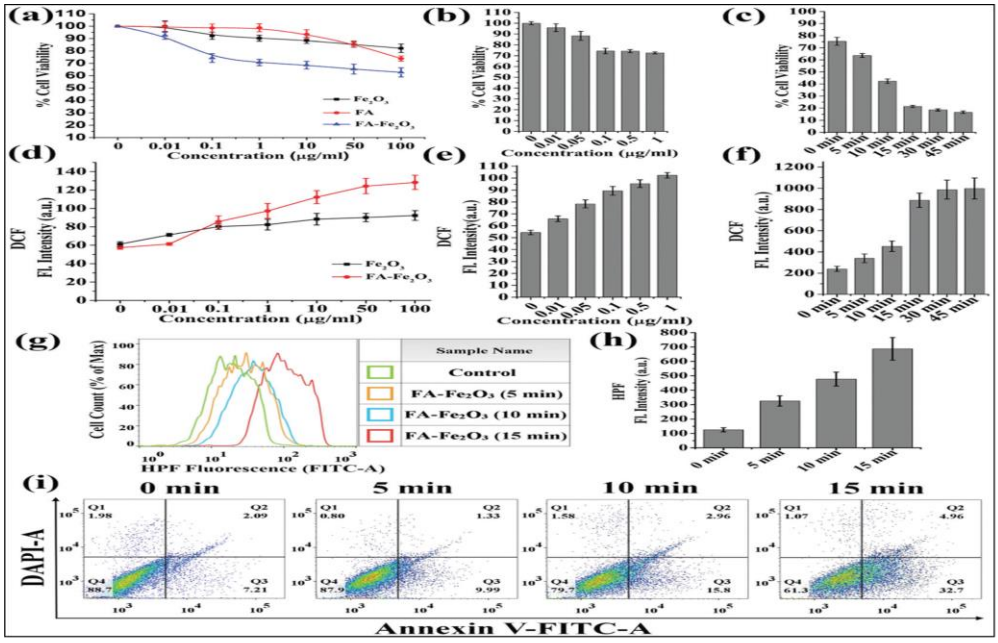

Fig. 4 HCT 116 cells were treated with the requisite amount of drugs for 24h prior to various experiments. (a) MTT assay data with different concentrations of FA, Fe_2O_3 and FA–Fe_2O_3 without blue light. (b) The same at different concentrations of only FA–Fe_2O_3. (c) Light induced cytotoxicity in presence of 0.1 mg/ml FA–Fe_2O_3 (d) Fe_2O_3 and FA–Fe_2O_3 treated dose dependent (0–100 mg/ml) iROS level in terms of DCF fluorescence intensity without blue light treatment. (e) FA–Fe_2O_3 treated dose dependent (0–1 mg/ml) iROS level in terms of DCF intensity without blue light treatment. (f) iROS measurement after treatment with 0.1 mgml1 FA–Fe_2O_3 followed by time dependent blue light exposure. (g) Intracellular hydroxyl radical (OH) after treatment with FA–Fe_2O_3 followed by time dependent blue light exposure (h)Data of hydroxyl radical (OH) determination (i)Annexin V-FITC/DAPI binding levels in FA–Fe_2O_3 (0.1 mg/ml) treated cells

2.3.4. Cytotoxicity study:

To check the cytotoxicity of the nanohybrid (FA-Fe_2O_3) and individual ingredients (FA and Fe_2O_3) HCT 116 cells were subjected to MTT assay without blue light exposure (Figure 4a). HCT 116 cells were incubated with FA, Fe_2O_3 and FA-Fe_2O_3 of different concentrations (0.01, 0.1, 1, 10, 50 and 100 µg/ml). Native FA and Fe_2O_3 do not have significant cytotoxicity up to concentration of 1 µg/ml. However, in case of FA-Fe_2O_3, cell viability was reduced to 70.68% at the same concentration (Figure 4a). After 1 µg/ml concentration the effect FA-Fe_2O_3 on cell viability of HCT 116 cells was almost reached to saturation. To determine the optimum cytotoxicity with lowest concentration of FA-Fe_2O_3 in absence of blue light, another screening was done using FA-Fe_2O_3 of concentration up to 1µg/ml. Figure 4b depicts the optimum cell viability was found to be 70.26% at 0.1 µg/ml concentration of FA-Fe_2O_3. As folic acid a well-known nutrient does not have significant cytotoxicity, we have excluded folic acid from upcoming part of our cellular study.

2.3.5. FA-Fe_2O_3 mediated in-vitro PDT in HCT 116 cell lines:

Next, to ascertain the enhanced intracellular ROS activity of FA-Fe_2O_3 in presence of blue light, HCT 116 cells were incubated with 0.1 µg/ml of FA-Fe_2O_3 and were exposed to blue light for different time duration (5-45 min). A gradual decrease in the cell viability was observed with increase in blue light exposure time (in 5, 10, 15, 30 and 45 min of light exposure cell viability was 63.63%, 42.32%, 21.34%, 18.47% and 16.63%, respectively) as compared to the FA-Fe_2O_3treated cells without light exposure (Figure.4b and 4c). Light dose of 15 min shows maximum effect on cell death (Cell viability 21.34%) and after that the effect is minimal, suggesting a rapid ROS activity of FA-Fe_2O_3 in HCT 116 cells as consistent with extracellular ROS generation. In vitro PDT experiment illustrates the photodynamic effect of FA-Fe_2O_3 and also suggests a direct indication of photosensitized cytotoxicity of FA-Fe_2O_3 nanohybrid in HCT 116 cells.

2.3.6. Intracellular ROS activity in absence and presence of blue light:

Intracellular ROS generation experiment was done by using cell permeable dye DCFH-DA. HCT 116 cells were incubated with Fe_2O_3 and FA-Fe_2O_3 of different concentrations (0.01, 0.1, 1, 10, 50 and 100 µg/ml) to determine ROS activities without blue light exposure.As shown in Figure 4d, Fe_2O_3 does not have significant ROS activity without blue light exposure. Moreover, Fe_2O_3 has minimal ROS activity in extracellular condition (as

shown in Figure 3b) in presence of blue light. Hence Fe_2O_3 have been excluded for further experiment. Figure 4d depicts FA-Fe_2O_3 treated cells shows moderate increase in DCF fluorescence intensity with respect to the Fe_2O_3 treated cells.Another screening was done in absence of light with 0-1 µg/ml of FA-Fe_2O_3. Figure 4e depicts moderate intracellular ROS activity of the nanohybrid in absence of blue light at a concentration 0.1 µg/ml. Initial cytotoxicity study showed 0.1 µg/ml of FA-Fe_2O_3 have optimum effect on cell viability in absence of blue light. To ascertain the intracellular ROS level in presence of blue light with optimum dose of FA-Fe_2O_3, cells were treated with 0.1 µg/ml FA-Fe_2O_3.Treated cells were exposed to blue light for differential time duration (5, 10, 15, 30 and 45 min). Figure 4f depicts ROS generation was gradually increased with increasing blue light exposure time (1.42, 1.88, 3.69, 4.11 and 4.15 fold in 5, 10, 15, 30 and 45 min, respectively). The trend in intracellular ROS generation reached to saturation with 15 min of light exposure, which is consistent with both extracellular ROS generation and photo induced cytotoxicity assay. Considerable light induced enhanced intracellular ROS activity and optimum dark toxicity of 0.1 µg/ml dose of FA-Fe_2O_3 indicates its potential in PDT.

2.3.7. Nature of intracellular ROS:

Earlier reports hadwell evidently established that amongst the numerous free radicals, the hydroxyl radical is commonly found cellular free radical that is generated through oxidative stress, causes cell death (8). For the assessment of the type of ROS produced within the cell by light-sensitized FA-Fe_2O_3, flow cytometric study of intracellular ROS generation was conducted by using specific florescent probe HPF, a marker for hydroxyl radical (28). Pretreated cells with 0.1 µg/ml of FA-Fe_2O_3 was exposed to different light dose of 5, 10 and 15 min. A gradual ($p<0.05$) increase in HPF fluorescence intensity was observed (2.67, 4, 5.17 fold in 5, 10 and 15 min, respectively) with increasing light exposure time (Figure. 4g and 4h). The observation reveals that enhanced cytotoxicity upon blue light exposure is due to the generation of hydroxyl radical within the cell in presenceFA-Fe_2O_3.

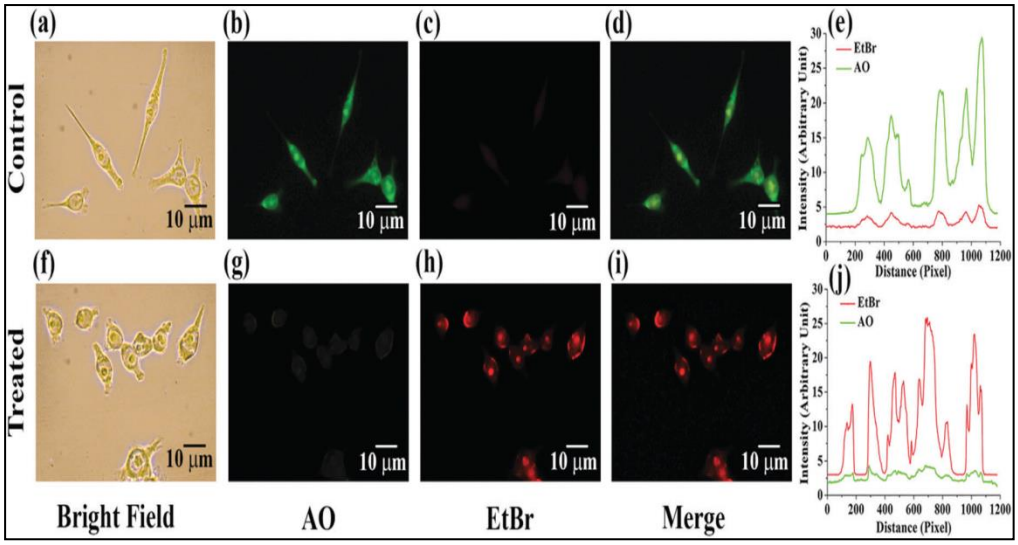

Fig. 5 Morphological changes of FA–Fe_2O_3 (0.1 mg/ml for 24 h) treated HCT 116 cells followed by blue light exposure (15 min). image after AO and EtBr staining (e) and (j) Change in AO and EtBr fluorescence intensity of control and treated cells.

2.3.8. FA-Fe_2O_3 induced apoptosis in HCT 116 cells:

Phosphatidylserine (PS), a phospholipid of plasma membrane, usually located inner side of the membrane, but in apoptotic condition, they are trans located in the membrane and externalized during apoptosis (29). Annexin-V is a specific PS-binding protein that can be used to detect the apoptotic cells when conjugated with a specific fluorophore. On the other hand DNA binding dye DAPI was used along with annexin V to assess the degree of apoptosis and necrosis.To find out the underlying mechanism of photodynamic effect of FA-Fe_2O_3 on HCT 116 cells; flow cytometric technique was used using Annexin V-FITC/DAPI. The percent viable cell population in FA-Fe_2O_3 treatment without light exposure was 88.7% following mild early apoptosis of 7.21%, late apoptosis of 2.09% and necrosis of 1.98%. Interestingly, the percent of apoptotic (early and late) population was progressively increased with the time of exposure (5, 10 and 15 min) of light in FA-Fe_2O_3 pretreated cells (Figure. 4i). With 15 min exposure of light, the viable cells were reduced to 61.3% following the enhancement of early/late apoptotic and necrotic population of 32.7%, 4.96% and 1.07%, respectively.

To further confirm the degree of apoptosis and necrosis upon treatment with FA-Fe_2O_3 in presence of light, fluorescence microscopic analysis was conducted using nuclear staining dye, AO and EtBr (Figure 5a-5i). Cells were pretreated with FA-Fe_2O_3 had intact nucleus

with strong green AO fluorescence and weak red EtBr fluorescence (5b and 5c). The scenario was reverse in presence of light as shown in Figure 5c and 5h, demonstrating clear nuclear fragmentation, which is also observed from the intensity curves (Figure 5e and 5j).

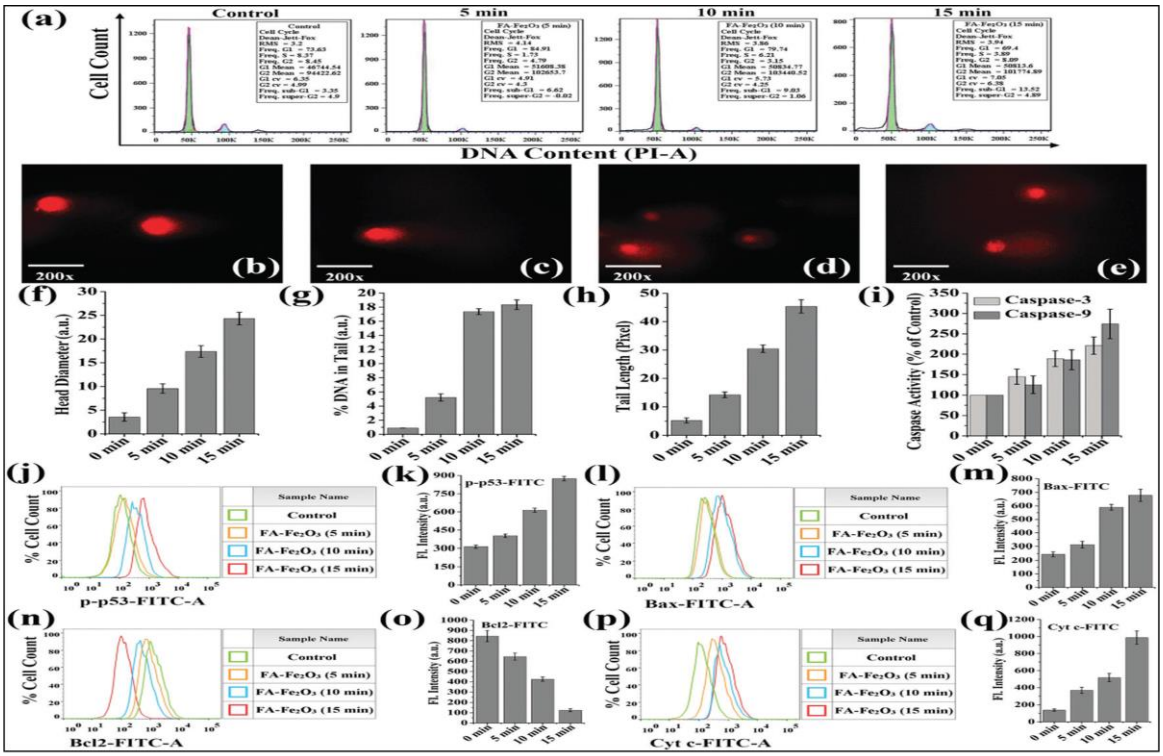

Fig. 6 HCT 116 cells were treated with FA–Fe_2O_3 for 24 h followed by time dependent blue light exposure prior to various experiments. (a) DNA content in each phase of the cell cycle. Representative microscopic images of comet assay. (b) Control. (c) 5 min. (d) 10 min. (e) 15 min blue light exposure. Comet score analyzed data of microscopic image (f) Head diameter. (g) % of DNA in tail. (h) Tail length. (i) Caspase 3 and Caspase 9 activity. Analysis of (j) p53Ser46, (l) Bax, (n) Bcl2, and (p) cytochrome c protein expressions, respectively. Flow Jo data of (k) p53Ser46, (m) Bax, (o) Bcl2 and (q) cytochrome c protein expression, respectively.

2.3.9. Analysis of DNA content in sub G0-G1 phase of cell cycle:

The estimation of fractional DNA content (Sub G0-G1) in cell cycle is widely used as a marker to determine apoptosis.Thus, to investigate the PDT effect of FA-Fe_2O_3 on HCT 116 cells underlying the role of apoptosis, flow cytometric assessment of percentage of DNA content in sub G0-G1 phase of cell cycle was analyzed (Figure 6a). After treatment cells show the percentage of DNA content 3.35% without any blue light exposure. After blue light exposure with different time duration (0-15 min) there was a significant enhancement in percentage of DNA content (6.62, 9.03 and 13.52 percent in 5, 10 and 15 min, respectively)

of sub G0-G1 phase. The results demonstrate the role of fragmented DNA regulating the apoptotic machinery in light induced FA-Fe_2O_3 mediated PDT.

2.3.10. FA-Fe_2O_3 induced nuclear DNA damage in HCT 116 cells:

Nuclear DNA damage upon the blue light exposure on FA-Fe_2O_3treated cells was further confirmed by comet assay, which is a single cell gel electrophoresis assay for the rapid and sensitive of DNA damage. In case of treated cell without blue light exposure migration of DNA from the origin was not significant, with increasing light exposure time tail length of damaged DNA increases, taking the shape of a comet (Figure.6b-6e).The head diameter in (2.70, 4.90 and 6.87 fold in 5, 10 and 15 min, respectively), % DNA in tail (5.88, 19.51 and 20.62 fold in 5, 10 and 15 min, respectively) and tail length (2.72, 5.82 and 8.67 in 5, 10 and 15 min, respectively) were significantly ($p<0.05$) increased with the gradual increase of blue light exposure time on FA-Fe_2O_3 treated cells. However, without light exposure on FA-Fe_2O_3 treatment did not show any upliftment of DNA damage indices (head diameter, % DNA in tail and tail length) as compared with light exposed treated cells (Figure 6f-6h). Light induced enhanced ROS generation damages nuclear DNA in HCT 116 cells.

2.3.11. FA-Fe_2O_3up regulates the expression of phosphorylated p53 at Ser 46 in HCT 116 cells:

Numerous studies have revealed that ROS act as an upstream signal transducer for the p53 activation and as a downstream mediator of apoptosis. To understand the involvement of p53 phosphorylation in photosensitized apoptosis machinery, flow cytometric assessment was conducted in FA-Fe_2O_3-treated cells in presence of blue light. Phosphorylation of p53 expression significantly augmented with an increase in light dose 5-15 min (Figure 6j). As found in the flow cytometry analysis, the fluorescence intensity of p-p53-FITC was gradually ($p<0.05$) increased (1.29, 1.97 and 2.79 fold in 5, 10 and 15 min respectively) with respect to the FA-Fe_2O_3 treated control cell without any blue light exposure, indicating the correlation of ROS mediated p53 phosphorylation at Ser 46 in photodynamic therapy (Figure 6k).

2.3.12. FA-Fe_2O_3 modulates the regulation of mitochondrial-dependent apoptosis machinery in HCT 116 cells:

An altered level of pro/anti apoptotic proteins, Bax, Bcl2 have been shown to regulate the mitochondrial-dependent apoptosis process through the modulation of phosphorylated p53 (Ser 46). Loss of function in anti apoptotic Bcl2 triggers the release of cyt c to the cytosol in

initiating the apoptotic cascade. To evaluate the detailed mechanism of FA-Fe_2O_3 induced apoptosis in presence of blue light, flow cytometric assessment of mitochondrial-dependent apoptosis regulating protein Bax, Bcl2 and cytochrome c was carried out (Figure 6l, 6n and 6p). As shown in the flow cytometric histogram, the relative FITC fluorescence intensities of Bax (1.27, 2.40 and 2.76 fold in 5, 10 and 15 min respectively) and cyt c (2.66, 3.74 and 7.13 fold in 5, 10 and 15 respectively) were gradually increased with increase in duration of light treatment (Figure 6l, 6m,6p and 6q). On the other hand, the expression of anti-apoptotic Bcl2 was significantly ($p<0.05$) suppressed (0.76, 0.50 and 0.15 fold in 5, 10 and 15 min respectively) with an increase in light duration of light treatment compared to without any light treatment (Figure 6n & 6o). Therefore FA-Fe_2O_3 mediated PDT in HCT 116 cells initiate mitochondrial-dependent apoptosis through p53 phosphorylation and associated with ROS mediated pathway.

2.3.13. FA-Fe_2O_3 enhances the Caspase 3/9 activation in HCT 116 cells:

Caspase, a family of proteases, is responsible for triggering the apoptosis by cleaving the specific enzymes. Up regulation of Bax/cytochrome c can induce caspase activation which is responsible for initialization of apoptosis. Correlating with the data, a gradual augmentation of caspase 3/9 activity (1.45, 1.89, 2.21 in 5, 10 and 15 min, respectively for caspase 3 activity and 1.25, 1.86 and 2.74 fold in 5, 10 and 15 min, respectively for caspase 9 activity) were found when the FA-Fe_2O_3 pretreated cells were exposed to blue light for different time duration (5, 10 and 15 min, Figure 6i). Along with p53, Bax and Bcl2 protein expression caspase 3 and caspase 9 activity confirms that FA-Fe_2O_3 mediated PDT in HCT 116 cells induces cell death via an apoptotic pathway.

The nanohybrid (FA-Fe_2O_3) possesses selectively blue light sensitized enhanced ROS activity without any. At optimum concentration of 0.1 µg/ml the nanohybrid possesses optimum dark toxicity and considerable light toxicity for the implementation of PDT. Upon blue light irradiation both in extracellular and intracellular condition, FA-Fe_2O_3 rapidly generates ROS, which is found to be hydroxyl radical from HPF staining experiment (Figure 4g and 4h). Light induced intracellular ROS generation causes nuclear DNA damage, which leads to increase in p53 protein expression inside the cell followed by up regulation of mitochondrial Bax protein and decrease in Bcl2 protein level. Mitochondrial started releasing cyt c leads to activation of pro Caspase 9 and Pro Caspase 3 to Caspase 9 and Caspase 3 respectively, ultimately cell death occur via apoptotic pathway.

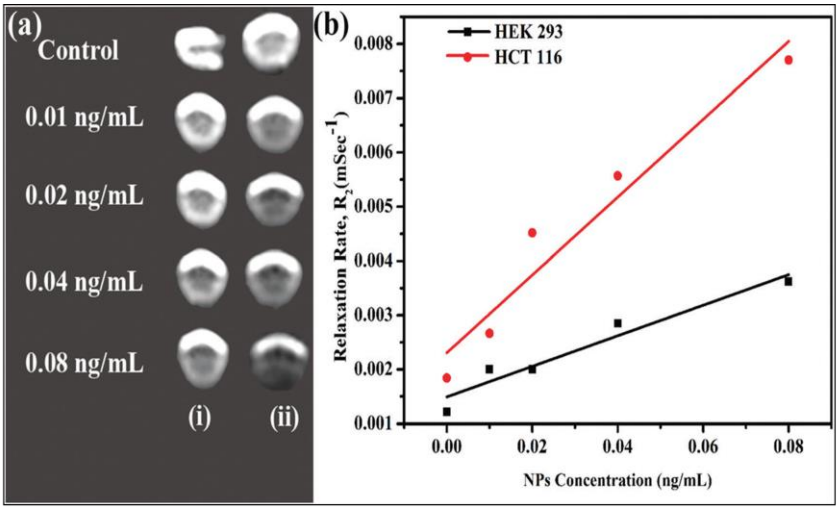

Fig. 7 (a) T2 weighted MRI phantom images of (i) HEK 293 and (ii) HCT 116 cells treated with different concentrations of FA–Fe2O3. (b) Relaxivity study of FA–Fe2O3 incubated in HEK 293 and HCT 116 cell lines.

2.3.14. MRI study:

To test the potential applicability of FA-Fe_2O_3 as a diagnosis tool for cancer in vitro MRI study has been performed on HCT 116 cells along with HEK 293 cells as control. Figure 7a represents T2 weighted phantom images of FA-Fe_2O_3 treated HEK 293 and HCT 116 cells. Signal intensity changes (from bright to dark) with an increase in concentration of FA-Fe_2O_3 (from 0.01-0.08 ng/ml) nanohybrid was observed in case of HCT 116 compare to HEK 293 cells indicating targeted delivery of FA-Fe_2O_3 in FR over expressed cells. Relaxivity plot (Figure 7b) indicates a linear relation of relaxation rate (R_2 = 1/T2) with the nanohybrid concentration (30). With increasing concentration of FA-Fe_2O_3, the transverse relaxation time (T2) of the protons of water decreases and relaxation rate (R_2) increases leading to darkening of the specific region of interest. This indicates FA-Fe_2O_3 being a potential T2 contrast agent.

Along with therapeutic property FA-Fe_2O_3, it has also potential MRI contrasting ability in HCT 116 cells. Shaoo et al. developed a FA conjugated silica coated manganese ferrite (FA-MSN) NPs for targeted delivery and MR imaging. FA-MSN shows MRI contrasting at 0.05 mg/ml concentration, whereas in case of FA-Fe_2O_3 we found excellent contrasting in cancer cell at 0.08 ng/ml, which is ~1000 times lower concentration with respect to the optimum dose found for the PDT. Compare to the FR deficient cells pronounced contrasting in FR+ cancer cells at very low concentration reveals its efficiency as a MRI contrast agent. FA

mediated targeted delivery, light sensitized enhanced ROS activity and MRI contrasting competence of FA-Fe_2O_3 leads to a potential biomaterial for dual application for diagnosis and therapy colorectal cancer.

2.4. Conclusion:

In summary, we have developed a facile and cost effective synthesis methodology of a novel nanohybrid (FA-Fe_2O_3), which characterized blue light sensitivity with target specificity andanti cancer activity in human colorectal carcinoma cell line along with MRI contrasting abilities.

Molecular level analysis shown attachment of FA with Fe_2O_3 was confirmed frompicosecond resolved fluorescence study. Enhanced ROS activity was confirmed fromextracellular and intracellular DCFH oxidation assay with different light exposure time.Cytotoxicity study in HCT 116 cells with different light exposure time reveals photoinduced enhanced cytotoxicity.Analysis of DNA content in sub G0-G1 phase of cell cycle and comet assay reveals ROS mediated nuclear DNA damage in HCT 116 cells. ROS mediated cell death via apoptotic pathway is evident from p53, Bax, Bcl2 and cytochrome c protein expression. Apoptosis mediated cell death was further confirmed from caspase 9 and caspase 3 activity. For diagnosis purpose in vitro MRI study reveals excellent contrasting in FR overexpressed cancer cell (HCT 116) than FR deficient normal cell (HEK 293). Such blue light induced PDT, can be done where affected tissues can be exposed to blue light using optical fiber (e.g lung cancer, colorectal cancer, stomach cancer, throat cancer etc.). Finally, this work elicits a new approach towards synthesis of effective, low cost nanohybrid for diagnosis and therapy of colorectal carcinoma.

2.5. References:

1. N. C. S. Initiative, London, National Cancer Survivorship Initiative, 2013.

2. H. J. Burstein, *J. Clin. Oncol.*, 2000, 18, 693.

3. T. J. Dougherty, G. Grindey, R. Fiel, K. R. Weishaupt ,D. Boyle, *J. Natl. Cancer Inst.*, 1975, 55, 115–121.

4. Z. Huang, H. Xu, A. D.Meyers, A. I. Musani, L.Wang, R. Tagg, A. B. Barqawi ,Y. K. Chen, *Technol. Cancer Res. Treat.*, 2008,7, 309–320.

5.D. Zhang, M. Wu, Y. Zeng, L. Wu, Q. Wang, X. Han, X. Liu , J. Liu, *ACS Appl. Mater. Interfaces*, 2015, 7, 8176–8187.

6. Z. Liu, X. Liu, Y. Du, J. Ren , X. Qu, *ACS Nano*, 2015, 9,10335–10346.

7. E. Ju, K. Dong, Z. Chen, Z. Liu, C. Liu, Y. Huang, Z. Wang,F. Pu, J. Ren ,X. Qu, *Angew. Chem.*, 2016, 128,11639–11643.

8. Z. Hu, J. Li, C. Li, S. Zhao, N. Li, Y. Wang, F. Wei, L. Chen , Y. Huang, *J. Mater. Chem. B*, 2013, 1, 5003–5013.

9. A. C. Antony, *Blood*, 1992, 79, 2807–2820.

10. Y.-k. Lee, *Macromol. Res.*, 2006, 14, 387–393.

11. P. Garin-Chesa, I. Campbell, P. Saigo, J. Lewis Jr, L. Old ,W. Rettig, *Am. J. Pathol*., 1993, 142, 557–567.

12. A. R. Hilgenbrink and P. S. Low, J. Pharm. Sci., 2005, 94,2135–2146.

13. C.-H. Wang, C.-W. Chang and C.-A. Peng, *J. Nanopart. Res.*,2011, 13, 2749–2758.

14. H. Meng, J.-Y. Chen, L. Mi, P.-N. Wang, M.-Y. Ge, Y. Yue,N. Dai, *J. Biol. Inorg. Chem.*, 2011, 16, 117–123.

15. P. Suriamoorthy, X. Zhang, G. Hao, A. G. Joly, S. Singh,M.Hossu, X. Sun ,W. Chen, *Cancer Nanotechnol.*, 2010,1, 19–28.

16. J.-J. Lin, J.-S. Chen, S.-J. Huang, J.-H. Ko, Y.-M. Wang, T.L.Chen ,L.-F. Wang, *Biomaterials*, 2009, 30, 5114–5124.

17. J. L. Arias, L. H. Reddy and P. Couvreur, *J. Mater. Chem.*,2012, 22, 7622–7632.

18. L. Li, M. Nurunnabi, M. Nafiujjaman, Y. Y. Jeong, Y.-k. Lee, K. M. Huh, *J. Mater. Chem. B*, 2014, 2, 2929–2937.

19. Z. Medarova, W. Pham, C. Farrar, V. Petkova , A. Moore,*Nat. Med.*,2007, 13, 372–377.

20. Y. Liu, H. Miyoshi, M. Nakamura, *Int. J. Cancer*, 2007,120, 2527–2537.

21. A. J. Ditto, K. N. Shah, N. K. Robishaw, M. J. Panzner, W. J.Youngs , Y. H. Yun, *Mol. Pharmaceutics*, 2012, 9, 3089–3098.

22. S.Mohapatra, S.Mallick, T. Maiti, S.Ghosh , P. Pramanik, *Nanotechnology*, 2007, 18, 385102.

23. P. K. Sarkar, N. Polley, S. Chakrabarti, P. Lemmens ,S. K. Pal, *ACS Sens.*, 2016, 1, 789–797.

24. S. Choudhury, G. Naiya, P. Singh, P. Lemmens, S. Roy,S. K. Pal, *ChemBioChem*, 2016, 17, 605–613.

25. J. R. Lakowicz, Principles of Fluorescence Spectroscopy,Kluwer Academic/Plenum, New York, 2nd edn, 1999.

26. S. Chakrabarty, T. Jana, K. De, S. Das, K. Dey, K. Chatterjee, *Mater. Res. Express*, 2014, 1, 046104.

27. S. Onari, T. Arai, K. Kudo, *Phys. Rev. B: Condens. MatterMater. Phys.*, 1977, 16, 1717.

28. M. Price, J. J. Reiners, A. M. Santiago, D. Kessel, *Photochem.Photobiol.*, 2009, 85, 1177–1181.

29. I. Vermes, C. Haanen, H. Steffens-Nakken ,C. Reutellingsperger, *J. Immunol. Methods*, 1995, 184, 39–51.

30. B. Sahoo, K. S. P. Devi, S. Dutta, T. K. Maiti, P. Pramanik ,D. Dhara, *J. Colloid Interface Sci.*, 2014, 431, 31–41.

Chapter 3

Phloroglucinol Bearing Covalent Organic Framework: An Effective Anticancer Agent

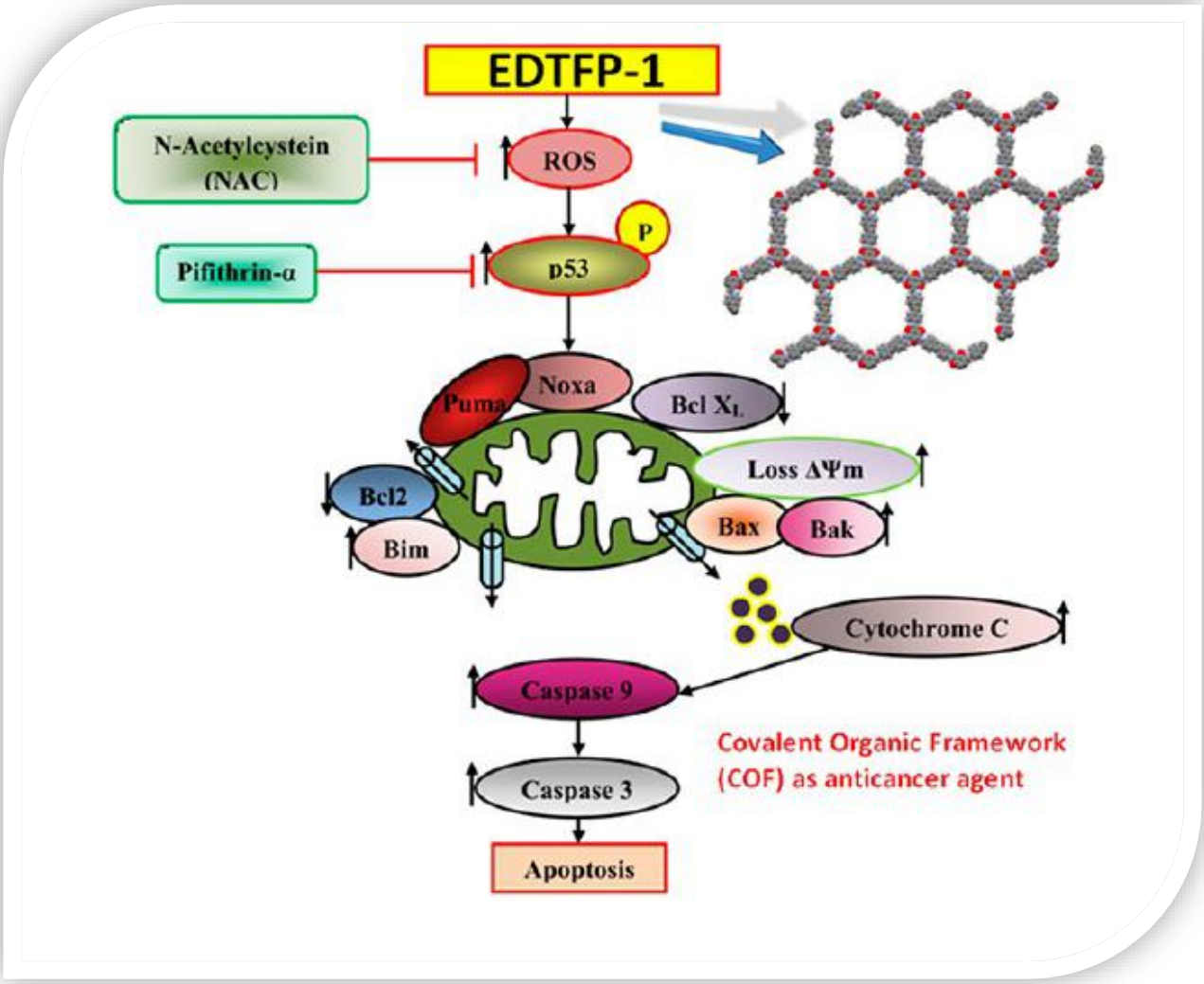

3.1. Introduction...

Mortality in cancer within this advanced medical therapeutic practice is enormous (1). According to world health organization, 18.1 million new patients were registered and among them 9.6 million cancer patients were expired in 2018, which is statistically second leading cause of human mortality. There were four keys to control cancer: early detection, diagnosis, treatment and palliation. But in developing countries treatment scenario was too much painful. There were 70% of cancer death comes from under developing countries. GLOBOCON 2018 and CA: Journal for clinician reported Lung cancer was predominant in all of the cancer cases; it takes 11.6% of total cancer patients and liquidated 18.4% of all the patients (2). These statistical values broadcasted not only current crucial situation but also forecasted upcoming prejudice and calamities. That will obligated towards extensive scientific research and develop new therapeutics to procure as many as patient's life. But involvement of several organs has made therapeutic progression little harder, so precise management strategies was still unspecified (3-5). WHO suggested many strategies and that all were well practiced, like surgery, radiation therapy, chemotherapy, hormonal therapies, Immuno therapies, active bimolecular therapy etc. Conventional cancer management with chemotherapeutic drugs suppress tumour progression in a certain extent (6). Success rate of this costly procedure wasn't very impressive. But all possible therapeutics weakens tumour cell growth to a certain extent, but contains many more side effects like high maintained treatment and after surgery medications, life threatening associated health issues (7, 8). Vanquish on such limitations researchers everyday tried to not only innovate much more cost effective sophisticated medicinal compounds, materials and chemo drugs but also reconnoitre and denote materials and its derivatives having anticancer properties (9-12).

Formulated novel and effective porous organic nano materials, investigators have synthesized COFs in a broad scale through polymerization of building blocks comprises enamine, imine, azine, hydrazine, beta-ketoenamine and boronate esters (12-15). Those have strong dynamic covalent bond with formulated nano architectures. Periodicity of the porous grid helps these materials to potentiate over associated conjugated microporous polymers, covalent triazine frameworks and porous organic polymers. Inherent properties, such as large as accessible pore size, specific surface area, channel type-ordered structure, low density, crystallinity and high thermal stability are also chief characters that can facilitated as a remarkable beneficiary advantage than metal organic frameworks. Popular COFs, zeolites, functionalized mesoporous materials and porous graphene nanocomposites can also be utilised for

biomedical applications as they are devoid of harmful/ hazardous metallic compounds (16). Therefore, this type of nano compound is highly lucrative not only for cell biologist to use as cargo for chemo or other drug delivery, imagining and cancer therapeutics, but also for inventors associated with chemical industry as storage for gas, hazardous catalysts, proton condition, Li-storage, photo responsive material etc(17-22). In biomedical industries, COFs, can be used as nano carrier, due to their unfilled vast internal barren space, with specific application associated with enzyme immobilization and drug delivery (23). Their frame work is characterized with porous biomaterials with Polyphenolic moieties, which potentiates anticancer activity (24).

Present improvement in cell and molecular biology advised apoptosis as an effective, precise and well organized regulator of cellular homeostasis (25). Cellular morbidity is achieved with this process, characterised by nuclear DNA fragmentation, chromatin condensation, membrane blebbing followed by cell shrinkage, modulation of pro and anti apoptotic proteins and associated factors. There are two groups of genes located in DNA, one group induce pro-apoptotic protein expression (p53, Rb, Bad, Bim, Bid, PUMA and NOXA) and other group inhibits apoptosis (26, 27). This anti-apoptotic proteins are Bcl-2 and Bcl-XL(28). It is well reported that apoptotic process is triggered by p53-DNA damage sensitive protein that transcribe required genes and govern the entire process. Entire apoptotic process is carried out in two different ways, either intrinsic or extrinsic (27). Changes in mitochondrial membrane potential and pore formation in mitochondrial membrane is due to alteration in Bcl2/BclXL that release pro-apoptotic Bid, Bad protein via its truncation(28). Truncated Bid translocated in mitochondrial membrane and make leakage in this membrane. This pore formation release Cytochrome C form mitochondrion vessel. Cytochrome C activates initiator and executor Caspase enzymes through Proteolytic cleavage (29-31). Reactive oxygen species and their derivatives actively take a part in maintaining normal cellular homeostasis (32). Its dissassemblance results cellular and physiological disorders such as inflammation, cancer and associated diseases. Therefore, induction of apoptosis in cancer cells by any compound/ materials can open a new therapeutic approach for the nano-biotechnological approach. Above mentioned incidents guided us to explore anticancer activity of a novel COF material EDTFP-1 and elucidate underlying molecular mechanism involved in this therapeutic process. Through this study we demonstrated porous polymer EDTFP-1 played as apoptotic inducer in *in-vitro* system by tinkering mitochondrial

membrane potential followed by requisite alteration in pro-apoptotic factors and DNA fragmentation.

3.2. Material & Methods: Synthesis…

3.2.1. Chemicals:

Phloroglucinol (M = 126.11 g/mol), hexamine (M = 140.18 g/mol), and 4, 4′-Ethylenedianiline (M = 212.29 g/mol) were purchased from Sigma-Aldrich, St. Louis, MO, USA. Trifluoroacetic acid (99.5%) was obtained from Alfa Aesar. Hydrochloric acid (HCl) and anhydrous dimethylformamide (DMF) was used without further purification.

3.2.2. Synthesis of EDTFP-1:

To start with, 2, 4, 6-triformylphloroglucinol (TFP) was synthesized following a earlier established protocol (33). In brief, tri-fluoroacetic acid and phloroglucinol and were mixed up in 250mL round-bottom flask containing hexamethylenetetramine. The mixture was stirred in a preheated (100 °C) oil bath for 2h under inert atmosphere. HCl was then supplemented to reaction mixture gradually with vigorous stirring at the same temperature for another

1 h followed by a filtration in the cold Celite bed. The filtrate part was subjected to extraction for four times with dichloromethane, and anhydrous sodium sulfate was used to soak moisture. Rotary evaporator was used for solvent evaporation. After evaporation, the off-white colored fluffy product was obtained and characterized by FTIR, 1H NMR, and 13CNMR spectroscopic techniques.

For a typical synthesis of EDTFP-1, 210 mg (1 mmol) of TFP was dissolved in a cleaned two-neck round-bottom flask containing anhydrous DMF (10 mL). The solution of 4,4′-ethylenedianiline in anhydrous DMF was then injected into the above solution using a syringe. The resulting solution mixture was kept in reflux condition under nitrogen containing atmosphere for 12 h at 150 °C for about to get the golden yellow colored solid product following a vigorous filtration and thoroughly washing with DMF as well as ethanol for several times to get rid of unreacted organic compounds. An advanced Soxhlet extraction was engaged to eradicate the impurity from the surface of the material. We have used methanol as a washing solvent. At last, the material was dried for 2 h in a 75 °C oven, and the synthesized COF was denoted as EDTFP-1 (Figure 1A). To determine the structure of the newly synthesized COF and to calculate the unit-cell parameters, possible 2D models were standardized by the Material studio (34). Several stacking possibilities were measured following the reported literature data.

3.2.3. Instrumentation:

A Bruker D8 Advance SWAX diffractometer using a fixed voltage (40 kV) and current (40 mA) was used to get the powder X-ray diffraction patterns of the EDTFP-1 samples. The XRD machine was calibrated with conventional silicon source employing Ni-filtered Cu Kα radiation with λ = 0.15406 nm. Quantachrome Autosorb 1-C surface area analyzer was employed for the nitrogen adsorption/desorption investigation at 77 K. Before the gas adsorption; in brief, the sample was initially degassed for 12 h at 403 K under high vacuum. NLDFT pore size distributions were determined from the N2 sorption isotherm using the carbon/cylindrical pore model.

For TEM analysis, 10 mg of the EDTFP-1 sample was dispersed into absolute ethanol for 5 min under sonication and this is followed by the coating of the sample on a copper grid followed by drying in air before analysis. In order to analyze the morphology as well as the particle size of the EDTFP-1 samples, JEOL JEM 6700 field emission-scanning electron microscope (FE SEM) was used. A series of high-throughput biophysical spectral analysis of the samples was carried out, mainly FT-IR (Nicolet MAGNA-FT IR 750 spectrometer Series II), UV−visible diffuse reflectance spectroscopy (UV 2401PC), and 13C CP MAS NMR spectroscopic analysis (Bruker Advance 500 MHz NMR). A TA Instruments thermal analyzer TA-SDT Q-600 was employed for the thermogravimetric (TG) and differential thermal analysis (DTA) of EDTFP-1 under air flow with a temperature ramp of 10 °C/min. A Vario EL III CHNOS elemental analyzer was employed for the determination of carbon, hydrogen, and nitrogen contents in the EDTFP-1 material. Additionally, 1H, together with 13C NMR spectra of the TFP monomer was taken on a Bruker DPX-300/500 NMR spectrometer. To check the stability of this COF in water, we have treated 100 mg of each of the EDTFP-1 samples with three aqueous buffer solutions of pH 5.5, 7.0, and 7.4. After these water treatments, the nanostructure and compositions of the samples were analyzed by XRD, FE SEM, and FT IR spectroscopy. Weight of EDTFP-1 samples after pH treatments were 99, 98, and 98 mgs for the solution pH of 5.5, 7.0, and 7.4, respectively. Further, particle size distributions in these aqueous dispersions were analyzed through dynamic light scattering (DLS) experiment by using a Malvern, UK, Zetasizer nano zs 90.

3.3. RESULTS AND DISCUSSION..

3.3.1. Elucidated powder X-Ray diffraction study.

The powder XRD pattern of EDTFP-1 material was displayed in Figure 1. The experimentally obtained 2θ values were validated satisfactorily with the theoretical simulated powder pattern (Figure 1B) of near-eclipsed stacking model. Presently, we advise the structure was close to hexagonal space group (*P6/m*) for EDTFP-1by comparing the experimental and simulated PXRD patterns. As elucidated in the Figure 1B, the EDTFP-1 displayed three broad peaks below 10 degrees of 2θ, centered at 5.7, 6.6 and 8.7 degrees of 2θ. The π–π stacking distance between COF layers was measured to be 3.49 Å from the d spacing between 001 planes. A possible 2D model was prepared with an eclipsed structure in the hexagonal space group (P6/m), by using the software Materials Studio. The unit cell parameters was found to be (a = b = 30.5 Å, c = 3.49 Å, α = β = 90.0° and γ = 120.0°. Unit cell volume was 2813.14 $Å^3$, Ball-stick model corresponding to the optimized crystal structure obtained from this powder XRD data revealed 3D-hexagonal crystal structure with unit cells as shown in Figure 1C and 1D.

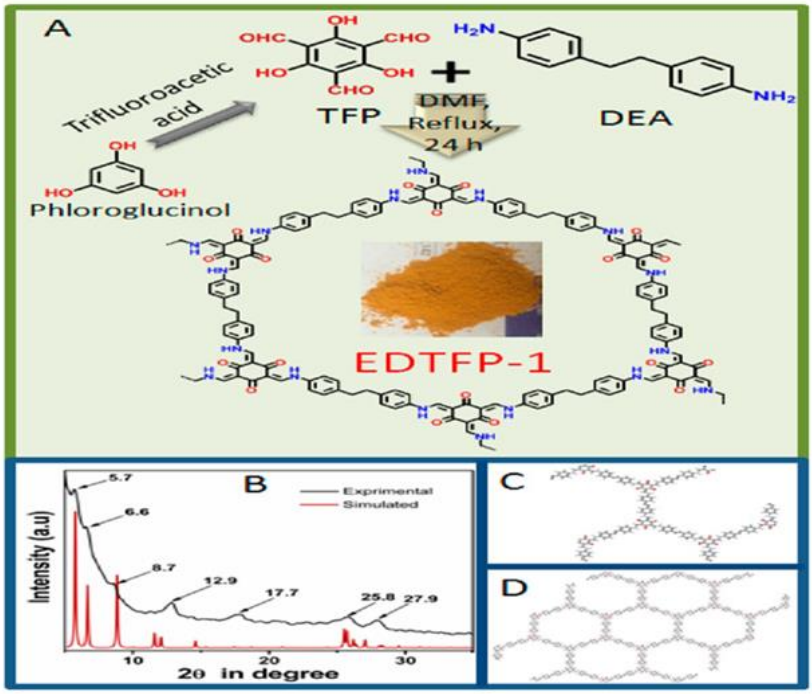

Figure 1. (A) Schematic representation for formation of EDTFP-1 COF material. (B) Powder XRD pattern of EDTFP-1 (black) and corresponding energy minimized simulated pattern (red). (C) Repeating unit cell and (D) hexagonal structure of EDTFP-1 COF viewed along the pore axis.

3.3.2. Porosity and surface area measurement.

The N_2 sorption isotherm of EDTFP-1 (Figure 2) displayed both type I and IV isotherms characteristics without any hysteresis loop. The large uptake was noted at relatively low pressure region (0 to 0.1 P/P_0), that elucidated, good microporosity in the polymer matrix. Along with a gradual increase in N_2 uptake in the intermediate P/P_0 revealed the existence of extensively vast area of mesopores (35). The surface area of the material was measured to be 223 m^2g^{-1} with a pore volume of 0.107 ccg^{-1}. Pore size distribution plot by employing NLDFT method revealed the peak pore was 1.5 nm widths. Pore size of COF crystal structure was gauged and validated with the help of Accelrys software.

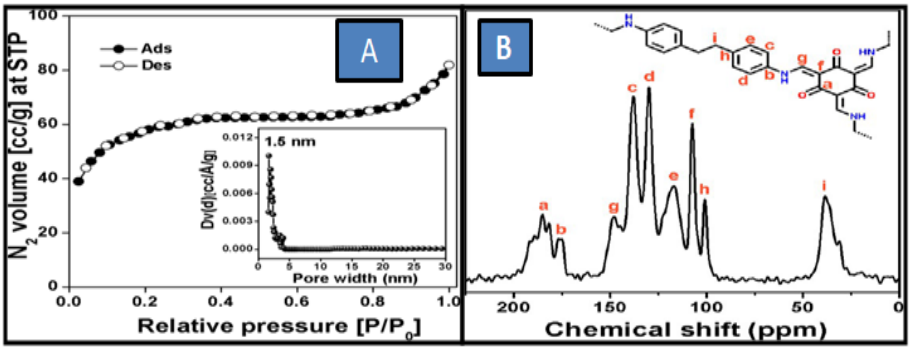

Fig.2 A) Nitrogen adsorption−desorption isotherm of EDTFP-1 material, where filled circle and empty circle represents the adsorption and desorption isotherm, respectively. The pore size distribution plot is shown in the inset.(B) Solid- state 13C CP MAS NMR spectrum of EDTFP-1 material. Different signals are assigned corresponding to the carbon atoms of the framework.

3.3.3. Spectroscopic analysis.

^{13}C CP MAS NMR spectrum of EDTFP-1 (Figure 3) displayed resonance signals at 185, 175, 148, 138, 130, 117, 107, 101 ppm for different carbon atoms present in the polymer framework. The peaks at 185 and 175 ppm raised from the carbonyl carbon atom and the benzene ring carbon adjacent to the –N-H group, respectively. 148 ppm signal was assigned to the enamine carbon atom.

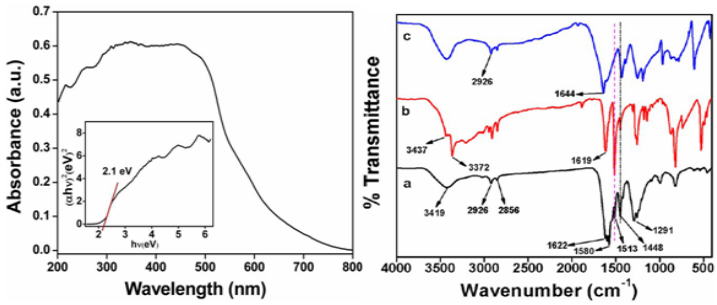

Fig. 3 A. UV-visible spectrum of EDTFP-1 material. B. FT IR spectra of (a) EDTFP-1, (b) 4,4′-ethylenedianiline, and (c) TFP

The peaks were appeared at 138, 130, 117, 107, 101 ppm corresponding to the different carbon atoms of the benzene rings. The peak at 107 ppm was observed due to sp^2 carbons of the phloroglucinol moiety. Sharp signal at 38 ppm was assigned due to the presence of ethylene carbon atoms. In the FTIR spectrum of EDTFP-1 (Figure 3), a broad peak appeared at 3419 cm^{-1} and a weak signal at 1513 cm^{-1} due to N–H stretching and N–H bending vibration in the polymer matrix. The two characteristic peaks centered at 2926 and 2856 cm^{-1}, were ascribed to the presence of sp^2 and sp^3 hybridized carbon. However, absence of hydroxyl (–OH) and imine (C=N) stretching bands suggesting that the framework was not present in enol form. The strong adsorption band arises at 1580 cm^{-1} due to the presence of C=C stretching band for enol to keto tautomerization (36). The characteristic peak in the range of 1244-1294 cm^{-1} was observed for newly formed C–N group. The peak centered at 1622 cm^{-1} could be attributed to the α,β-unsaturated ketone in the polymer matrix in the enol tautomer(36). Further, the two well defined peaks were noticed at 3437 and 3372 cm^{-1} for stretching vibration of primary amine (NH_2) group and another strong band at 1619 cm^{-1} due to in-plane bending vibration of NH_2 in 4,4'-ethylenedianiline part was observed (Figure 4c). On the other hand the UV-visible adsorption band of EDTFP-1 suggested $\pi \rightarrow \pi^*$ and $\sigma \rightarrow \sigma^*$ transitions and band gap of 2.1 eV **(**Figure 3**)**.

3.3.4. Microscopic and thermal stability analysis.

FE-SEM images of EDTFP-1 (Figures 5a and 5b) suggested nanofibre like morphology having diameter of *ca.* 22-30 nm and length of *ca.* 200 nm, and these are randomly distributed throughout the whole specimens to form bundle of wire like network. The high-resolution transmission electron microscopic images of EDTFP-1 (Figure 6) further revealed nanofibre type particle morphology with uniform micropores of *ca.*1.5 nm.TGA/DTA plot of EDTFP-1 in air flow indicated first weight loss due to the evaporation of adsorbed water from material surface, and the second and third weight loss in 310-500 ºC due to the cleavage

of C–C and C–N bond and the burning of remaining organic moieties of polymer framework (Figure 4). Thus, TGA analysis revealed its considerably high thermal stability up to 300 ºC. Further, CHN analysis data revealed C= 66.5, H= 4.76 and N= 7.25 %, which agrees very well with the model structure of EDTFP-1 shown in Figure 1A.

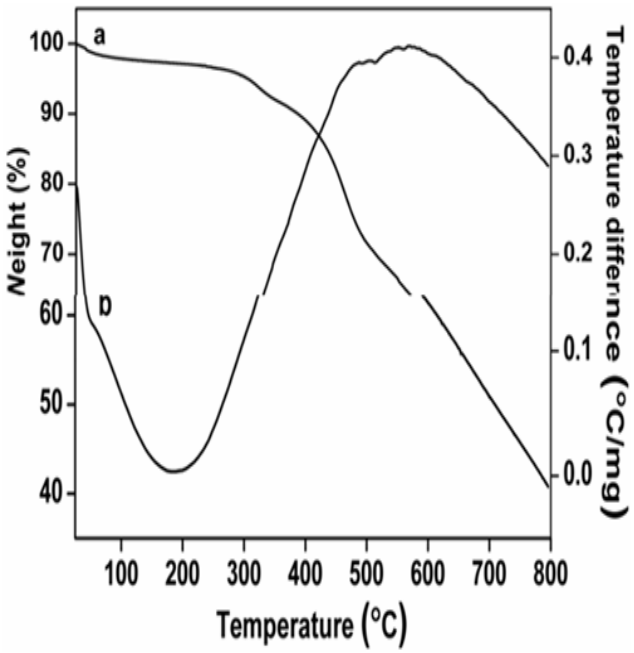

Fig.4 TGA (a) and (b) DTA (b) profile diagrams of EDTFP-1 material

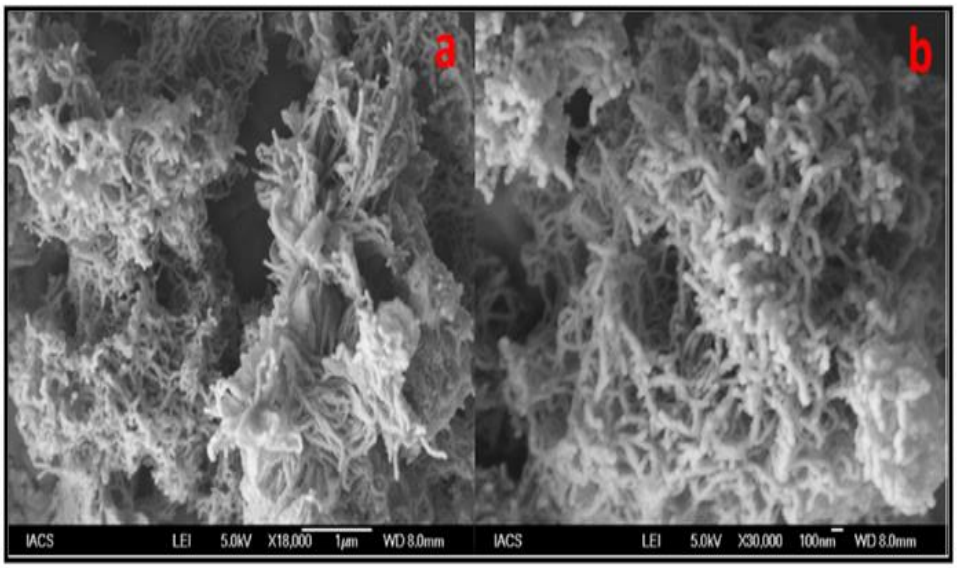

Fig.5 FE-SEM images of EDTFP-1 material at two different magnifications: (a) 18 000 and (b) 30 000×

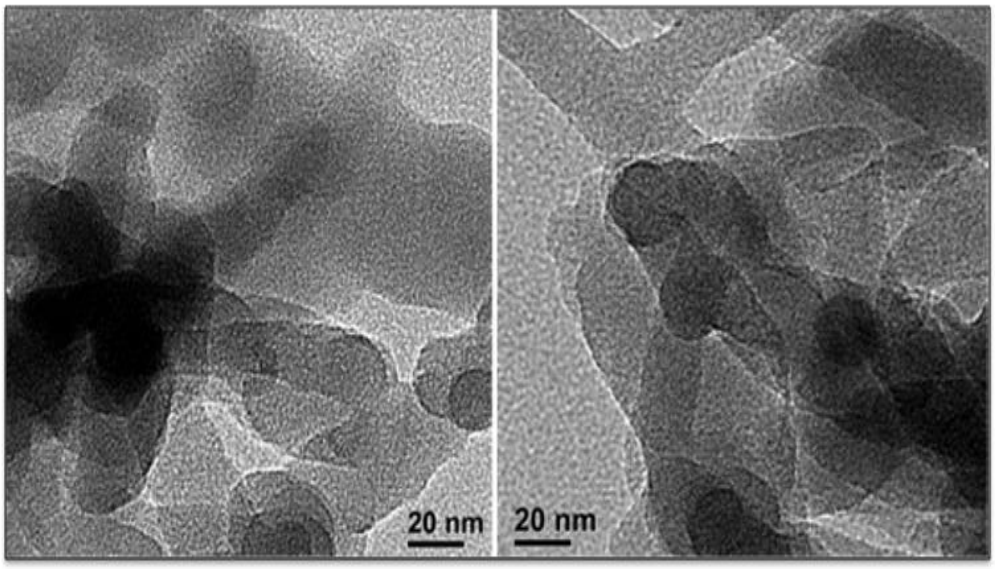

Figure 6. HR-TEM images of EDTFP-1 material

3.3.5. EDTFP-1 induced Apoptosis.

Zhang *et al*(37) and Gao *et al*(38)have predicted that NPs with a radius of approximately 25 nm have the shortest internalization time of about 20 minutes. The uptake rate reaches a maximum at the optimal radius of 25 nm as observed Zhang et al and thus this provides a valuable piece of information for the rational design of NPs like cellular delivery of COF. The EDTFP-1 nanofiber has particle size of 22-30 nm diameter. So EDTFP-1 easily internalized by endocytosis.The cytotoxic effect of EDTFP-1 was evaluated on A549, HepG2, HCT116 and MIA PaCa-2 cells by MTT assay to determine the cellular death response. Treatment with different concentrations of EDTFP-1 (0 to 100 µg/ml) for 24 h reduced the cell viability significantly in a dose-dependent manner with a lower IC_{50} value of 9.89 ± 1.16 µg/ml for HCT116 and 11.88 ± 1.82 µg/ml for A549 cells when compared with the standard chemotherapeutic drug, 5-fluorouracil (10.24 ± 2.14 µg/ml for HCT116 and 12.30 ± 3.18 µg/ml for A549 cells) (39). On the other hand, the IC_{50} value for EDTFP-1-treated HepG2 (14.38 ± 2.01 µg/ml) and MIA PaCa-2 (14.30 ± 1.32 µg/ml) cells was significantly higher when compared with the 5-fluorouracil-treated cells. Thus, the concentration of 10µg/ml was selected for the entire experimentation using HCT116 cells (Figure 8A). We had evaluated the cell viability of the monomer units TFP and DEA as controls for HCT116 cell line under controlled experiments. Our experimental results depicted building block monomer units of the COF do not have any activity for inducing apoptosis at 10 µg/mL concentration (Figure 7). These monomers have some kind of cytotoxicity above 40 µg/mL concentration. The dosing amount of the monomers present in the COF was significantly less than the cytotoxic level. So the monomers do not have any effect at 10 µg/mL concentration in apoptosis.

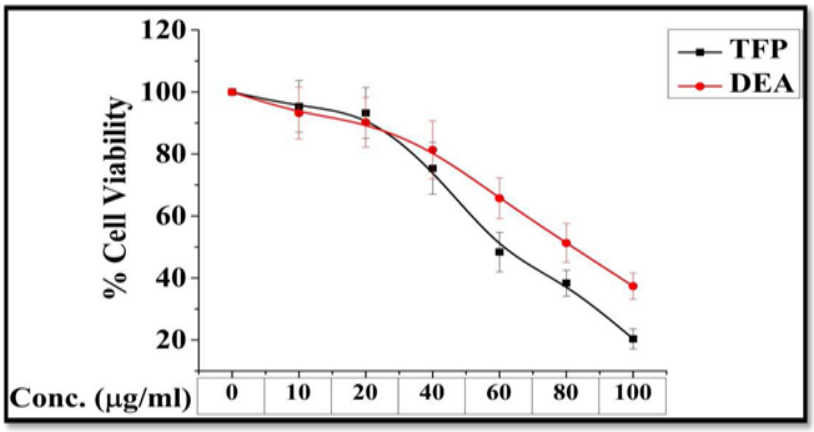

Fig.7 Cell viability of the monomer units TFP and DEA as controls for HCT116 cell line

In order to evaluate whether the cytotoxic effect of EDTFP-1 was directly correlated with apoptosis, morphological analysis of treated cells was determined using Immunofluorescence microscopy as apoptotic cells have some characteristic of changes like cell shrinkage, rounding, and nuclear condensation and DNA fragmentation (39). The morphological changes of treated cells (A549 and HCT116) were assessed using AO/EtBr and DAPI staining (nuclear staining dye). The number of densed bright fragmented nuclei was markedly increased in EDTFP-1-treated condition after DAPI staining and dual positive cells ($AO^+/EtBr^+$) were higher in EDTFP-1 treated cells when compared with the untreated control (Figure 8B) as evidenced by yellowish, orange-red or their combination coloured nuclei upon AO/EtBr staining. This data was further confirmed with the analysis of DNA fragmentation assay (Figure 8C).

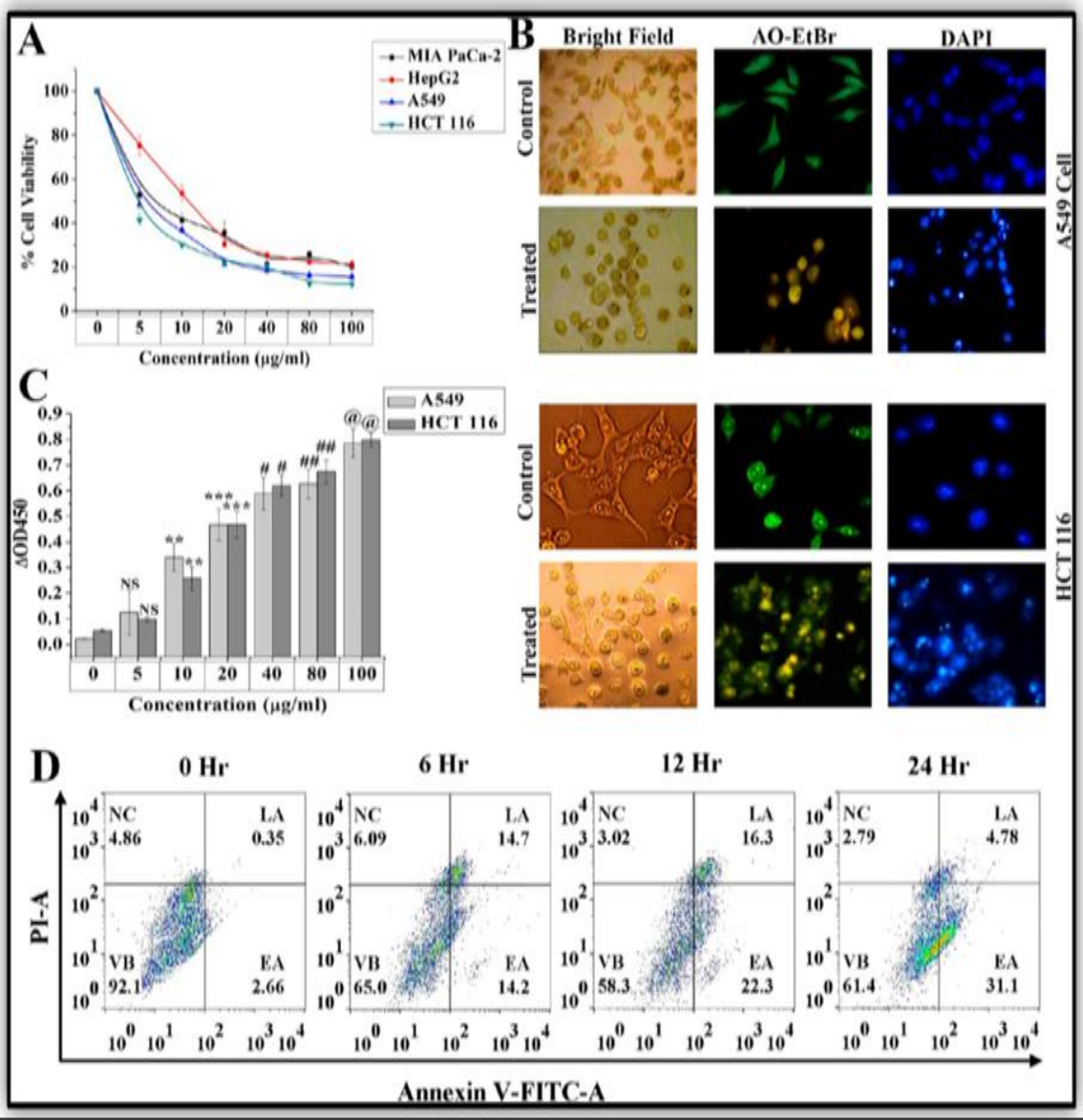

Figure 8. (A) Effect of increasing doses (0–100 µg/mL) of EDTFP-1 on different cancer cell lines in 24 h. (B) Morphological and nuclear changes of A549 cells (upper panel) and HCT116 cells (lower panel). Morphological change of normal and EDTFP-1 treated (for 24 h) cells (left column of both panels). AO/EtBr staining of normal and treated cells (middle column of both panels) for nuclear changes. DAPI staining of normal and treated cells (right column of both panels) for nuclear changes. (C) DNA fragmentation status of A549 and HCT116 cells with increasing doses of the DP. (D) Annexin V, FITC/PI positive cells with time of treatment of 10 µg/ml of EDTFP-1 by flow cytometry.

To explore whether the EDTFP-1 was involved in apoptosis/necrosis, flow cytometric assessment was conducted using Annexin-V-FITC/PI staining by studying the level of exposed phosphatidyl serine (PS) in outer membrane of cells. Result portrayed that the

percentage of apoptotic (early and late) cells was stretched in a time-dependant manner (14.2% EA/14.7% LA for 6 h, 22.3% EA/ 16.3% LA for 12 h and 31.1% EA/4.78% in LA for 24 h) with respect to the control cells (2.66% EA and 0.35% LA) (Figure 8D). These results suggested that EDTFP-1-induced cell death was directly correlated with cytotoxicity followed by apoptosis.

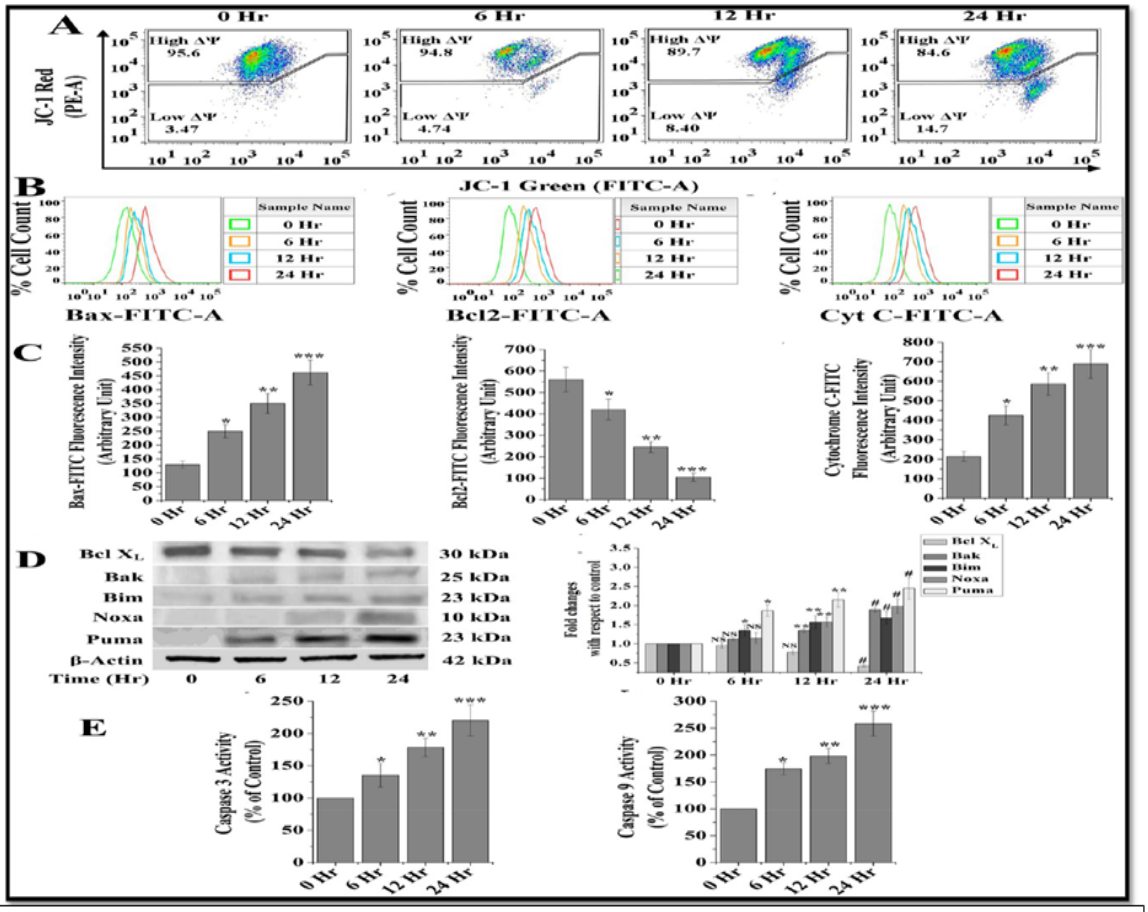

Figure 9. (A) Change in mitochondrial membrane potential with time following treatment by 10 µg/mL of EDTFP-1. (B) Level of Bax, Bcl-2, and cytochrome C positive cells. (C) FlowJo analysis of B. (D) Western blot analysis of different apoptosis regulatory proteins (left column). Right column is the FlowJo analysis of the same. (E) Left column is the level of active caspase-3 and right column is that for caspase-9 with time of EDTFP-1 (10 µg/mL) treated HCT116 cells.

Apoptosis can proceeds through the mitochondrial-dependant pathway (intrinsic) or extrinsic pathway (mitochondrial-independent pathway) or both (40, 41). Mitochondria are the power house of cell because of ATP synthesis. So mitochondrial dysfunction played a vital role in the induction of apoptosis and has even been suggested to be central to the apoptotic pathway. This has been fundamental fact that loss of mitochondrial membrane potential is an early indication of apoptosis. That is why we had studied the loss of mitochondrial membrane potential in Figure 9A as an important step of apoptosis signaling pathway. Here we had to

investigate whether the EDTFP-1-induced apoptosis in HCT116 cells was involved through mitochondrial-dependant pathway, plethora of indices like loss of mitochondrial membrane potential, changes in the axis of pro-/anti-apoptotic proteins were assessed. Result displayed a significant increase in loss of mitochondrial membrane potential (MMP) in a time-dependant manner (4.74% for 6 h, 8.40% for 12 h and 14.7% for 24 h) due to the enlargement of mitochondrial membrane pore as illustrated from increased level of JC1 green fluorescence intensity in EDTFP-1 treated cells (Figure 9A). Following death signalling, a significant ($p<0.05$) time-dependant enhancement of Bax and Cytochrome C expression was found in EDTFP-1-treated cells followed by a marked decrease in Bcl2 expression when compared with the control cells as observed from median fluorescence intensity analysis. On the other hand, the immunoblot analysis portrayed a significant ($p<0.05$) time-dependant increase in Bak, Bim, Noxa and Puma expression was found upon EDTFP-1 treatment when compared with the control cells, suggesting that EDTFP-1-induced loss of MMP was correlated with the alteration of pro-and anti-apoptotic protein expression (Figure 9B). FlowJo and Western blot analysis of different apoptosis regulatory proteins were displayed in Figures 9C and 9D. The apoptotic fate was also confirmed using caspase 3 and 9 activity assessment in HCT116 cells as the data indicated that EDTFP-1-treatment was significantly augmented Caspase 3 and 9 activity with respect to the control cells (Figure 9E). The above data suggested that EDTFP-1 treatment triggered the release of pro-apoptotic protein as well as suppress the anti-apoptotic proteins in the mitochondria which were interacted with the increase in Caspase activity (26).

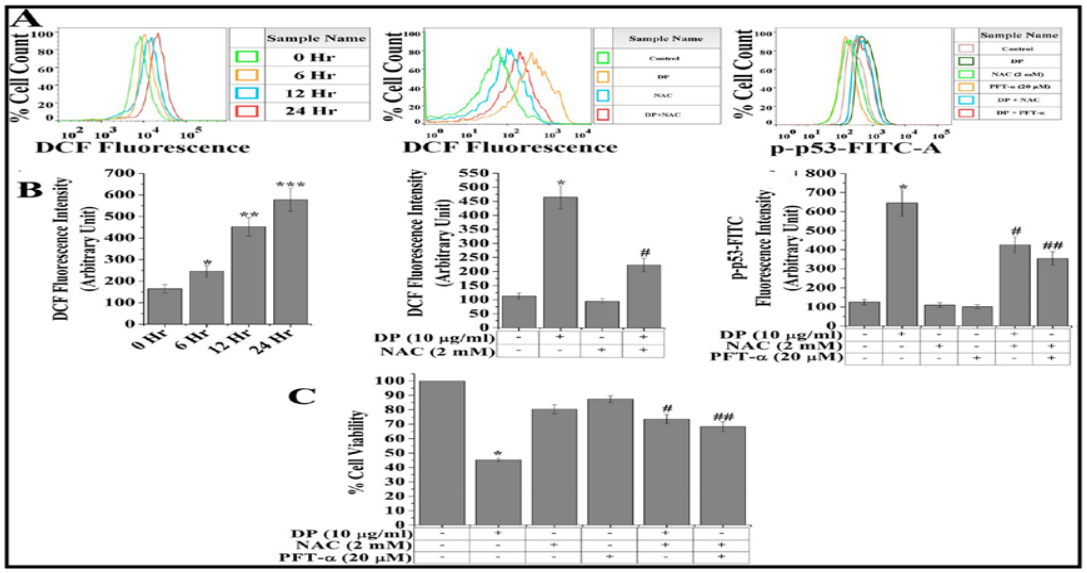

Figure 10. (A) Left column is the ROS level with time in 10 µg/ml of EDTFP-1 treated cells. Middle column is the level of ROS in the presence of ROS inhibitor, NAC (N-acetyl cysteine). Right column is the level of p53 in the presence of NAC, pifithrin (PFT-α). B: FlowJo analysis of the results of A. (C) Cell viability in the presence of NAC, PFT-α with or without the EDTFP-1 (10 µg/ml) for 24 h.

Apoptosis is triggered by elevated ROS either independently or dependently through the p53 phosphorylation (39). Current study deciphered, the level of ROS, p53 expression and their interplay were analysed using flow cytometry (Figure 10A and B).The mean fluorescence intensity of DCF was significantly ($p<0.05$) increased in a time-dependent manner upon EDTFP-1treatment. However, the increased level of ROS was markedly suppressed with the pretreatment of standard ROS scavenger, NAC (2 mM). On the other hand, EDTFP-1-treated reduction in cell viability (45.32 ± 1.21) was reversed using NAC (2 mM) treatment (80.35 ± 3.21) and this result suggested that the EDTFP-1-induced cytotoxicity was directly involved with the generation of ROS. Relation of ROS with the p53 phosphorylation upon EDTFP-1 treatment, through flow cytometric analysis confirmed time-dependant increase in p53 phosphorylation was significantly suppressed with the treatment of NAC (2 mM) and potent p53 inhibitor, PFT-α (20 μM) (Figure 10C) as reflected in cell viability analysis. Upon the pre-treatment with PFT-α and NAC on HCT116 cells, the EDTFP-1-induced suppression in cell viability was significantly ($p<0.05$) restored when compared with control cells. Thus, EDTFP-1 induces mitochondrial dependence apoptosis through the modulation of pro- and anti-apoptotic proteins (Figure 10).

To understand the stability of the COF material under aquatic conditions in the cells we had stimulated EDTFP-1 samples with pH = 5.0 (acidic pH), 7.0 (neutral) and 7.4 (PBS buffer) under 1-4 days stirring. Representative FE SEM images of the treated samples were sequentially displayed in Figure 11. SEM image analysis depicted that after acidic and neutral pH treatments there was no significant change in particle morphology. However, treatment in PBS buffer at 7.4 the nanofibers ware somewhat fragmented to form smaller nanofibers with similar agglomerated particle morphology. To check the stability of this EDTFP-1 COF in water, the samples treated at pH 7.0 for 24 h had been continuously stirred in this condition for another 3 days. This sample after treatment at pH 7.0 for 96 h showed similar nanofibers like morphology. There is no change in the diameter of the nanofibers after these treatments. This result confirmed that EDTFP-1 COF is stable in water and can be internalized into the cells for prolonged period of time.

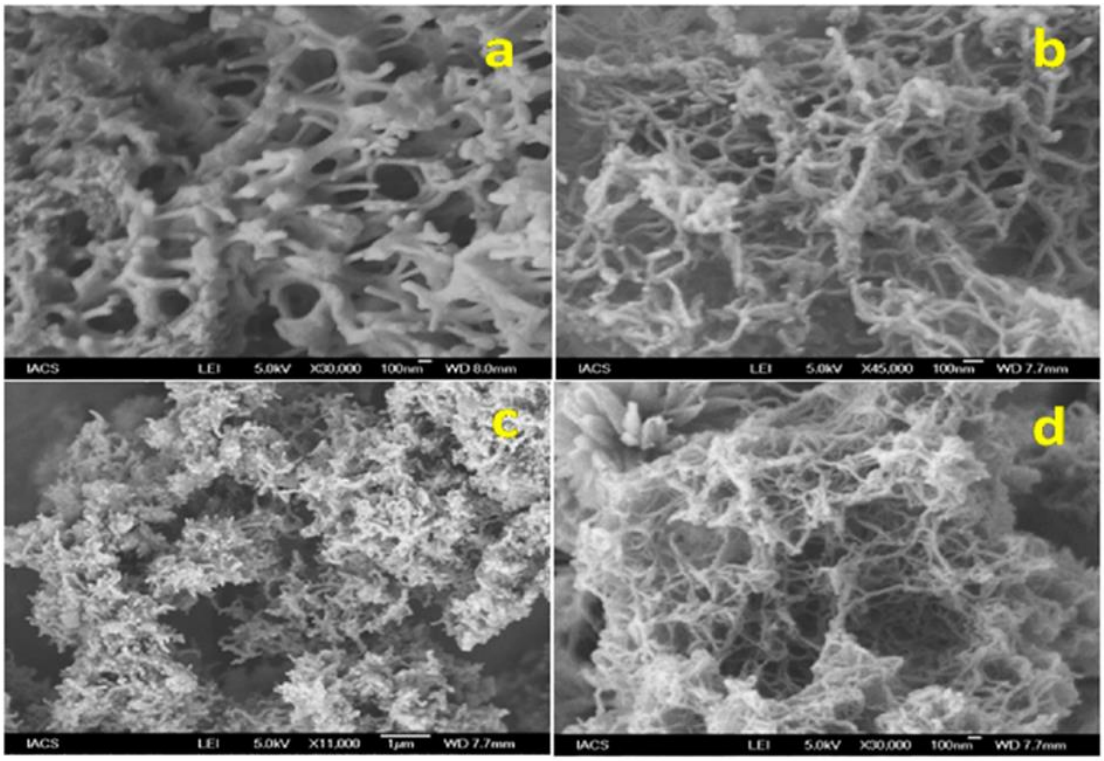

Figure 11. FE SEM images of EDTFP-1 after treatments at (a) pH 5.5 (acidic) for 24 h, (b) pH 7.0 (neutral) for 24 h, (c) pH 7.4 (PBS buffer) for 24h, and (d) pH 7.0 for 96 h.

The *in vitro* drug release experiments were carried out at pH 5.0 and 7.4 with 10 µg/ml of EDTFP-1 loaded into a dialysis bag. 0.01 mg of EDTFP-1 was suspended in a definite volume (1 ml) of phosphate buffer saline (PBS) of 7.4 and 5.0 solutions, transferred to dialysis bag and kept at 37ºC.The resulting suspension was immersed into 10 ml of PBS and pH 5.0 solutions and incubated at 130 rpm for a definite time period (4 h 30 min). 500 µl aliquots were taken out of the dissolution medium at appropriate time intervals (30 min) replaced by same volume of fresh PBS buffer and pH 5.0 buffer, to keep the volume of the release medium constant. The amount of EDTFP-1 released was observed by UV spectrophotometer at 420 nm.

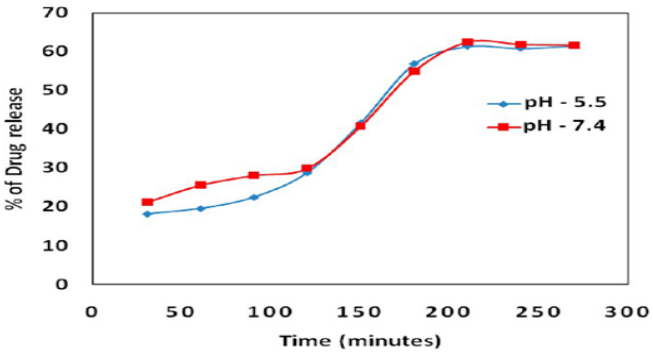

Figure 12. In vitro time-dependent pharmacokinetics of EDTFP-1 drug release at pH of 5.5 and 7.4.

In Figure 12 we have shown the drug release pharmacokinetics with time on EDTFP-1. The pharmacokinetics plot suggested almost no effect of pH in *in vitro* drug delivery. The drug release was simultaneously increasing up to 200 min (around 60% of EDTFP-1 COF) and after 200 min it became plateau.

3.4. CONCLUSIONS

We have amalgumed a novel microporous covalent organic framework material EDTFP-1 via Schiff base condensation reaction using 4,4'-ethylenedianiline and 2,4,6-triformylphloroglucinol. The porous COF material displayed very good BET surface area and 3D-hexagonal crystal structure with abundant Polyphenolic network in the polymeric backbone. Our *in vitro* experiments revealed EDTFP-1 induced cell death is associated with apoptotic phenomena like nuclear condensation, DNA fragmentation, externalization of Phosphatidylserine followed by loss of mitochondrial membrane potential, induce expression of pro-apoptotic proteins and suppress anti-apoptotic protein content. Therefore, EDPTA-1 may be coined as a potential anti-cancer agent, that overcomes vital prejudice in cancer therapeutics.

3.5. REFERENCES

1. R. D.Schreiber, L. J.Old, M. J. Smyth, *Science*,2011, 331, 1565−1570.

2. J.Ferlay, I.Soerjomataram, R.Dikshit, S.Eser,C.Mathers,M.Rebelo, D. M.Parkin, D.Forman, F.Bray, *Int. J. Cancer*,2015, 136, 359−386.

3. M. S.Lawrence, P.Stojanov, C. H.Mermel, J. T.Robinson,L. A.Garraway, T. R.Golub, M.Meyerson, S. B.Gabriel, E.S.Lander, G. Getz, *Natur* , 2014, 505, 495−498.

4. F. Q.Nie, M.Sun, J. S.Yang, M.Xie, T. P.Xu, R.Xia, Y.W.Liu, X. H.Liu, E. B.Zhang, K. H.Lu, Y. Q.Shu, *Mol. Cancer Ther.*,2015, 14, 268−277.

5. W. P. Roos, A. D. Thomas, B. Kaina, *Nat. Rev. Cancer*,2016, 16, 20−33.

6. R.Bayat Mokhtari, T. S.Homayouni, N.Baluch, E.Morgatskaya, S.Kumar, B.Das, & H.Yeger,*Oncotarget*, 2017,*8*(23), 38022–38043.

7. V.Schirrmacher, *International journal of oncology*, 2019, *54*(2), 407–419.

8. K.Nurgali, R. T.Jagoe, R.Abalo, *Frontiers in pharmacology*, 2018, 9, 245.

9. J.An, O. K.Farha, J. T.Hupp, E.Pohl,J. I.Yeh; N. L.Rosi, *Nat. Commun.* , 2012, 3, 604.

10. X.Zhang, D.Liu, D.Xu, S.Asahina, K. A.Cychosz, K. V.Agrawal, Y.Al Wahedi, A.Bhan, S.Al Hashimi,O.Terasaki, M.Thommes, M. Tsapatsis, *Science*,2012, 336, 1684−1687.

11. K.Sarkar,K.Dhara, M.Nandi, P.Roy, A.Bhaumik, P.Banerjee, *Adv. Funct. Mater* ,2009, 19, 223−234.

12. M. A.Ali, K.Mondal, Y. Y.Jiao, S.Oren,Z.Xu, A.Sharma,L.Dong, *ACS Appl. Mater.*, 2016, 8,20570−20582.

13.F. J.Uribe-Romo, C. J.Doonan,H.Furukawa, K.Oisaki, O. M.Yaghi, *J. Am. Chem. Soc.* 2011, 133, 11478−11481.

14. S. Y.Ding, W.Wang, *Chem. Soc. Rev.* 2013, 42, 548−568.

15. S.Dalapati, E.Jin, M.Addicoat,T.Heine, D. L.Jiang, *J. Am. Chem. Soc.* 2016, 138, 5797−5800.

16. A.Rengaraj, P.Puthiaraj, Y.Haldorai,N. S.Heo, S. K.Hwang, Y. K.Han, S.Kwon, W. S.Ahn, Y. S.Huh, *ACS Appl. Mater* , 2016, 8, 8947−8955.

17. Q.Fang, S.Gu, J.Zheng, Z.Zhuang; S.Qiu, Y.Yan, *Angew. Chem., Int. Ed.*,2014, 53, 2878−2882.

18. R.Gomes, P.Bhanja, A.Bhaumik, *Chem. Commu.*, 2015,51, 10050−10053.

19. Y. F.Zeng, R. Q.Zou, Y. L.Zhao, *Adv. Mater*, 2016, 28, 2855−2873.

20. H.Xu, S. S.Tao, D. L.Jiang, *Nat. Mater.* 2016, 15, 722−726.

21. H.Yang, S. L.Zhang,L. H.Han, Z.Han, Z.Xue, J.Gao,Y. J.Li, C. S.Huang, Y. P.Yi, H. B.Liu, Y. L.Li, *ACS Appl. Mater* , 2016, 8, 5366−5375.

22. N.Huang, X. S.Ding, J.Kim, H.Ihee, D. L. Jiang, *Angew. Chem.,Int. Ed.* 2015, 54, 8704−8707.

23. W.Cui, J. B.Li, G.Decher, *Adv. Mater*,2016, 28, 1302−1311.

24.A.Modak, A. K.,Barui, C.R. Patra, A.Bhaumik, *Chem.Commun*. 2013, 49, 7644−7646.

25. T. Y.Jiang, W. J.Sun, Q. W.Zhu, N. A.Burns, S. A.Khan,R.Mo, Z.Gu, *Adv. Mater.*2015, 27, 1021−1028.

26. K.Ishikawa, K.Takenaga, M.Akimoto, N.Koshikawa,A.Yamaguchi, H.Imanishi, K.Nakada, Y.Honma, J. I.Hayashi, *Science* , 2008, 320, 661−664.

27. M.Brentnall, L.Rodriguez-Menocal, R. L.De Guevara, E.Cepero, L. H.Boise, *BMC Cell Biol.*,2013, 14, 32.

28. W. P. Roos, A. D. Thomas, B Kaina, *Nat. Rev.Cancer* 2016, 16, 20−33.

29. R.Arya,M.Mallik, S. C.Lakhotia, *J. Biosci.*,2007, 32, 595−610.

30. Q. L.Hu, M.Gao, G. X.Feng, B.Liu, *Angew. Chem., Int. Ed.*, 2014, 53, 14225−

14229.

31. A. LAberasturi. M.Redrado, M.Villalba, L.Larzabal,M. J.Pajares, J.Garcia, S. R.Evans, D.Garcia-Ros, M. E.Bodegas,L.Lopez, L.Montuenga, A.Calvo, *Cancer Lett*., 2016, 370, 165−176.

32. A. V.Bazhin,P. P.Philippov, S.Karakhanova , *Oxid. Med. Cell.*, 2016, 4197815.

33. C. V.Yelamaggad, A. S.Achalkumar,D. S. S.Rao,S.K.Prasad,*J. Org. Chem.*, 2009, 74, 3168−3171.

34. Material Studio Release Notes, Release 4.2; Accelrys Software: San Diego, 2006

35. S. K.Das, M. K.Bhunia, A. K.Sinha, A.Bhaumik, *ACS Catal.*, 2011, 1, 493−501.

36. S.Chandra, T.Kundu, S.Kandambeth, R.Babarao,Y.Marathe, S. M.Kunjir, R.Banerjee, *J. Am. Chem.Soc.*, 2014, 136, 6570−6573.

37. S.Zhang, J.Li, G.Lykotrafitis, G.Bao, S.Suresh, *Adv. Mater.*, 2009, 21, 419−424.

38. H.Gao,W. D.Shi, L. B.Freund, *Proc. Natl. Acad. Sci. U. S. A.* 2005, 102, 9469−9474.

39. C.Focaccetti, A.Bruno, E.Magnani, D.Bartolini, E.Principi,K.Dallaglio, E. O.Bucci, G.Finzi, F.Sessa, D. M.Noonan, A.Albini, *PLoS One*,2015,10, e0115686.

40. A.Mallick, P.More, S.Ghosh, R.Chippalkatti, B.A.Chopade, M.Lahiri, S.Basu, *ACS Appl. Mater.*, 2015, 7, 7584−7598.

41. B.Liu, Y.Chen, D. K.St. Clair, *Free Radical Biol. Med.*, 2008, 44, 1529−1535.

Training, Seminar & Conference Presentations (Poster/ Oral/ Abstract):

1. Presented Poster entitled **"Novel Thiosemicarbazone metal complexes and it's Biological Efficacy"** in **National Seminar on Recent Advances in Biotechnology** conducted by CSIR-Indian Institute of Chemical Biology, Kolkata on April 17, 2015 (Poster/Abstract Presentation).
2. Completed Advance Course on "**Multicolor Flow Cytometry"** organized by CSIR-Indian Institute of Chemical Biology, Kolkata and Becton Dickinson (BD) India Pvt. Ltd., from 29th-30th June, 2015.
3. Presented Poster entitled **"Radiosensitization of Quercetin in Colorectal Carcinoma (HCT-116) cell line"** in **14th Annual Meeting of the Society for Free Radical Research-India (SFRR-India), International Conference on Translational Research in Ionizing Radiation, Free Radicals, Antioxidants and Neutraceuticals on Health, Disease and Radiation Biology** under the aegies of Department of Biochemistry, College of Medicine & JNM Hospital, WBUHS, Kalyani on January 7-9, 2016 (Poster/Abstract Presentation).
4. Attended 3rd International Meet on **Advanced Studies in Cell Signalling Network (CESIN 2016)** at CSIR- Indian Institute of Chemical Biology, Kolkata on December 18-20, 2016.
5. Participated in the **"Workshop on Basics of Flowcytometry"** organised by the Department of Zoology, West Bengal State University, Barasat and Becton Dickinson India Pvt. Ltd. From 3rd-10th February, 2017.
6. Presented Poster entitled **"Anticancer activity of Virgin Pomegranate Seed Oil on Human Colorectal Carcinoma (HCT-116) cell line"** in **2nd National Seminar-cum-Farmers' Fair, Pomegranate for Health, Growth & Prosperity** organised by ICAR-National Research Center on Pomegranate, Solapur 0n April 28-30th
7. Presented Poster entitled "**Covalent Organic Framework Material Bearing Phloroglucinol Building Units as a Potent Anticancer Agent"** at **AAPI Global Healthcare Summit,** 2017 in Kolkata, December 28th-31st, 2017.
8. Presented Poster entitled **"Folic acid-conjugated magnetic mesoporous silica nanoparticles loaded with quercetin enhances colorectal carcinoma cell death through JNK/p53 axis: A theranostic approach for cancer management"** in **16th Annual Meeting of the Society for Free Radical Research-India (SFRR-India)**, International Conference on Translational Research in Free Radicals, Micronutrient

Antioxidants and Functional Foods at All India Institute of Medical Sciences, New Delhi, India on 18th-20th February, 2018.

9. Presented **Poster** entitled **"Amelioration of diabetic nephropathy using pomegranate peel extract-stabilized gold nanoparticles: assessment of NF-κB and Nrf2 signaling system"** on **6th World Congress of Nanomedical Sciences Chemistry Biology Interface: Synergistic in New Frontiers (CBISNF-2019) & Science & Technology for the future of Mankind,** organised by Jamia Hamdard & University of Delhi at Vigyan Bhawan on 7th-9th January, 2019.

Publications:

1. **Coumarinyl thioether Schiff base as turn-on fluorescent Zn (II) sensor and the complex as chemosensor for the selective recognition of ATP along with its application in live cell imaging. Patra C, Bhanja A K, Mahapatra A, Mishra S, Das Saha K, Sinha C : RSC Adv., 2016,6, 76505-76513**

2. **A novel nanohybrid for cancer theranostics: folate sensitized Fe2O3 nanoparticles for colorectal cancer diagnosis and photodynamic therapy. R Nandi*, S Mishra*, T K Maji, K Manna, P Kar, S Banerjee, S Dutta, S. K. Sharma, P Lemmens, K D Saha and S K Pal. *J. Mater. Chem. B,* 2017, 5, 3927 (*joint first authors)**

3. **Specific Recognition of Cr^{3+} in Physiological Condition by allyl substituted appendage Rhodamine and Its Cell-Imaging Studies. Bhanja A K, Mishra S, Naskar K, Maity S, Saha K D, Sinha C. Dalton trans., 2017, DOI: 10.1039/C7DT03560H.**

4. **Synthesis of a novel glucose capped gold nanoparticle as a better Theranostic candidate. Saritha S, Sunil K C, Das U, Mishra S, Sudarshan M, Saha , K D, Dey S, Chakraborty A, Narayana V. PLOS ONE 0178202 June 5, 2017 1 / 15**

5. **Macrocycle aza-crown chromogenic reagent to $Al^{3+}$and fluorescence sensor for $Zn^{2+}$and Al^{3+}along with live cell application and logic operation. Bhanja A K, Patra C, Mondal S, Mishra S, Das Saha K, Sinha C. Sensors and Actuators B 252 (2017) 257–267**

6. **A fluorescence 'turn-on' chemodosimeter for specific detection of Pd^{2+} by rhodamine appended Schiff base and its application in live cell imaging. Bhanja AK, Mishra S, Das Saha K, Sinha C:Dalton Trans., 2017, DOI: 10.1039/C7DT01288H**

7. **Covalent Organic Framework Material Bearing Phloroglucinol Building Units as a Potent Anticancer Agent. Bhanja P*, Mishra S*, Manna K, Mallick A, Das Saha K, Bhaumik A: ACS Appl. Mater. Interfaces, 2017, 10.1021/acsami.7b07343, (*joint first authors)**

8. **A Schiff base platform: structures, sensing of Zn (II), PPi in aqueous medium and anticancer activity. Naskar B, Modak R, Maiti DK, Drew MGB, Bauzá A, Frontera A, Das Mukhopadhyay C, Mishra S, Das Saha K, Goswami S: Dalton Transaction, 2017, DOI: 10.1039/C7DT01932G**

9. **Porous Polymer Bearing Polyphenolic Organic Building Units as a Chemotherapeutic Agent for Cancer Treatment. Bhanja P, Mishra S, Manna K, Das Saha K, and Bhaumik A: ACS Omega, 2018, 3, 529−535**

10. **Isoelectronic Pt (II) - and Au (III)-N-Heterocyclic Carbene Complexes: A Structural and Biological Comparison. Rana B , Mishra S, Sarkar D, Mondal T K, Seth K S , Bertolasi V, Saha K D, Bielawski W C, Isab A A, and Dinda J: New Journal of Chemistry DOI: 10.1039/C8NJ01562G, 2018**

11. **Use of rhodamine-allyl Schiff base in chemodosimetric processes for total palladium estimation and application in live cell imaging. Bhanja A K, Mishra S, Kar K, Naskar K, Maity S, Saha K D, Sinha C: New Journal of Chemistry 42 (21), 2018, 17351-17358**

12. **A new triazine based π-conjugated mesoporous 2D covalent organic framework: its in vitro anticancer activities. Das K S, Mishra S, Manna K, Kayal U, Mahapatra S, Saha D K, Dalapati S, Das G P, Mostafa A A, Bhaumik A: Chemical communications (Cambridge, England) 54 (81), 2018, 11475-11478**

13. **Amelioration of diabetic nephropathy using pomegranate peel extract-stabilized gold nanoparticles: assessment of NF-κB and Nrf2 signaling system:Manna K*, Mishra S*, Saha M, Mahapatra S, Saha C, Yenge G, Gaikwad N, Pal R K, Oulkar D, Banerjee K, Saha K D: International journal of nanomedicine 14, 2019, 1753 (*joint first authors)**

14. **Efficient Detection of Early Events of Alpha Synuclein Aggregation using a Cysteine Specific Hybrid Scaffold: Chatterjee S, Ghosh S, Mishra S, Saha K D, Banerji B: Biochemistry, 2019**

15. **Bromelain with peroxidase from pineapple are more potent to target leukemia growth inhibition-A comparison with only bromelain: Debnath R, Chatterjee N, Das S, Mishra S, Bose D, Banerjee S, Das S, Saha K D, Ghosh D, Maiti D: Toxicology in Vitro 55, 2019, 24-32**

16. **Semisynthetic Quercetin Derivatives with Potent Antitumor Activity in Colon Carcinoma: Mukherjee A*, Mishra S*, Kotla K N, Manna K, Roy S, Kundu B, Bhattacharya D, Saha K D, Talukdar A: ACS Omega 4 (4), 2019, 7285-7298 (*joint first authors)**

17. **Intracellular anti-leishmanial effect of Spergulin-A, a triterpenoid saponin of Glinus oppositifolius: Das Saha K Banerjee S, Mukherjee N, Gajbhiye RL,**

Mishra S, Jaisankar P, Datta S: Infection and Drug Resistance, 2019, 2933—2942

18. **Ferulic acid enhances the radiation sensitivity of lung and liver carcinoma cells by collapsing redox homeostasis: mechanistic involvement of Akt/p38 MAPK signalling pathway: Das U, Manna K, Adhikary A, Mishra S, Das Saha K, Dey Sharma R, Majumder B, Dey S: Free Radical Research, 2019, 53, 944-967**

19. **Folic acid-conjugated magnetic mesoporous silica nanoparticles loaded with quercetin: a Theranostic approach for cancer management: Mishra S, Manna K, Kayal U, Saha M, Chatterjee S, Chandra D, Hara M, Datta S, Bhaumik A, Das Saha K: RSC Advances, 2020, 10, 23148-23164**

20. **Triptycene-Based and Schiff-Base-Linked Porous Networks: Efficient Gas Uptake, High CO2/N2 Selectivity, and Excellent Antiproliferative Activity: Alam A, Mishra S, Hassan A, Bera R, Dutta S, Das Saha K, Das N: ACS Omega, 2020, 5, 4250-4260**

21. **Pro-oxidant therapeutic activities of cerium oxide nanoparticles in colorectal carcinoma cells: Datta A*, Mishra S*, Manna K, Das Saha K, Mukherjee S, Roy S: ACS Omega, 2020, 5, 9714-9723 (*joint first authors)**

22. **A Novel Cyclic Mobile Transporter Can Induce Apoptosis by Facilitating Chloride Anion Transport into Cells: Kulsi G, Sannigrahi A, Mishra S, Das Saha K, Datta S, Chattopadhyay P, Chattopadhyay K: ACS Omega, 2020, 5, 16395-16405**

23. **Evalution of catacholase mimicking activity and apoptosis in human colorectal carcinoma cell line by activating mitochondrial pathway of copper(II) complex coupled with 2-(quinolin-8-yloxy)(methyl)benzonitrile and 8-hydroxyquinoline: Ali A*, Mishra S*, Kamaal S, Alarifi A, Afzal M, Das Saha K, Ahmad M: Bioorganic Chemistry, 2020, 104479 (*joint first authors)**

24. **Analysis of various diagnostic, Therapeutics as well as immunization strategies based on nanotechnology against Covid-19 pandemic: an Interdisciplinary View: Sujan Chatterjee#, Snehasis Mishra#, Kaustav Dutta Chowdhury, Chandan Kumar Ghosh * and Krishna Das Saha* (Just accepted in Lifesciences) (*joint first authors)**